MEDICAL IMAGE ANALYSIS AND VISUALIZATION USING GEOMETRIC DEFORMABLE MODEL

Shuo Li

A thesis
in
The Department
of
Computer Science and Software Engineering

Presented in Partial Fulfillment of the Requirements
For the Degree of Doctor of Philosophy
Concordia University
Montréal, Québec, Canada

March 2006

Your file Votre référence
ISBN: 978-0-494-34792-8
Our file Notre référence
ISBN: 978-0-494-34792-8

Abstract

Medical Image Analysis and Visualization using Geometric Deformable Model

Shuo Li, Ph.D Candidate.
Concordia University, 2006

Medical image analysis and visualization has become increasingly important in computer aided medicine. Throughout the history of medicine, advances in imaging have led to great progress in medical interventions.

The thesis proposes, develops and evaluates methods for automated analysis, visualization and quantification of medical images. The focus of this thesis is to perform both theoretical and practical investigations into medical image analysis and visualization to overcome current challenges in the field.

The theoretical framework for fulfilling above goals is based on segmentation using the geometric deformable model and some new advances: support vector machine and principal component analysis from the pattern recognition and machine learning. The medical applications of the above theoretical framework include automated computer aided analysis of dental X-ray image and chest computer tomography volumetric image reconstruction and visualization.

There are three main contributions in the thesis:

1. We propose and develop two faster and more robust segmentation methods which have the potential to be used in clinical and hospital environments.
2. We propose and develop the first dental X-ray image analysis and visualization system. It is able to analyze the dental X-ray image, extract the features and then recognize the patterns of certain diseases such as root decay and areas of bone loss. It has potential to be applied in the dental X-ray machine which has attracted interest from industry.
3. We propose and develop an efficient reconstruction and visualization framework. This method can reconstruct and visualize very large medical datasets with less time and less data volume.

Acknowledgments

Completing a PhD is truly a marathon event, and I would not have been able to complete this journey without the aid and support of countless people over the past years.

I would like to express my gratitude to my supervisors, Drs. Adam Krzyżak and Thomas Fevens, both of whom were driving factors to the successful completion of this thesis. Their expertise, understanding, and patience, added greatly to my experience.

I would like to thank my family for the support they provided me through my entire life and in particular, I must acknowledge my wife and best friend, Bo Chen without whose love and encouragement, I would not have finished this thesis.

I would like to thank the other members of my committee, Drs. William Lynch, Peter Grogono and Sudhir P. Mudur for the assistance they provided during my Ph.D study.

I would like to thank Dr. Aaron Fenster for presenting my defense as external reviewer and his constructive remarks.

Last, but for sure not least, I must also acknowledge Dongwook Cho and Chao Jin, whose friendship colors my life in the past few years.

Notations

$E_{()}$	Energy function
$P(x, y)$	Scalar potential function
$\mu(s)$	Mass density
$\gamma(s)$	Damping density
R^2	Two dimensional space
R^3	Three dimensional space
Ω	A bounded open subset of R^2 or R^3
ϕ	Lipschitz function
C	2D curve or 3D surface
t	Time
F	Speed function of level set
div	Divergence operator
ϕ_0	An initial level set function
k	Curvature
$c(x)$	Stopping term
σ	Standard deviation
∇	Gradient
∂	Partial derivative
u	Intensity value of a voxel or pixel
$p_i(u)$	Probability density function to be estimated inside
$p_e(u)$	Probability density function to be estimated outside
$\sum$	Summation function
$Area(x)$	Area function
$Length(x)$	Length function

δ_ε	Dirac delta function
da	Surface area element
$H(x)$	Heaviside function
$\vec{n}$	Exterior normal to the boundary
$\frac{\partial \phi}{\partial \vec{n}}$	normal derivative of ϕ at the boundary
H	Hessian of image
c_i	Mean grey value of the region
u_0	Original image
sgn	Sign function
Δt	Step size

Contents

List of Figures

Chapter 1

Introduction

"Don't be so humble - you are not that great."

– Golda Meir (1898-1978) to a visiting diplomat

Throughout the history of medicine, advances in imaging have led to expedite progress in medical interventions. Rapid changes in imaging procedures, such as digital radiography, virtual endoscopy, spiral Computed Tomography and Magnetic Resonance Image, have resulted in an active partnership between clinicians and information technologies. Accordingly, computer techniques play an increasingly important role in the medical imaging with computer aided medical image analysis and visualization has become one of the most important active research fields.

1.1 Background

Medical imaging provides an efficient visualization of the body's interior without painful and potentially risky surgery. It is a group of non-invasive techniques, pioneered by Wilhelm Röntgen, for the visual probing of the human body. X-rays are electromagnetic waves of short wavelength, capable of penetrating a certain thickness of matter. Medical X-rays are produced by a stream of those fast electrons not absorbed by the matter slowing down by a metal plate.

The left image in the Fig. 1 shows the first radiograph of a hand made by Wilhelm Röntgen on Dec. 22, 1895 [57]. Since then there has been a great advance in medical imaging as shown in the Fig. 1. The right image in Fig. 1, taken in 1995 is "100 years better" than the left image. The development of the medical

imaging has provided increasingly clear images. On the other hand, in the last decade, many new modalities such as virtual endoscopy, spiral Computed Tomography, interventional Magnetic Resonance and functional Magnetic Resonance have also successfully demonstrated their diagnostic values. At the same time, the high volume of the information provided by those new modalities requires assistance from the information technology field to reduce the workload of the doctors and radiologists.

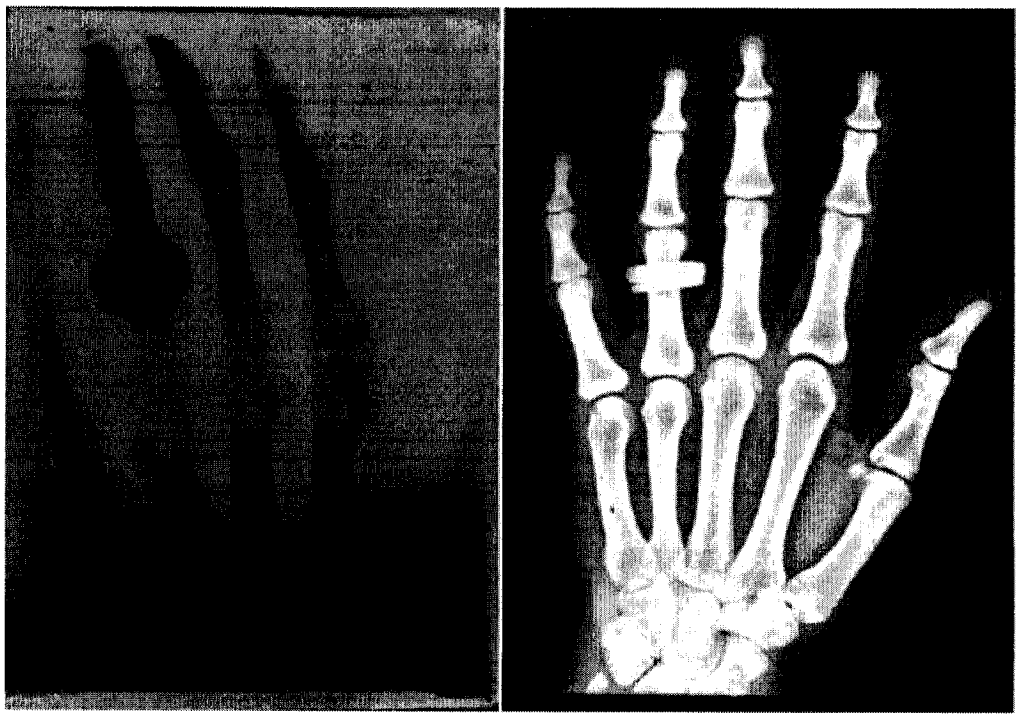

Figure 1: Changes over 100 years [57]. Left : first radiograph taken in year 1895 by W. C. Röntgen. Right: X-ray taken in 1995.

Based on the development of medical imaging, the analysis and visualization of medical images has been woven into the fabric of the pattern analysis and machine intelligence community and the computer graphics community since the very beginning. Initially, medical image analysis and visualization were seen as applying existing algorithms in the computer techniques to the medical dataset. However, over the last two to three decades, the unique nature of the problems presented within this area of study, such as the types of image information (image modality) that are acquired, fully three-dimensional and four-dimensional (3D+time) image

set, the nonrigid nature of object motion and deformation, and the statistical variation of both the underlying normal and abnormal ground truth, have led to the development of a new discipline in its own right.

1.2 Motivation and Objectives

As described above, with rapid advances in medical imaging modalities and computer techniques, medical image analysis and visualization has become very important in medical area. After decades of development, although modern image processing and visualization have provided very accurate and high quality 2D, 3D and 4D views of the anatomical structure, their utilization for accurate and efficient analysis and visualization is still limited.

The focus of this thesis is to perform both theoretical and practical investigations into medical image analysis and visualization. To meet the current challenges, we research and develop the new advances primarily in Image Processing, Pattern Recognition, Graphics and Computational Geometry to explore the possibility to combine the strength of novel methods as described in the Fig. 2.

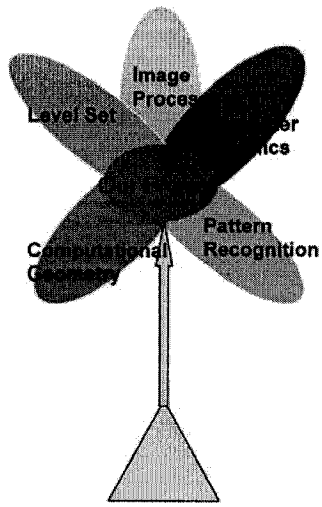

Figure 2: Methodologies involved in the thesis.

Based on the review and research of those new techniques, the road map for this thesis is proposed in Fig. 3. As shown in the road map, the level set based geometric deformable model (GDM) plays a important role in this thesis. The GDM will be first researched, developed and improved to achieve a fast, accurate and robust

segmentation. Then the segmentation will be used for visualization and computer aided diagnosis.

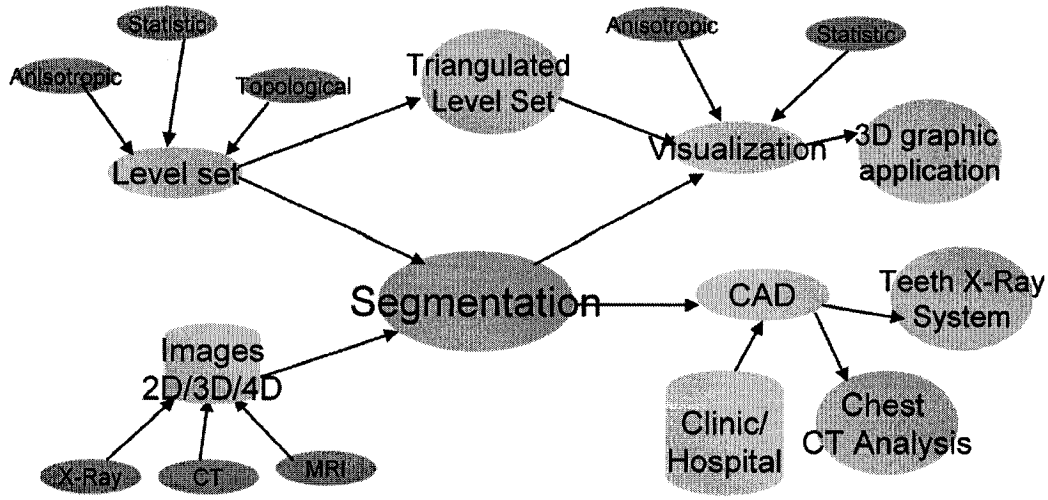

Figure 3: Road map of the thesis.

In essence, the aim of this thesis is to make the quality and speed of medical image analysis and visualization more suitable for clinical settings.

1.2.1 Objective One

The first objective of this thesis is to research and develop general automatic segmentation using GDM, for the clinical environment. The speed and efficiency of the algorithm is one of the main focuses.

Image segmentation has always been a critical component in medical imagery since it assists in medical diagnoses and visualization. But in medical imagery, image segmentation is more challenging compared to other imaging fields. This is primarily due to the large variability in topologies, complexity of medical structures, several kinds of spurious artifacts and restrictive scanning methods. This is especially true for volumetric medical images where a large amount of data is coupled with complicated 2D/3D medical structures. It is even worse for 4D medical image data. Among all types of image segmentation, clinical image segmentation is extremely challenging due to its demand on speed and accuracy.

One of latest techniques in segmentation is based on the class of GDM, referred as "level set" or "geodesic active contours/surfaces". It combines level set with a deformable model. The application of the model in medical image segmentation

has become very popular because of its ability to capture the topology of shapes in medical imagery. In this thesis, "geometric deformable model", "level set" and "geometric level set" will be used interchangeably.

Although popular, the level set algorithms are not generally suitable for clinical medical image processing due to following reasons:

1. Level set is an iteration based numerical algorithm with high computational cost.
2. Level set requires complicated settings for parameters. These settings depend on the type and content of the image and these may vary from image to image.
3. As a numerical solution of partial differential equation (PDE), level set is sensitive to the placement of initial contours:
   (a) The running time of level set method heavily relies on the position and size of initial curves and complexity of objects;
   (b) In some images, coupled level sets do not converge for some initial curves.

1.2.2 Objective Two

To test the applicability of the GDM to medical image analysis, an application in the computer aided diagnosis domain will be explored. Due to the fact that digital dental X-ray systems are replacing the traditional dental X-ray (film based) systems, which indicates an opportunity to apply computer aided dental X-ray analysis and diagnosis, one of our main objectives is researching and developing a computer aided dental X-ray analysis system using the GDM. A efficient computer aided dental X-ray system is able to provide great assistance to radiologists and dentists.

However it is a nontrivial work to develop such a system due to the following reasons:

1. Among all the image modalities, X-ray is a particularly noisy image modality.
2. There are great contrast and intensity changes on the dental X-rays. Even for the same person using the same machine, images taken within a short interval could have very large contrast and intensity changes.
3. In addition, teeth have very complicated topology which is sometime coupled with artificial filling.
4. Moreover, the orientation of the teeth is arbitrary in the real clinical setting, which challenges the automatic analysis system.

1.2.3 Objective Three

Volumetric medical image reconstruction is able to reconstruct the structured data from unstructured 3D dataset. It has very wide application in image modeling, 4D image tracking and computer aided diagnosis and surgery. To demonstrate the ability of the GDM on enhancing medical image reconstruction and visualization, a volumetric medical image reconstruction and visualization system using GDM will also be explored.

It is a very challenging problem since it is usually handles a large amount of information and more importantly it has the following challenges:

1. Unlike those data obtained from laser scanner and so on, as typical in computer graphics, which usually only contain a couple of objects, medical volume is usually consisted of multiple organs. Moreover these organs are usually coupled with complicated structure and topology which pose great challenges to the speed and efficiency of reconstruction.
2. Medical data usually have high noise, compared to the dataset obtained from optical scanners and so on. After reconstruction, the data volume is even greater.
3. Medical data usually have very close distribution of intensity value and the boundary between each object is not very clear. This is mainly due to the technique limit of the scanning techniques and the complicity of human organs. This poses great challenges to the simplification.

1.3 Thesis Structure

The layout of the remainder of the thesis is as follows:

1. **Chapter 2** presents an introduction to level sets and related background on medical imagery, medical image segmentation using level set and support vector machine.
2. **Chapter 3** presents our methodology for clinical level set segmentation. The results have been published in [36, 37]. It addresses the "Segmentation" bubble in the Fig. 3.
3. **Chapter 4** presents a fast segmentation framework using a pattern classifier trained by level set segmentation. The results have been published in [39, 41].

The work addresses the "Segmentation" bubble in the Fig. 3 with a slight different aspect from the above work described in Chapter 4. It focuses on the fast segmentation using a pattern classifier trained by a proposed pathological level set segmentation.

4. **Chapter 5** presents our innovative exploration towards automatic dental X-ray computer aided diagnosis. Some preliminary results have been published in [38, 40, 39, 41, 42, 43]. It is the first such a work to the best of our knowledge. The method is able to detect the early indication of bone loss and root decay, which may be treated thus avoiding more serious and expensive procedures in the future. It addresses the "CAD" and "Teeth X-ray System" bubbles in the Fig. 3.
5. **Chapter 6** presents our methodology on clinical volume reconstruction and visualization method. This work is done in collaboration with other fellow Ph.d student, Chao Jin, with the author of the thesis leading the research. Some preliminary results have been published in [31, 44]. The visualization part is implemented by Chao Jin. The work addresses the "level set" and "visualization" bubbles in the Fig. 3.

Chapter 2

Background Review

"It is my inner conviction that the development of science seeks in the main to satisfy the longing for pure knowledge... Discovery is really not a creative act"

- Albert Einstein (1879-1955)

2.1 Introduction

In this chapter, related background information would be reviewed. We would first give a historical perspective on the development of the medical imagery. And then a historical perspective of the development of the segmentation especially the GDM based segmentation would be given. Due to the fact that SVM plays an important role in the thesis, a brief introduction of SVM is also given in this chapter. All these background review provides a complete context for the thesis.

2.2 Medical Imaging

Here we provide a brief historical perspective of the development of medical imagery.

2.2.1 X-ray

X-ray was discovered in 1895 by the German Physicist Wilhelm Röntgen. The discovery of X-rays announced a new era in the practice of medicine.

However conventional X-ray imaging techniques have several limitations, especially the following two:

1. Small characteristic differences (1% to 2%) in X-ray attenuation by various body tissues are not detectable in recordings on X-ray film or fluoroscopic screens.
2. Much detail is lost in the radiographic process due to superposition of three-dimensional structural information onto a two-dimensional detector.

2.2.2 X-ray Computer Tomography (CT)

To overcome the problems in the traditional X-ray systems, CT imaging (also called as CAT scanning for Computed Axial Tomography) was invented in 1972 by Godfrey Hounsfield in England [57, 83]. The word "tomography" comes from the Greek words "tomeo", which means "cut" and "graphia" means "describing". CT scanning is based upon X-ray attenuation measurement at object's slices. The volume data is reconstructed and filtered from these slices. The reconstruction is made possible by the digital computer. The basic algorithm involved in the CT image reconstruction is based on theories proposed by the scientist Radon [56] in the late 1917's.

Originally, Hounsfield used gamma rays (and later X-rays) and a detector mounted on a special rotating frame together with a computer to create detailed cross sectional images of objects. The first system took hours to acquire a single slice. And the reconstruction took more than 24 hours. Current CT systems can acquire a single image in less than one second and the reconstruction can be done instantly.

CT has a revolutionary impact on diagnostic imaging since it eliminates or greatly minimizes the problem of superposition and differential attenuation mentioned above. CT provides unambiguous images of the cross-sectional dimensions of the body. More importantly it provides an excellent discrimination of soft tissues.

2.2.3 Magnetic Resonance Imaging (MRI)

Magnetic Resonance Imaging is based on the magnetic properties of atoms. An atomic nucleus rotates around its rotary axis (spin), and this produces a small magnetic field for nucleus with odd proton number. The Magnetic Resonance (MR) principle was discovered by Bloch and Purcell independently in 1946. Both were awarded the Nobel Prize in physics in 1952 [1, 2].

MRI was initially researched in the early 1970s and the first MRI prototype was

tested on clinical patients in 1980. It was approved for commercial, clinical availability by the Food and Drug Administration (FDA) in 1984 and its use throughout the U.S. has spread rapidly since then [1].

Although compared to the CT images, MRI usually is more noisy, MRI has revolutionized the standard of medical image diagnosis systems, largely because it provides highly detailed three-dimensional images of the human anatomy. Recently MRI has been used to acquire 4D data. With the advances in the computer and magnetic technology, the image quality of MRI has improved in the past decade, and a variety of different techniques are used in MRI applications today. The following are some of the commonly used techniques of MRI in modern medical diagnostics: functional MRI, interventional MRI, MR Angiography, MR Microscopy, MR Spectroscopy.

functional MRI (fMRI)

Functional MRI utilizes echo-planar imaging and involves very rapid scans of approximately 20 ms or less. It has been widely used in the brain research. It is able to detect the increase in the blood flow to the local vasculature that accompanies neural activity in the brain. Therefore activity in the patients brain, which is induced by some form of stimulation, either directly through the senses or by invoking some form of thought, such as memory can be easily captured. Sometimes chemical agents are injected into the blood before stimulation to increase the contrast in the MR images.

The main advantages to use fMRI as a technique to image brain activity include:

1. The scan does not require injections of radioactive isotopes. Therefore it more safer.
2. The scan is very fast. Therefore the blood flow increase, which indicates the brain activities, can be captured. Therefore it has been used widely in the research.

interventional MRI (iMRI)

iMRI defines the intraoperative application of MRI, which enables real-time scanning. Virtual real-time feedback provided by the iMRI allows the doctor to precisely localize brain and spinal lesions at the time of surgery thus facilitating more

accurate surgical procedure. This characteristic enables iMRI to be used in the following areas: planning and visualization, guidance and navigation, and monitoring the therapy.

MR Angiography (MRA)

MRI of the blood vessels is called MR Angiography. It utilizes MR technology to detect, diagnose and aid the treatment of heart disorders, stroke and blood vessel diseases. MRA produces images of blood flow within the circulatory system. With MRA, detailed images of blood vessels and blood flow are obtained without having to insert a catheter directly into the vessel, so that there is no risk of damaging an artery.

MR Microscopy (MRM)

MRM is a form of high-resolution imaging. It works under the same principle as traditional MRI, only modified for smaller specimens.

MR Spectroscopy (MRS)

MRS utilizes the same magnet and electronics as other MRI, but with specialized methods that produce a "spectrum" identifying different chemical compounds in the tissues. It allows the assessment of chemical shifts within the tissue, which has been shown to be useful for diagnosis of cancer, Alzheimer's disease, diabetes, and certain inflammatory and ischemic diseases.

2.2.4 Positron Emission Tomography (PET)

PET is a molecular imaging technique that uses radioactive labeled molecules to image molecular biological processes in vivo. The first PET camera was built in 1973 by Edward Hoffman, Michael M. Ter-Pogossian, and Michael E. Phelps. Four years later (1977), the full-body PET scanner was constructed. Phelps [83], who is often credited as inventor of PET, received the 1998 Enrico Fermi Presidential Award for his work.

TPET is very useful tool for the study of live objects, because PET images describe not a structure, but chemical function (metabolism) of objects. Therefore, a PET scan is often used to detect and evaluate cancer, such as of the lung or

breast cancer. It also can be used to evaluate the heart's metabolism, blood flow and examine brain function.

2.2.5 Single Photon Emission Computed Tomography

Single photon emission computed tomography (SPECT) is a nuclear imaging modality, which was invented in 1963 by Kuhl and Edwards. It was once discredited because the quality of image is not acceptable. The problem is solved by applying X-ray CT image reconstruction algorithms were applied to ECT to take into account for attenuation for scatter in the body. Moreover recent advances include refinements that make SPECT significantly more user friendly for both clinicians and patients. This results in a notable growth in its presence as a member of the imaging community.

SPECT produces 3D images that relate to an organ's function. This allows for better visualization of the extent of disease and reveals the progress of the disease at the early stage. Therefore, it is an efficient tool for brain function research. Compared to MRI or PET, it is much less expensive.

Beside the above modalities, there are still other imaging modalities, ultrasound and fluoroscopy for example. They are omitted since they are not directly related to our research.

2.3 Segmentation

As one of the important techniques in image processing, image segmentation has been intensively studied. Due to the nature of segmentation, most of the algorithms are specified for particular problems. In this section, we will give a brief introduction to image segmentation methods.

As shown in the Fig. 4, those existing image segmentation algorithms can be broadly classified into three categories: structural techniques, statistical techniques and other techniques. Structural techniques are those techniques which take into consideration structural information during segmentation; stochastic techniques are those which perform the segmentation based on statistical analysis methods; and other techniques are those which do not primarily use structure or stochastic techniques for segmentation.

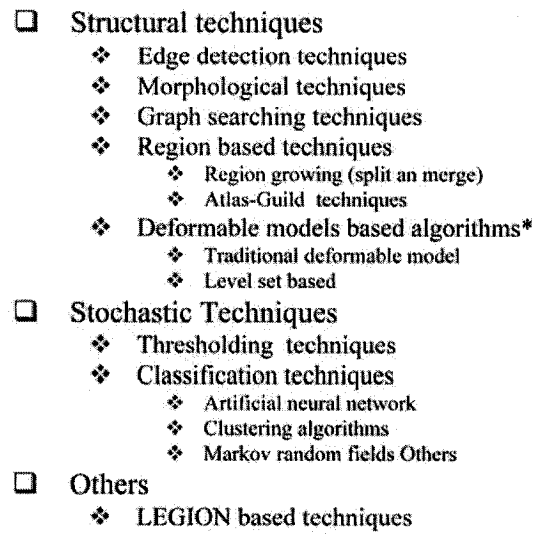

Figure 4: Classification of segmentation methods.

2.4 Classic Deformable Models and Medical Segmentation

The classic deformation model plays an important role in image segmentation. In the past decade a large amount work was devoted to application of deformable models for segmentation. In a classic deformable model, users typically initialize a deformable model near the region of interest (ROI) and allow it to evolve into an exact position. The user can then manually fine-tune the fitting by using interactive capabilities. These models gained great successes in the human interaction based applications.

The first use of classic deformable models in the medical image analysis was the application of deformable contour models, such as snakes [32], to segment 2D images. To segment 3D medical datasets, each 2D slice is segmented separately. Once a 2D slice is segmented, the contour of that slice is used as a reference contour for neighboring slices. This reference contour is then deformed into place in those slices. This process is repeated for all the 2D slices. The resulting sequence of 2D contours is then connected to form a continuous 3D surface model [12, 15, 45]. Obviously the process is not only laborious and requires a post processing step to connect the sequences of 2D contours into a surface, but also the reconstructed surface can have various inconsistencies since the consistency existing in 3D is not taken into

consideration. However it is not a true 3D segmentation. In one of the initial works on true 3D segmentation, Miller [51] in 1991 proposed a "balloon" approach by approximating a sphere using polygons. He then geometrically deformed this balloon until its surface conformed to the object surface in 3D CT data. The whole segmentation process is formulated as the minimization of a weighted cost function.

Deformable superquadrics, proposed by Terzopoulos *et al.* [72], and deformable generalized cylinders, proposed by O'Donnell and Gupta [26], incorporated global shape parameters of a super-ellipsoid and generalized cylinder, respectively. Local degrees of freedom are based on elastic properties and the action of external forces. These models can be used to extract gross shape features from visual data, which can be used for indexing into a database of stored models to provide shape recognition. Local deformations help in reconstructing the details of complex shapes to provide shape reconstruction. In related works, Cohen and Cohen [15, 16] used finite-element techniques to implement an elastically deformable cylinder. Later, McInerney and Terzopoulos [50] used physics based techniques to implement an elastically deformable sphere. Whitaker [82], Tek and Kimia [70], Davatzikos and Bryan [18] and others have also done notable work with 3D volumes.

The advantages are:

1. Classic deformable models generally offer a coherent and consistent mathematical description associated with PDE.
2. They are robust to noise and boundary gaps due to smoothness constraint and energy modelling.
3. They offer sub-voxel accuracy for boundary representation.
4. For medical image segmentation, more importantly, they accommodate significant variability of biological structures over time and across individuals.

The disadvantages are:

1. They usually require manual interaction.
2. They work only for surfaces or contours (not real region or volumetric segmentation).

2.4.1 Classic Deformable Models

Classic deformable models are physically motivated, model based techniques for delineating region boundaries using closed parametric curves or surfaces that deform under the influence of internal and external forces. Classic deformable models

gained popularity after they were applied in the computer vision [32] and computer graphics [71] by Terzopoulos and others in 1988.

Mathematically, a classic deformable model moves according to its dynamic equations and seeks the minimum of a given energy function. The deformation of a typical 2D deformable model can be characterized by the following dynamic equation:

$$\mu(s)\frac{\partial^2 X(s,t)}{\partial t^2} + \gamma(s)\frac{\partial X(s,t)}{\partial t} = F_{int} + F_{ext}, \tag{1}$$

where $X(s,t) = X(x(s,t), y(s,t))$ is a parametric representation of the position of a model at a given time t, and $\mu(s)$ and $\gamma(s)$ are parameters representing the mass density and damping density of the model, respectively. Eq. 1 makes the model move in the direction and magnitude of the forces on the right hand side. The most commonly used internal forces are:

$$F_{int} = \frac{\partial}{\partial s}\left(\alpha(s)\frac{\partial X(s,t)}{\partial s}\right) - \frac{\partial^2}{\partial s^2}\left(\beta(s)\frac{\partial X^2(s,t)}{\partial s^2}\right), \tag{2}$$

which represent internal stretching and bending forces. These internal forces are computed as the gradient of an edge map.

2.4.2 Extended Classic Deformable Models

The extended classic deformable models can be divided into three categories: energy minimization snakes, dynamic deformable models and probabilistic deformable models.

Energy-Minimizing snakes

Snake [32, 71] is the most popular form of deformable models among all the classic deformable models. It is a planar deformable contour model whose target is to find a parametric model that minimizes the weighted sum of internal energy and potential energy. The internal energy specifies the tension or the smoothness of the surface of the model. The potential energy is defined over the volume domain and typically possesses local minima at the edge or surface occurring at the object boundaries. It can be mathematically represented as follows.

Let $v(s) = (x(s), y(s))^T$ be a snake embedded in the image plane $(x, y) \in R^2$, where x and y are the coordinate functions and $s \in [0, 1]$ is the parametric domain.

The shape of the contour can be obtained by minimizing energy function given as:

$$E(v) = E_{internal\ energy}(v) + E_{potential\ energy}(v). \tag{3}$$

The internal deformation energy is expressed as:

$$E_{internal\ energy}(v) = \int_0^1 \omega_1(s)|\frac{\partial v}{\partial s}|^2 + \omega_1(s)|\frac{\partial^2 v}{\partial s^2}|^2 ds. \tag{4}$$

Traditionally,

$$E_{potential\ energy}(v) = \int_0^1 P(v(s))ds, \tag{5}$$

where $P(x, y)$ denotes a scalar potential function. In accordance with the calculus of variations, the contour $v(s)$, which minimizes the energy $E(v)$ (Eq. 3) must satisfy the Euler-Lagrange equation.

This vector-valued partial differential equation (PDE) expresses the balance of internal and external forces when the contour rests at equilibrium as shown in the Eq. 6. The first two terms represent the internal stretching and bending forces, respectively, while the third term represents the external forces that couple the snake to the image data.

$$-\frac{\partial}{\partial s}\left(\omega_1(s)\frac{\partial v}{\partial s}\right) + \frac{\partial^2}{\partial s^2}\left(\omega_2(s)\frac{\partial^2 v}{\partial s^2}\right) + \nabla P(v(s,t)) = 0. \tag{6}$$

Dynamic Snakes

It is natural to extend Eq. 6 to a dynamic system by applying the Lagrangian principles. This leads to dynamic deformable models that unify the description of shape and motion, making it possible to quantify not just a static shape, but also shapes evolving through time. A simple example is a dynamic snake, which can be represented by introducing a time-varying contour $v(s) = (x(s), y(s))^T$ along with a mass density $\mu(s)$ and a damping density $\gamma(s)$. The Lagrange equations of motion for a snake with the internal energy given by Eq. 6 is

$$\mu\frac{\partial^2 v}{\partial t^2} + \gamma\frac{\partial v}{\partial t} - \frac{\partial}{\partial s}\left(\omega_1(s)\frac{\partial v}{\partial s}\right) + \frac{\partial^2}{\partial s^2}\left(\omega_2(s)\frac{\partial^2 v}{\partial s^2}\right) = -\nabla P(v(s,t)). \tag{7}$$

The first two terms on the left hand side of this PDE represent inertial and damping forces, while the right hand side represents the external forces.

Probabilistic Deformable Models

Probabilistic deformable models view the deformable models as a fitting process. They incorporate the prior model in terms of a probability distribution, which is usually referred as "Bayesian prior" [23]. After the model is fitted to the image data, the probabilistic model uses a measure of uncertainty of estimated shape parameters [69]. Let μ represent the deformable model shape parameters with a prior probability distribution $p(\mu)$ on the parameters values. Let $p(I|\mu)$ be the probability of producing an image given parameter μ. Bayes theorem states that:

$$p(\mu|I) = \frac{p(I|\mu)p(\mu)}{p(I)}. \tag{8}$$

The internal energy measure of the deformable model (see Eq. 4) is converted into a prior distribution over expected shapes, with lowest energy shapes given the highest probability. This is done using a Boltzmann (or Gibbs) distribution of the form

$$p(\mu) = \frac{exp(-S(\mu))}{Z_s}, \tag{9}$$

where $S(\mu)$ is the internal deformation energy and Z_s is a normalizing constant (also referred as the partition function [3]).

$$p(I/\mu) = \frac{exp(-P(\mu))}{Z_I}, \tag{10}$$

where $P(\mu)$ is a discrete version of the potential energy, which is the function of the image $I(x, y)$.

The fitting of the models is done by finding the μ, which locally maximizes $p(\mu/I)$ in the Eq. 8. This is also known as the maximum a posteriori solution.

2.5 Level Set segmentation

2.5.1 Level Set

Proposed by Osher and Sethian [54], level set methods have attracted increasing attention from researchers from different areas. The level set method and in particular the motion by mean curvature of Osher and Sethian [54] has been used extensively

in problems of curve evolution, because it allows for corners and automatic topological changes. Moreover, the discretization of the problem is made on the fixed rectangular grid.

Let Ω be a bounded open subset of R^2, with the boundary $\partial\Omega$. Let U_0 be a given image, and $C(S) : [0,1] \rightarrow R^2$ be a parameterized curve. The curve C is represented implicitly via the Lipschitz function ϕ, by $C = \{(x,y)|\phi(x,y) = 0\}$, and the evolution of the curve is given by the zero-level curve at time t as the function $\phi(t,x,y)$. Evolving the curve C in the normal direction with speed F by solving the differential equation, we get

$$\begin{cases} \frac{\partial\phi}{\partial t} = |\nabla\phi|F, \\ \phi(0,x,y) = \phi_0(x,y), \end{cases} \tag{11}$$

where the set $C = \{(x,y)|\phi_0(x,y) = 0\}$ defines the initial contour. A particular case is the motion by mean curvature, when $F = div(\frac{\nabla\phi}{|\nabla\phi|})$ is the curvature. The equation becomes

$$\begin{cases} \frac{\partial\phi}{\partial t} = |\nabla\phi|div(\frac{\nabla\phi}{|\nabla\phi|}), \\ \phi(0,x,y) = \phi_0(x,y), \end{cases} \tag{12}$$

where ϕ_0 is an initial level set function.

2.5.2 Level Set based Deformable Model

Level set techniques (also referred as geometric deformable models) started with Sethian's PhD dissertation [63]. There is a well-known relationship between classic deformable models and level set methods. The typical curve evolution equations that are computed as level sets correspond to a reduced version of motion that characterizes a massless snake $\mu(s) = 0$ with no rigidity $\omega_2(s) = 0$. This special case results in snakes that, like conventional level set curves, minimize arc length in the metric induced by the image.

The fundamental difference between geometric deformable models and classic deformable models is:

1. Parametric deformable curves are local methods based on an energy-minimizing curves guided by external and image forces, which pull or push the curves towards features such as edges or surfaces in the image.

2. The classical active contour models solve the objective function to obtain the final boundary, if the approximate or initial location of the contour is available.
3. Geometric deformable methods are active contour energy minimization techniques, which solve the computation of geodesics or minimal distance curves using level set methods. The level set methods are generally governed by the curvature or other speed functions of moving curves or fronts.

A brief review of the geometric deformable methods is given in the following. We broadly classify those geometric deformable methods into three classes:

1. **Geometric Feature Driven Level Sets** are those techniques where the propagation force does not utilize the region-based strategy for its computation. These forces sometimes are called "stopping terms" or "leakage prevention terms". The normally used stopping forces, also called stopping terms, are: gradient, edge, area-minimization, and curvature.
2. **Regional Level Sets** are those techniques where the propagation force utilizes the region-based strategy for its computation.
3. **Variational Level Sets** are those techniques where the level set function is obtained by variational approaches applied to the energy functional. As will be discussed below, this is currently an active area of research.

2.5.3 Geometric Feature Driven Level Sets

Image Gradient

Since image gradient is a very useful geometric image feature, it is first used as driving force, the force to guide the evolution to the final convergency, for level set.

Caselles *et al.* [8], Chopp *et al.* [14] and Rouy *et al.* [60] proposed the gradient based geometric active contours, which is later extended by Malladi *et al.* [49].

The main idea of the model is:

given a 2-D scalar function that embeds the zero level curve, the geometric active contour is given by solving

$$\frac{\partial \phi}{\partial t} = c(x)(k + V_0)|\nabla \phi|, \tag{13}$$

where k is the curvature, V_0 is the constant, and $c(x)$ is the stopping term.

In Caselles *et al.*'s work [8], $c(x)$ is given as $c(x) = \frac{1}{1+|\nabla(G_\sigma(x)*I(x))|}$.

In Malladi's work [49], $c(x)$ is given as: $c(x) = e^{\alpha}|\nabla(G_\sigma(x) * I(x))|$, where α is the gradient constant and $|\nabla(G_\sigma(x) * I(x))|$ is the absolute of the gradient of the convolved image. This convolved image is computed by convolving the original image by the Gaussian function with a known standard deviation σ.

The advantage of the gradient driven level set is:

1. Gradient provides an efficient pulling strength when local gradient is large.

The disadvantages are:

1. The stopping term is not robust and hence may not stop the bleeding or leaking of the boundaries. As mentioned before, this is prime concern because the boundaries of organs in the medical image are typically not clear.
2. The pull back features are not strong. Therefore if the front propagated and crossed the target boundary, it cannot come back.

Edge

Along the direction of gradient driving force, another local image feature, the edge, is then used as a driving force. Kichenassamy *et al.* [33] and Yezzi *et al.* [86] tried to solve the above problems by introducing an extra stopping term, also called the pull back term. This is expressed mathematically as:

$$\frac{\partial \phi}{\partial t} = c(x)(k + V_0)|\nabla \phi| + (\nabla c \cdot \nabla \phi). \tag{14}$$

It is interesting to note that $\nabla c \cdot \nabla \phi$ denotes the projection of an attractive force vector on the normal to the surface. This force is realized as the gradient of a potential field c. Malladi *et al.* in [49] proposed a similar edge based force by adding some constant parameters.

The advantage is:

Compared to the gradient, the force provided is stronger and more robust.

The disadvantage is:

This approach still suffers from boundary leaking for complex structures, as pointed out by Siddiqui *et al.* [64].

Local Neighborhood

Due to the fact that localized feature cannot prevent the leakage properly, the neighborhood information is fused into driving force as presented in [86, 64]:

1. Siddiqui *et al.* [64] thus changed Kichenassamy *et al.* [33] and Yezzi *et al.*'s [86] model by adding an extra term: an neighboring force term. This term is the product of the divergence of the stopping term times the gradient of the flow. This term provides an additional force when the front is in the vicinity of an edge.

$$\frac{\partial \phi}{\partial t} = c(x)(k + V_0)|\nabla \phi| + \nabla c \cdot \nabla \phi + \frac{V_0}{2} x \cdot \nabla c |\nabla \phi|, \tag{15}$$

where $\frac{V_0}{2} x \cdot \nabla c |\nabla \phi|$ is the neighborhood force term.

The disadvantages are:

   (a) Even though it performs better than gradient and edge based techniques, the system is not very robust at handling the convolutedness of medical shapes.
   (b) The system does not take advantage of the regional neighborhood for the propagation or evolution of level sets.

2. Niessen *et al.* [53] proposed a multiple level sets method, which takes advantage of the regional neighborhood. The model is an extension of the geodesic model [49], which will be described in the next section.

   The disadvantages are:

   Even though Niessen *et al.*'s algorithm takes the strength of regional neighborhood, it is not a robust solution since like most of the classic snakes and active contour models, it relies on the edge and gradient to stop the curve evolution. Therefore the algorithm has problem when the image is very noisy and there is no edge as described by Chan and Vese in [10].

Curvature with Directionality

Although the level set originally proposed with curvature as the main force term in front evolving problem, the curvature itself cannot be used as the main force term in a robust image segmentation. Therefore, in image segmentation, the curvature force term is usually used with other forces as shown in previous sections.

However, Lorigo *et al.* [48] proposed an idea using the curvature dependent force integrated with directionality for brain vessel reconstruction based on curve

evolution in 3-D, also know as "codimension 2" in geodesic active contours. The mathematical expression is given as:

$$\frac{\partial \phi}{\partial t} = \lambda(\nabla\phi(x,t), \nabla^2\phi(x,t)) + (\nabla\phi \cdot \nabla I) \times S \times \frac{g'}{g}(H\frac{\nabla\phi}{|\nabla\phi|}), \tag{16}$$

which consists of two components:

1. $\lambda(\nabla\phi(x,t), \nabla^2\phi(x,t))$ (Mean curvature flow) are the eigenvalues of the projection operator: $P_{\nabla\phi}\nabla^2\phi P_{\nabla\phi}$, where $P = I - \frac{qq^T}{|q|^2}$ and q is a nonzero vector. The term is used to derive the Eulerian representation of the level set equation. Eulerian representation of the curve evolution is given by Lorigo *et al.* as: $\frac{\partial\phi}{\partial t} = \lambda(\nabla\phi(x,t), \nabla^2\phi(x,t))$.
2. $(\nabla\phi\cdot\nabla I)\times S\times\frac{g'}{g}(H\frac{\nabla I}{|\nabla I|})$(Directionality of vessels), where g is the edge detector operator and H is Hessian of image. It is the normal of these vessels projected onto the plane. This term is like an angular balloon force, which navigates the deformation process. Normally $\nabla\phi \cdot \nabla I$ is called the directionality term.

The advantages are:

1. The method is robust to noise due to the use of the mean curvature flow.
2. The directional component in the level set framework is very useful in the segmentation of twisted, convoluted and occluded vessels.

The disadvantages are:

1. It is too time consuming since the directional component has to be computed in each iteration.

Although the idea in the paper is very attractive, this paper has very little impact in the field and there have been very few references to it since its publication.

As described above, geometric feature driven level sets primarily focused on modelling the stopping term using different geometric features: curvature, gradient, edge, etc. None of the above methods take advantage of a region-based strategy; hence they are not successful in the capture of the complex shapes of medical organs.

2.5.4 Regional Level Sets

In this section, we describe the design of the propagating force based on a regional strategy, which is fused into the level set fundamental model to improve the robustness of the segmentation for medical imagery. These segmentation systems take advantage of the local and global shape information for pulling and pushing boundaries/surfaces to capture the topology in the level set framework based on PDE. Incorporating such regional-statistics, is also known to make the overall segmentation system more robust and accurate.

2-D Regional Geometric Contour Based on Clustering

Suri *et al.* [65, 66, 67, 68] derived the curve evolution equation by embedding the region statistics into the parametric classical energy model. They obtained the level set function in the form of a PDE as:

$$\frac{\partial \phi}{\partial t} = c(x)(\epsilon k + V_p)|\nabla \phi| - V_{ext} \cdot (\nabla \phi). \tag{17}$$

V_p is considered as a regional force term since it is mathematically expressed as a combination of the inside-outside regional area of the propagating curve.

It is also interesting to note that Eq. 17 has three terms: the product of ϵ and k, V_p and V_{ext}. These three terms are the speed functions, which control the propagation of the curve. These three speed functions are known as curvature, regional, and gradient speed functions.

The advantages of embedding the clustering technique in the level set framework are:

1. The embedding usually leads to robust implementation;
2. With embedding the clustering techniques, the boundary achieved could be more accurate if the class is correctly chosen.

The disadvantages are:

1. The algorithm is not fast enough to be implemented for real-time applications.
2. The performance of the algorithm depends upon a few parameters, such as: the error threshold and the number of iterations.
3. The choice of the initial cluster is important and needs to be carefully selected.
4. The algorithm is not very robust for MR images, which has spatial variations.

3-D Bayesian Classification Constrained Coupled Level Sets

Coupled constrained boundary estimation in the medical imaging has been very successful when applied to shape analysis. In the level set framework, Zeng *et al.* [87] put the level set under constraints in neurological applications. For example, a volume has three tissue types, say TA, TB, and TC, and, tissue TB is embedded in between tissues TA and TC. Such an example is seen in the human brain where the grey matter (GM) is embedded between the white matter (WM) and cortical spinal fluid (CSF). There is a coupling between the WM-GM and GM-CSF volumes. Zeng *et al.* used constrained level sets in the application of human cortex segmentation from MR images. The proposed coupled level set formulation is motivated by the nearly constant thickness of the cortical mantle and takes this tight coupling as an important constraint. The algorithm starts with two embedded surfaces in the form of concentric sphere sets. The inner and outer surfaces are then evolved, driven by their own image-derived information, respectively, while maintaining the volume coupling through a thickness constraint.

The coupled-surfaces propagation with the level set implementation offers the following advantages:

1. The initialization is comparably easy since it can be obtained from the domain prior.
2. The claimed computational efficiency (one hour) is very impressive compared to methods proposed before.
3. The complex sulcal folds, the folds between material entities such as sulci, can be handled by the coupling easily.
4. By the method proposed "skull-stripping" (delineation of non-brain tissues) and segmentation can be done simultaneously.
5. After segmentation, several characteristics of the cortex, such as surface curvature and a cortical thickness map, are already ready to be evaluated.
6. The method integrates the efficiency and flexibility of level set methods with the power of shape constraint.

The disadvantages are:

1. The method does not include a model that deals with image inhomogeneity, unlike other research such as that of Wells *et al.* [81].

2. The technique imposed no constraint to preserve the cortical surface topology. Although it does take advantage of the topological flexibility of level set methods.

3. The resulting surface may not produce a 2-D manifold.

3-D Regional Geometric Surface

Baillard *et al.* [4, 5] designed the brain segmentation system based on the fusion of region into boundary/surface estimation. This algorithm is another instance where the propagation force in the fundamental level set segmentation, Eq. 13, is changed into a regional force. There are three changes made to this equation by Baillard *et al.*.

1. First is in the propagation force V_0.

$$V_0 = sgn\{\alpha_i p_i(u) - (1-\alpha_i)p_e(u)\}, \tag{18}$$

$$sgn(x) = \begin{cases} 1 & if\, x \geq 0\ , \\ -1 & if\, x < 0, \end{cases} \tag{19}$$

   where $p_i(u)$ is a probability density function to be estimated inside the structure, $p_e(u)$ is a probability density function to be estimated outside the structure, and u is the intensity value of a voxel.

   As described in Eqs. 18 and 19, propagation force V_0 utilizes the probability density function inside $(p_i(u))$ and outside $(p_e(u))$ the structure to create a pull/push force on the propagating front.

2. Second change is in the stopping term $c(x)$. Unlike previous methods, which use gradient of the image as stopping term, this method uses the gradient of the probability as the stopping term as shown here:

$$c(x) = g[p_T(x|I, C))], \tag{20}$$

   where

$$g[x] = \begin{cases} 1 - 4x^3 & if\, x < 0.5\ , \\ 4(1-x)^3 & if\, x \geq 0.5, \end{cases} \tag{21}$$

$$p_T = \begin{cases} \frac{(1-\alpha_i)p_e(I(X))}{\alpha_i p_i(I(x))+(1-\alpha_i)p_e(I(x))} & \text{pixel/voxel belongs to the inside,} \\ \frac{\alpha_i p_e(I(X))}{\alpha_i p_i(I(x))+(1-\alpha_i)p_e(I(x))} & \text{pixel/voxel belongs to the outside.} \end{cases} \quad (22)$$

3. The third change is in the step size Δt. Unlike other method, which used fixed Δt, the Δt in this work is defined adaptively to balance the speed and stability.

The advantages of this work are:

1. The work is an excellent example of the fusion of region-based information with the surface.
2. The algorithm is adaptive since the data consistency term $c(x)$ and the step size Δt are adaptively estimated in every iteration of the front propagation. This provides a good tradeoff between convergence speed and stability.
3. Instead of using expectation-minimization (EM), this method uses stochastic-EM (SEM), which is a more robust and accurate method for estimation of probability density function parameters.
4. The algorithm does not use many tuning parameters and thus it is very efficient. The method is designed to control the propagation force using region-based analysis. Baillard *et al.*'s method used pixel-classification based on Bayesian-statistics.

The disadvantages of this work are:

1. Due to use of the pixel-classification based on Bayesian-statistics, the system is very slow although no exact time execution is reported by the author.
2. The accuracy of the system relies heavily on the Bayesian statistics, which relies heavily on the prior information. It is difficult to extend this method to general unsupervised segmentation, where the statistic prior information is unknown.

2D/3D Regional Geometric Surface

Another application of the fusion of Bayesian statistics with the geometric boundary/surface to model the shape in the level set framework is done by Leventon *et*

al. [35]. This method focused on the segmentation of the subcortical area of the brain, such as corpus callosum, and is a good example of the fusion of the boundary and region-based technique. Leventon *et al.* derived the shape information using maximum a posteriori probability (MAP) and fused that with gradient and curvature driven boundary/surface in the level set framework. This MAP model the shape as priors in the Bayesian framework from the training data set.

They used the equation shown in the Eq. 14 with some modifications to the finite difference method,

$$\phi(t+1) - \phi(t) = \lambda_1[(k + V_0)|\nabla\phi| + \nabla c \cdot \nabla\phi] + \lambda_2[\phi^*(t) - \phi(t)], \qquad (23)$$

where $\phi^*(t)$ is computed by MAP.

The advantages are:

1. The method is robust due to MAP used.
2. It is able to successful capture the topology based on the Bayesian shape information.
3. Shape and pose parameters converge to the shape to be segmented by the proposed method.

The disadvantages are:

1. The time taken is relatively long (six minutes for the vertebral segmentation) for spinal navigation, which is supposed to be a real-time application.
2. The system needs training data sets, which are collected off-line.
3. The performance of system, which involves coefficients estimated from training data off-line and application of these estimated coefficients on-line is dependent upon training data and test data sets.

2.5.5 Variational Level Sets

Variational level set method was first proposed by Zhao *et al.* [88]. It has becomes a very popular approach for segmentation. Variational level set combines the energy minimization, which is a very popular method in the physics, with level set methods. In the following, different variational level set methods are introduced.

Zhao *et al.*'s functional

Zhao *et al.* [88] proposed a coupled level set method for the motion of multiple junctions (e.g., of, solid, liquid, and grain boundaries). They use the energy functional consisting of surface tension (proportional to length) and bulk energies (proportional to area) as shown in the Eq. 24. The approach was the first effort on combining the level set method with a theoretical variational formulation.

Assume there are n disjoint regions $\Omega_i (1 \leq i \leq n)$ in the image. The common boundary between Ω_i and Ω_j is denoted as Γ_{ij}. Zhao *et al.*'s obtained by minimizing energy function given by the following:

$$E = \sum_{1 \leq i \leq j \leq n} f_{ij} Length(\Gamma_{ij}) + \sum_{1 \leq i \leq n} v_i \text{Area}(\text{inside}(C_i)). \tag{24}$$

where f_{ij} and Γ_{ij} are constants and C_i is the level set curve enclosing the region Ω_i.

Upon minimizing 24 they obtain the level set function:

$$\begin{cases} \frac{\partial \phi_i}{\partial t} = |\nabla \phi_i| \left(\gamma_i div(\frac{\nabla \phi}{|\nabla \phi|}) - e_i - \lambda \left(\sum_{j=1}^{n} H(\phi_j) - 1 \right) \right), \\ \frac{\partial \phi_i}{\partial \vec{n}} = 0 \ on \ \partial\Omega, \end{cases} \tag{25}$$

where γ_i, e_i and λ are constants, $\vec{n}$ denotes the exterior normal to the boundary $\partial\Omega$, $\frac{\partial \phi}{\partial \vec{n}}$ denotes normal derivative of ϕ at the boundary, and $H(.)$ is the Heaviside function, $div(\cdot)$ is the divergence operator.

The advantage is:

Global energy minimization might lead the level set to converge to the global energy minima.

The disadvantage is:

Only edge and area are used for energy minimization. Therefore the minimization may not lead to a robust segmentation.

Samson*et al.*'s functional

Along the direction of Zhao *et al.*'s functional, Samson *et al.* [61] presented an improved variational approach by adding a minimal variance force. The energy function is given as:

$$E = \sum_{1 \le i \le j \le n} f_{ij} Length(\Gamma_{ij}) + \sum_{1 \le i \le n} v_i Area(inside(C_i)) \tag{26}$$

$$+ \sum_i \int_{\Omega_i} \frac{(u_0 - c_i)^2}{\sigma_i^2} dxdy. \tag{27}$$

The level set function they obtain is:

$$\begin{cases} \frac{\partial \phi_i}{\partial t} = |\nabla \phi_i| \left(\gamma_i div(\frac{\nabla \phi}{|\nabla \phi|}) - e_i \frac{(u_0 - c_i)^2}{\sigma_i^2} - \lambda \left(\sum_{j=1}^{n} H(\phi_j) - 1 \right) \right) \\ \frac{\partial \phi_i}{\partial \vec{n}} = 0 \ on \ \partial\Omega. \end{cases} \tag{28}$$

Due to the minimal variance functional added, the performance of the algorithm is improved.

Mumford-Shah Functional

Chan *et al.* [10] tried to improve above techniques by using a Mumford-Shah modelling based functional. They add a minimal variance term E_{MinVar}. The model is able to detect contours when gradient change is not obvious. The objects with smooth boundaries or even with discontinuous boundaries can be successfully detected. Moreover they claim this model is robust to the position of the initial curve. The 2D version of the model can be expressed as minimization of the following energy function:

$$E(c_1, c_2, C) = \mu \cdot Length(C) + v \cdot Area(inside(C)) + E_{MinVar}, \tag{29}$$

The E_{MinVar} is defined as:

$$E_{MinVar} = \lambda_1 \int_{inside(c)} |u_0(x,y) - c_1| dxdy + \lambda_2 \int_{outside(c)} |u_0(x,y) - c_2| dxdy,$$

where $\mu \ge 0$, $v \ge 0$, $\lambda_1 > 0$ and $\lambda_2 > 0$ are fixed parameters and c_1 and c_2 are the average of u_0 inside and outside C as follows:

$$c_1(\phi) = \frac{\int_\Omega u_0(x,y)H(\phi(x,y))dxdy}{\int_\Omega H(\phi(x,y))dxdy} \tag{30}$$

$$c_1(\phi) = \frac{\int_\Omega u_0(x,y)(1-H(\phi(x,y)))dxdy}{\int_\Omega (1-H(\phi(x,y)))dxdy}. \tag{31}$$

The level set function they obtain is:

$$\begin{cases} \frac{\partial\phi}{\partial t} = \delta_\varepsilon(\phi)[\mu \cdot div(\frac{\nabla\phi}{|\nabla\phi|}) - v - \lambda_1(u_0-c_1)^2 + \lambda_2(u_0-c_2)^2] = 0, \\ \phi(0,x,y) = \phi_0(x,y) \text{ in } \Omega, \\ \frac{\delta_\varepsilon(\phi)\partial\phi}{|\nabla\phi|\partial\vec{n}} = 0 \text{ on } \partial\Omega, \end{cases} \tag{32}$$

where δ_ε is the Dirac delta function.

The advantage is:

Due to the minimization with regional variance, the segmentation is robust and fast. More importantly the segmentation can be achieved when the area has very small gradient changes, which poses a challenge to the previous level set segmentation approach.

The disadvantage is:

It works well on two-region images. However it is not really a Mumford-Shah model driven segmentation since the Mumford-Shah model is the general segmentation model for any images.

Edge Functional

Several approaches have been proposed using an edge based functional.

1. **Geodesic Active Surfaces**

   Kimmel *et al.* [7] proposed a gradient based geodesic active contour/surface functional,

   $$E_{GAC}(S) = \iint g(S)da, \tag{33}$$

   where da is the surface area element and $g(\cdot)$ is an inverse edge indicator function given, for example, by

   $$g(\cdot) = \frac{1}{1+|\frac{\nabla u_0}{\alpha}|^2}. \tag{34}$$

2. **Laplacian Edge Detector Functional**

   Kimmel *et al.* in [34] showed that a Laplacian edge detector provides optimal edge integration with regard to a very natural geometric functional. The functional accumulates the inner product between the normal to the edge and the gray level image-gradient along the edge.

$$E_{LAP} = \iint_s < \nabla u_0, n > da \tag{35}$$

   The advantage is:

   The Laplacian edge detector functional provides a good edge alignment [34] in the vicinity of area where the gradient is large.

   The disadvantage is :

   It can only be used as a regularizer since it is based on the gradient, a localized feature.

Hybrid Functional

It is natural to extend the above work to combine different functionals. Along this direction, the following works have been proposed.

1. In [27], Holtzman-Gazit *et al.* proposed a hybrid model, which combines three functions: Minimal variance functional, Laplacian Edge Detector functional and Geodesic Active Surface functional.

$$E_{total} = -E_{LAP} + \beta E_{MinVar} + \gamma E_{GAC}. \tag{36}$$

   where β and γ are constants.

2. More complicated hybrid model is proposed by Paragios *et al.* [55] for segmentation and tracking of the left ventricle. He combines edge functional, global shape functional and prior shape functional together to get a more robust system for tracking and segmentation.
3. In this thesis, we also use a hybrid model for coupled level sets. The detail will be discussed in next three chapters.

   The advantage is:

Hybrid functional, especially those edge functionals, usually drive the level set converge faster to the edges.

The disadvantage is:

The computational cost could be very expensive.

2.6 Support Vector Machine

SVM has become, in both practice and theory, the classifier of choice of many researchers and practitioners for many real-world classification problems. The main principle was originally introduced by Vapnik [78].

In the following, we briefly introduce two most important features of SVM: optimal margin and structural risk minimization.

Like other linear classifiers, as described in [22, 23], the SVM attempts to evaluate a linear decision boundary or a linear hyperplane between the 2-classes (see Fig. 5 (a)), assuming the data is linearly separable. When the data is not linearly separable in a lower dimensional space it can be mapped to a higher dimension using linear or nonlinear kernels and a linear decision hyperplane is easier to construct. When the nonlinear kernels are used to do the mapping, it is important to choose the right kernel. Typically gaussian or radial basis function kernels are chosen. A detailed description of kernels can be found in [62]. Theoretically, when the data is linearly separable, there are possibly an infinitely many of hyperplanes (see Fig. 5 (b)), which can correctly classify the training data. To obtain the best separation, the SVM attempts to maximize the margin between two classes, as shown in the Fig. 5 (c). Therefore finding the maximum margin separating hyperplane reduces to a quadratic programming problem, see [78] for a complete mathematical formulation and derivation of the solution. More recent progress on SVM can be found in [17, 20, 21].

SVM offers following several advantages, which are typically not found in other classifiers:

1. SVM has a good capacity on generalization, the ability to predict the unseen or unknown samples with a good degree of accuracy, as compared to many traditional classifiers, neural network (NN) for example.
2. Although the training time for original SVM is very high, current progresses in

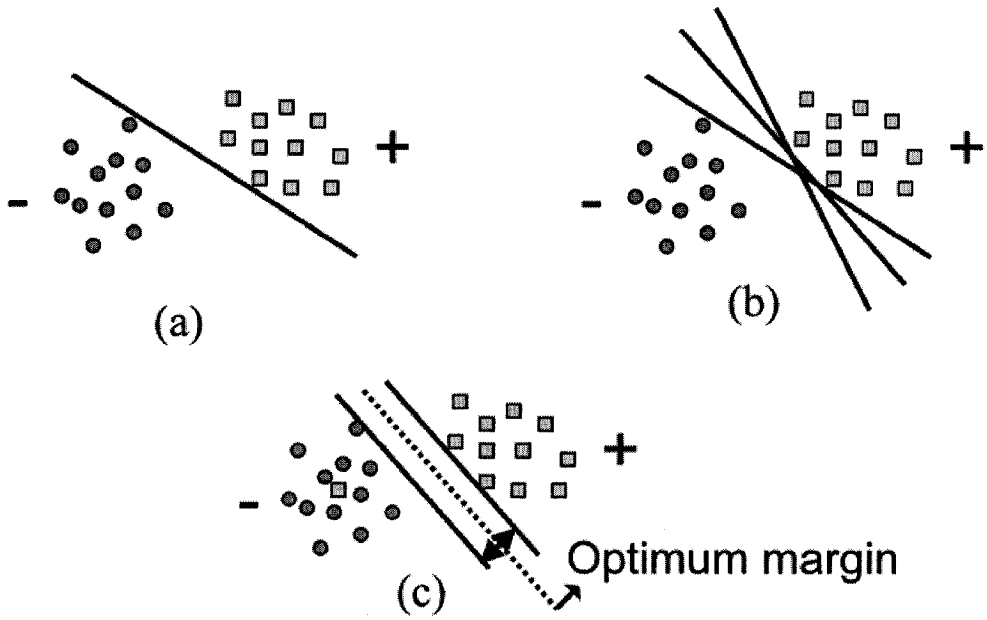

Figure 5: Optimal hyperplane in SVM. (a) Linear hyperplane. (b) Various hyperplanes, which is able to separate the features. (c) Optimal hyperplane found by SVM.

the field has make it computationally much less intensive (esp. in comparison to NN) as shown in [11, 21].

3. Lack of training data is often not a severe problem for SVM.
4. It is based on minimizing an estimate of test error rather than the training error. Together with the optimal margin scheme, it leads to the following advantages:
   (a) SVM is more robust to over-fitting.
   (b) SVM is robust to noise, which severely degrades the performance of NN.
5. SVM does not suffer as much from the curse of dimensionality, which refers to the exponential growth of hypervolume as a function of dimensionality [23]. It performs well in higher dimensional spaces which limits many other efficient classifiers. The computational complexity does not depend on the dimensionality of the feature space. This is also very important for this thesis since feature dimension is usually high in medical image processing and analysis.

Chapter 3

Clinical Level Set Segmentation

"The eternal mystery of the world is its comprehensibility... The fact that it is comprehensible is a miracle."

- Albert Einstein (1879-1955)

3.1 Introduction

Due to the importance of the clinical segmentation, one of the main objectives of this thesis is improving the current clinical medical image segmentation using geometric level set.

Although efficient, level sets are not suitable for clinical segmentation due to several reasons: (1) high computational cost: normally it takes several minutes to do a 2D(100*100) image segmentation; (2) complicated parameters setting: for different types of images, the parameters may need to be set differently; (3) sensitivity to the placement of initial contours, which is shown in the following aspects: (a) the running time of level set method heavily relies on the position and size of the initial curves and the complexity of objects as shown in the Fig. 6; (b) level set do not converge for some initial curves and (c) for some cases, different initial contours may give different segmented results. In the clinic or hospital, it is not realistic to expect a good initial curve from radiologist every time. The details of the above problems and analysis of Fig. 6 will be discussed in the next sections.

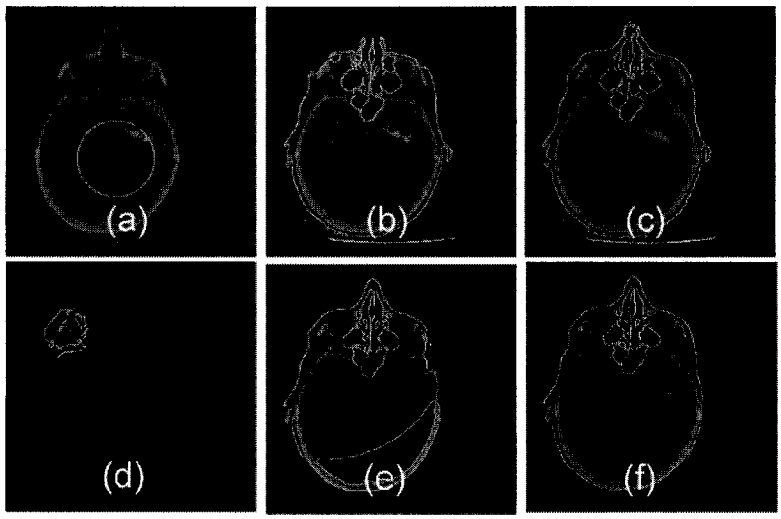

Figure 6: Challenging nose. (a) Iteration 0. (b) Iteration 150. (c) Iteration 350. (d) Iteration 0. (e) Iteration 600. (f) Iteration 1200.

3.1.1 Variational Level Set Method

Proposed by Osher and Sethian [54], level set methods have attracted much attention from researchers from different areas. The detailed survey has been done in the Chapter 2. However to keep the completeness of this chapter, we still briefly recall several closely related variational level set methods, which have been introduced in § 2.5.5.

Variational level set method presently is a very popular approach for segmentation. Variational level set uses the energy minimization, which has been a very popular method for solving physics problems with the level set method. In the following, different variational level set methods are reviewed.

Zhao *et al.* [88] proposed a coupled level set method for the motion of multiple junctions (e.g., of solid, liquid, and grain boundaries). They use an energy functional consisting of surface tension (proportional to length) and bulk energies (proportional to area) as shown in the Eq. 37. This approach combines the level set method with a theoretical variational formulation. Assume there are n disjoint regions $\Omega_i (1 \leq i \leq n)$ in the image. The common boundary between Ω_i and Ω_j is denoted as Γ_{ij}. Zhao *et al.* obtain optimal segmentation by minimizing the functional is given by:

$$E = \sum_{1 \le i \le j \le n} f_{ij} Length(\Gamma_{ij}) + \sum_{1 \le i \le n} v_i Area(inside(C_i)). \tag{37}$$

The level set function they obtain is expressed as:

$$\begin{cases} \frac{\partial \phi_i}{\partial t} = |\nabla \phi_i| \left(\gamma_i div(\frac{\nabla \phi}{|\nabla \phi|}) - e_i - \lambda \left(\sum_{j=1}^{n} H(\phi_j) - 1 \right) \right) \\ \frac{\partial \phi_i}{\partial \vec{n}} = 0 \ on \ \partial\Omega. \end{cases} \tag{38}$$

Chan and Vest [10] proposed a Mumford-Shah functional for level set segmentation. They added a minimal variance term E_{MV}. This model is able to detect contours either with or without a gradient. Objects with smooth boundaries or even with discontinuous boundaries can be successfully detected. Moreover they claim this model is robust to the position of the initial contour. The 2D version of the model can be expressed as minimization of the following energy function:

$$E = \mu \cdot Length(C) + v \cdot Area(Inside(C)) + E_{MV}.$$

with

$$E_{MV} = \lambda_1 \int_{inside(C)} (u_0(x,y) - c_1)^2 dxdy + \lambda_2 \int_{outside(C)} (u_0(x,y) - c_2)^2 dxdy$$

The level set function they obtain is given by

$$\begin{cases} \frac{\partial \phi}{\partial t} = \delta_\varepsilon(\phi)[\mu \cdot div(\frac{\nabla \phi}{|\nabla \phi|}) - v - \lambda_1(u_0 - c_1)^2 + \lambda_2(u_0 - c_2)^2] = 0 \\ \phi(0,x,y) = \phi_0(x,y) \ in \ \Omega \\ \frac{\delta_\varepsilon(\phi)\partial \phi}{|\nabla \phi| \partial \vec{n}} = 0 \ on \ \partial\Omega. \end{cases}$$

The Chan and Vese's functional is very good for segmenting an image into two regions. To segment images with multiple regions, we can use Samson *et al.*'s method, which is one of the earliest reported work using coupled level set. In [61], Samson

et al. presented a variational approach as shown in Eqs. 39 and 40.

$$\begin{aligned} E &= \sum_{1\le i\le j\le n} f_{ij} Length(\Gamma_{ij}) + \sum_{1\le i\le n} v_i Area(Inside(C_i)) \\ &+ \sum_i \int_{\Omega_i} e_i \frac{(u_0 - c_i)^2}{\sigma_i^2} dxdy + \frac{\lambda}{2} \int (\sum_{j=1}^{n} H(\phi_j) - 1)^2 dxdy. \end{aligned} \tag{39}$$

where Γ_{ij} is the intersection of different regions and σ_i is the variance. The level set function obtained is given by

$$\begin{cases} \frac{\partial \phi_i}{\partial t} = \delta_\varepsilon(\phi_i) \left(\gamma_i div(\frac{\nabla \phi}{|\nabla \phi|}) - e_i \frac{(u_0 - c_i)^2}{\sigma_i^2} - \lambda \left(\sum_{j=1}^{n} H(\phi_j) - 1 \right) \right) \\ \frac{\partial \phi_i}{\partial \vec{n}} = 0 \ on \ \partial\Omega. \end{cases} \tag{40}$$

3.2 Challenges in Level Set Segmentation

Although great success has been achieved using level set on medical image segmentation, there are following two main challenges for clinical level set segmentation.

3.2.1 Stopping Criteria

Although compared to the classical deformable model, the level set is more robust to the placement of the initial contour, initial contour placement is still a big challenge for clinical image segmentation using the level set method. The running time of the level set method heavily relies on the position and size of the initial curves and the complexity of objects. As can be seen from Figs. 6(a) to (c), the majority of the objects are segmented in the first 150 iterations while it takes another 200 iterations to segment to the tip of the nose as shown in the Fig. 6(c). Thus it is very difficult for the user to set appropriate stopping conditions, since from iteration 150 to iteration 350, each iteration causes only a few pixel changes. Therefore a too relaxed stopping condition on the number of pixel changes will not able to stop the iterations while a strict stopping condition will stop the iteration before the image is correctly segmented. Figs. 6 (d) to (f) show the iterations needed when different size and position of the initial curve are used. As we can see from Fig. 6, to segment the same image, the number of iterations used varies from about 350 iterations to 1200 iterations when different positions and sizes of initial curves are used while the other parameters are the same. It becomes even worse when complicated structures such

as thin structures, are encountered. Moreover for some cases, level set methods and especially coupled level sets methods, do not converge for some initial curves [10, 27].

3.2.2 Hierarchical versus Coupled Level Sets Segmentation

The level set method naturally divides an image into two regions. Therefore it is very efficient at extracting one object in an image even when the image consists of several disconnected pieces. In order to extract multiple objects, people normally use hierarchical methods [27, 29, 75] or coupled level set methods [19, 47].

Hierarchical Level Set Segmentation

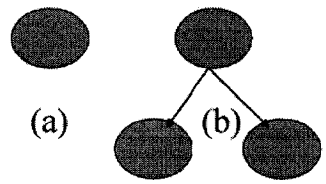

Figure 7: Binary tree representation of hierarchical segmentation: first level segmentation by which, an image (a) is segmented into two regions by the one level set function as shown in (b).

Hierarchical level set segmentation employs an hierarchical approach to extend two region segmentation method to multiple regions segmentation. The idea is described by the binary trees in Figs. 7 and 8. The image is first segmented into two regions by one level set function as shown in the Fig. 7. Then based on the variance analysis of each region, the program decides to further segment one (see Fig. 8 (a and b)) or both regions (see Fig. 8(c)). The procedure is done recursively until the whole image is properly segmented. The advantage of the hierarchical level set is its easy implementation and fast segmentation. By the analysis of the region intensity variance, which measures the deviation from homogeneity of the regions, the hierarchical level set segmentation can easily be used as an automatic segmentation scheme using only one level set function.

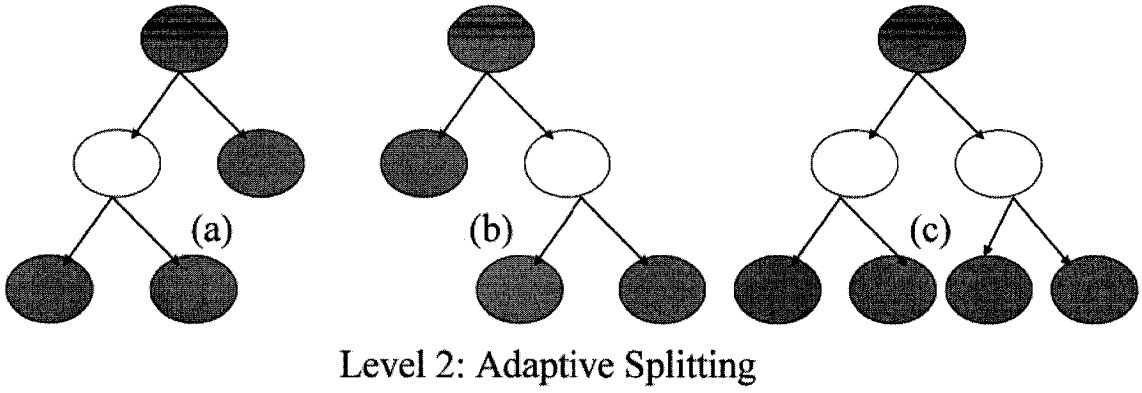

Figure 8: Binary tree representation of hierarchical segmentation: second level segmentation by which, two segmented regions are further segmented into up to four regions. (a) and (b) show that only one of the two regions is further segmented into two regions. (c) shows that both regions are each further segmented into two regions.

Coupled Level Sets Segmentation

In contrast to hierarchical level set segmentation, which uses one level set function recursively to segment one image into multiple regions, coupled level sets segmentation uses multiple level sets simultaneously for multiple region segmentation. The number of the level set functions is equal to the number of the regions in the image as shown in [61, 88].

Advantage versus Disadvantages

Although straightforward and fast, hierarchical segmentations simply assume a single mean inside and outside of zero level. So for multiple objects detection, it tends to be less accurate than coupled level sets. As a result the boundaries may not be optimal. A detailed error analysis is performed and shown in the next section. Coupled level set on the other hand uses one level set function to represent each object. However it is not only slow but it also suffers from the problem of the placement of initial curve, a common problem that exists in the numerical minimization where when functions are non-convex the numerical results may depend on the choice of the initial curves [10, 7]. The placement of initial curve problem can be even worse when the image is noisy.

Error analysis with Bayes model

Although hierarchical level set segmentation is widely used for the segmentation, the accuracy of the obtained boundaries is unknown. In the following, a Bayes model (see § 2.4.2 for more detail about the Bayes theorem) is proposed to analyze the results. A simulation on energy minimization for hierarchical and coupled level set, separately, is performed and compared. In this simulation, data is randomly generated with given means and covariance. We use Bayes decision to calculate the correct decision boundary and benchmark with the decision boundary calculated by the energy minimization. The detailed mathematic description of the Bayesian decision approach can be found in the the book by Duda and Hart [23]. The error measurements are defined as shown in Eqs. 41 to 44. The correct decision boundary is calculated using the Bayesian decision approach.

Eq. 41 shows the energy function (E_c) for three classes: the left class, the middle class and the right class. The grey value range of the three classes is (0, w_1), (w_1, w_2) and (w_2, max) and means of the three classess are μ_{left}, μ_{middle} and μ_{right}. The "max" denotes the maximum grey value in the range. Segmentation is equivalent to finding the correct decision boundaries: w_1 and w_2. Eq. 42 shows the energy function (E_h) for two classes: left class and right class. The grey value range of the two classes is (0, w) and (w, max) and means of them are μ_{left} and μ_{right}.

$$E_c(w_1, w_2) = \int_0^{w_1} (u_0 - \mu_{left})dx + \int_{w_1}^{w_2} (u_0 - \mu_{middle})dx + \int_{w_1}^{max} (u_0 - \mu_{right})dx, \quad (41)$$

$$E_h(w) = \int_0^{w} (u_0 - \mu_{left})dx + \int_{w}^{max} (u_0 - \mu_{right})dx, \quad (42)$$

where w_i are decision boundaries.

Normalized energy $E(x)$ is defined as:

$$E_n(x) = \frac{E(x)}{N}, \quad (43)$$

where N is the total number of pixels.

Two error measurements are defined as:

$$e_1 = \frac{\text{misclassified pixels}}{\text{total pixels of all classes}}, \tag{44}$$

$$e_2 = \frac{\text{misclassified pixels}}{\text{total pixels of neighboring two classes}}. \tag{45}$$

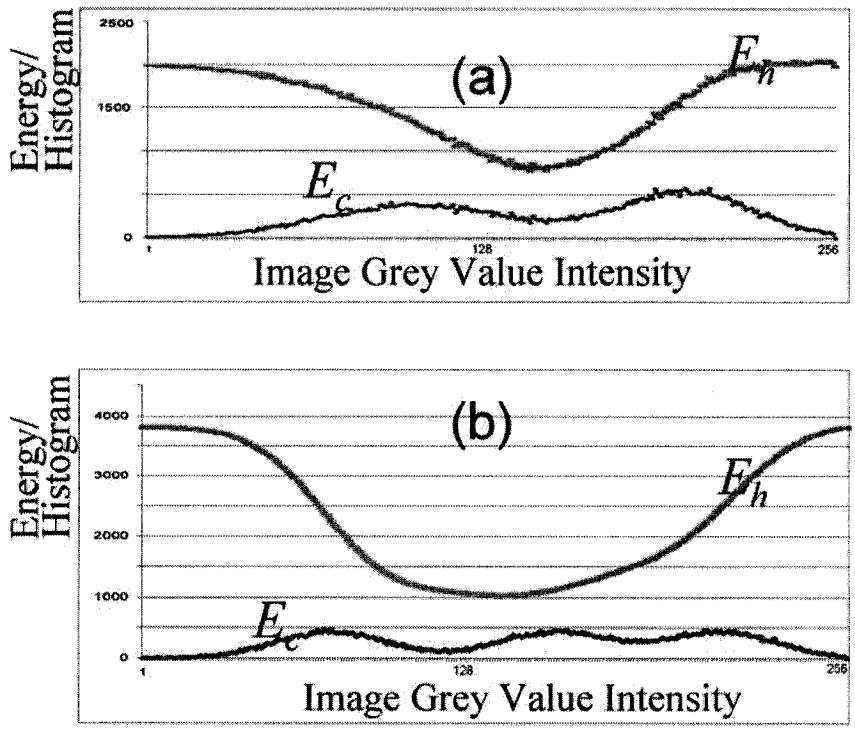

Figure 9: Energy minimization and Bayesian boundary. Top curve: energy curve E_h and E_c.; bottom curve: histogram of the image. (a) Two regions case: first decision boundary by hierarchical energy minimization (e_1= 0.0020; e_2= 0.0020). (b) Three regions case: first decision boundary calculated by hierarchical energy minimization (e_1= 0.0607; e_2= 0.0911).

Fig. 9(a) shows that when there are two classes in the image, energy minimization is able to get a very good decision boundary, which is almost the same as Bayesian decision boundary calculated by the Bayesian approach. However when there are more than two classes, the hierarchical scheme will develop more errors as shown in the Fig. 9(b). Moreover the energy curve in the Fig. 9(b) is not very sharp around the global minima, which means that numerical algorithm may not converge to the

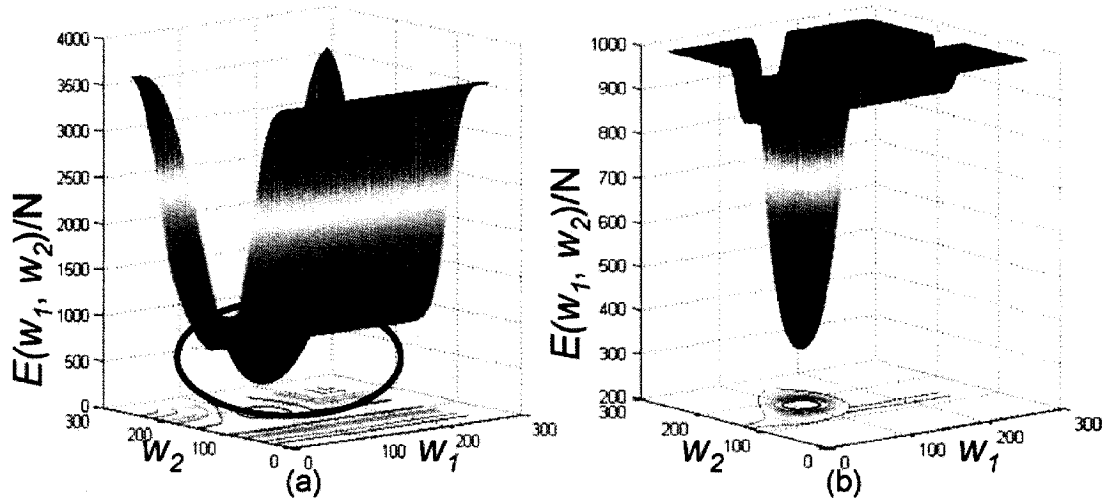

Figure 10: Decision surface of energy function E_c (e_1 = 0.0055; e_2= 0.0082). (a) Global view of the energy surface of E_c. (b) Zoomed view for the cycled part of (a).

global minimum. Fig. 10 shows the energy surface of the Eq. 42. The error is much lower than that for hierarchical level sets. From above we can conclude that coupled level sets tend to find more accurate decision boundaries than those for hierarchical level sets when there are more than two classes in the image.

3.3 Proposed Framework

To overcome the problems described in the above section, a classification based approach is proposed. The approach combines the strength of a classifier, and hierarchical and coupled level set segmentations. In this framework, as shown in the Fig. 11, the framework is divided into following steps:

1. First, sample images or representative slices of volumetric images are segmented by the hierarchical level set segmentation method. The hierarchical method allows detection of multiple objects in an image while limiting the complexity of the computation.
2. Then these results are used to train the pattern classifier. Together with the first step, they form the training stage in Fig. 11. We choose the SVM

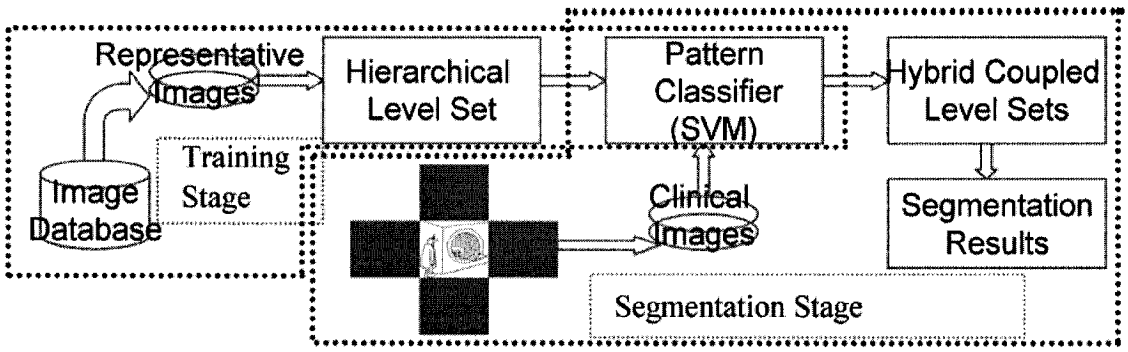

Figure 11: Framework diagram.

as our classifier, which has become increasing popular in pattern recognition and has clear advantages over other pattern classifiers as described in the § 2.6. Therefore the segmentation problem is expressed as a classification problem temporarily. Since medical images usually contain large amount of redundant information for classification, to accelerate the segmentation by SVM, an information reduction scheme is used. SVM training just needs to trained only once. Once the SVM is trained, we can use it to segment the image whenever it is needed.

3. In the clinical setting, the image is first segmented by the SVM as shown in Fig. 11.
4. Lastly, based on the initial curves provided by the SVM, a hybrid coupled level sets segmentation algorithm, which combines Samson *et al.*'s algorithm [61], a optimal edge integrator [34] and the geodesic active contour model is used to give the final fine result as shown in the segmentation stage in the Fig. 11. Although the third step only gives a coarse result, it helps coupled level set curves to find good initial curves. Therefore it takes much less time for coupled curves to converge.

By above framework, with the help of SVM, we naturally combined hierarchical and coupled level set to achieve a fast and robust autonomous medical image segmentation framework for clinical setting.

3.3.1 Hierarchical Region Detection

First the hierarchical level set method described in the § 3.2.2 is used to detect hierarchically how many regions there is in the representative images. The energy function we use is shown in the Eq. 29. Eq. 32 shows the level set function we use as given in the § 2.5.5.

3.3.2 Optimal SVM Training and Segmentation

The results obtained from hierarchical region detection are input into the SVM. A window based feature extraction, as shown in Fig. 12(a), is used to extract features from the regions segmented by hierarchical level set segmentation. The SVM classifier we use is modified from [11]. The brief introduction of SVM can be found in the § 2.6.

Information Reduction Scheme

To accelerate the segmentation by SVM, an information reduction scheme is used.

Medical image contains quite a lot of redundant information for SVM in terms of feature vectors. For example, as shown in the Fig. 12, when we use window feature extraction with 7*7 as the window dimensionality, only 3% of the total features extracted are independent since rest of the 97% are the repetition of these 3%. Therefore for SVM based segmentation, we just need to compute those independent feature vectors. With the help of the hierarchical lookup table, the classification of volumetric image can be greatly accelerated.

3.3.3 Hybrid Coupled Level Sets Segmentation

SVM classification naturally provides good initial contours for coupled level sets. We use one level set function to represent each region. Based on the fact that the boundary segmented by SVM is close to the correct boundary, a hybrid coupled level sets segmentation algorithm combining Samson *et al.*'s algorithm [61], an optimal edge integrator [34] and the geodesic active contour model [7] is proposed as shown in the Eq. 46. A similar functional is used in [27] for a single level set function. The energy function is :

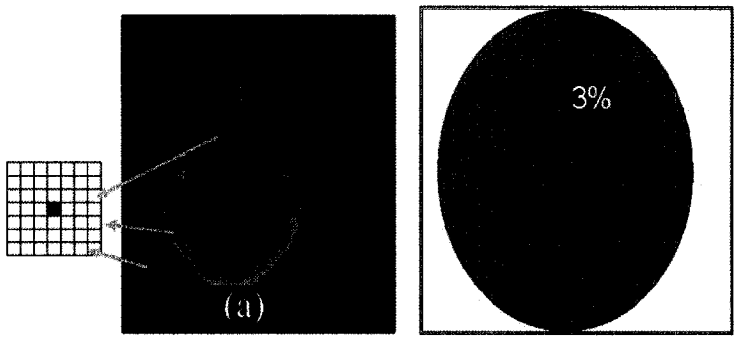

Figure 12: An image and useful information. (a) Original image. (b) Percentage of independent vectors among all the feature vectors in the image (a).

$$E = -\gamma_1 E_{edge} + \gamma_2 E_{coupled} + \gamma_3 E_{GAC}, \tag{46}$$

where γ_i are constants and geodesic active contour (E_{GAC}) is defined as $E_{GAC}(S) = \iint g(S)ds$, where $g(S)$ is an inverse edge indicator function. We use $g(S) = \frac{\alpha^2}{\alpha^2+|\nabla u_0|^2}$ as suggested in [27], where α is a constant. E_{Edge} is the functional proposed in [34] where Kimmel shows that the Laplacian edge detector Δu_0 provides optimal edge integration with regard to a very natural geometric functional as shown in the Eq. 47.

$$E_s(S) = \iint_S < \Delta u_0, n > ds - \iint_{\Omega_S} K|\Delta u_0| dxdy, \tag{47}$$

where S is the evolving contour, K_I is the mean curvature of level sets, n is the unit vector to the curve and is the surface area element. Eq. 48 shows the level set function we use.

$$\begin{aligned} \frac{\phi_i^{t+1} - \phi_i^t}{\Delta t \cdot \delta_\alpha(\phi_i^t)} = \gamma_3 div(g\frac{\nabla\phi_i}{|\nabla\phi_i|}) - \gamma_2 e_i \frac{(u_0 - c_i)^2}{\sigma^2} \\ -\beta\frac{\left(\sum_{i=1}^{K} H(\phi_i) - 1\right)^2}{(u_0 - c_i)^2} - \gamma_1 u_{0\xi\xi}, \end{aligned} \tag{48}$$

where $\delta_\alpha(\cdot)$ is the direct delta function, $u_{0\xi\xi} = \Delta u_0 - K|\nabla u_0|$ and β is constant.

3.3.4 Uncertainty Map

Segmentation divides the image into several homogeneous regions, which ignores localized intensity deviation. However, in medical applications, localized intensity deviation is very important for the analysis and diagnosis. The intensity deviation can be obtained from the uncertainty measurement of the segmentation.

To measure the uncertainty of the segmentation, an uncertainty measurement is proposed as shown in the Eq. 49. The uncertainty measurement consists of two components: a numerical solution uncertainty component ($\psi_1(x,y)$) and a variance uncertainty component ($\psi_2(x,y)$). The $\psi_1(x,y)$ is used to measure the uncertainty of the segmentation to see if the numerical iteration has finished. The $\psi_2(x,y)$ is used to measure intensity deviation inside of the segmented region. Those areas with large intensity changes compared to other areas would have large uncertainty. The larger the value of $\psi(x,y)$, the larger the uncertainty of the segmentation.

$$\psi(x,y) = \psi_1(x,y) \cdot \psi_2(x,y), \tag{49}$$

$$\psi_1(x,y) = \frac{\mathrm{Max}(H(\phi_i))}{\sum H(\phi_i)}, \tag{50}$$

$$\psi_2(x,y) = \frac{\sum |u_0 - c_i| H(\phi_i)}{\sum \sigma_i H(\phi_i))}. \tag{51}$$

The uncertainty map not only gives the user digitized uncertainty of the segmentation results but it also helps to remove the highly uncertain data, which might distract the analysis as will be in the case of the dental X-ray analysis as discussed in § 5.

3.4 Experimental Results

Both two-dimensional and volumetric images were used to evaluate the performance of the proposed framework.

Fig. 13 shows the segmentation using proposed SVM based segmentation. One can notice that in the Fig. 13(a) the boundary found by the SVM is not very accurate. However it provides a good initial contour for the level set segmentation. A comparison of Fig. 6(c) and Fig. 13(d) shows that our framework is able to greatly accelerate level set segmentation such that whereas previously 350 iterations were

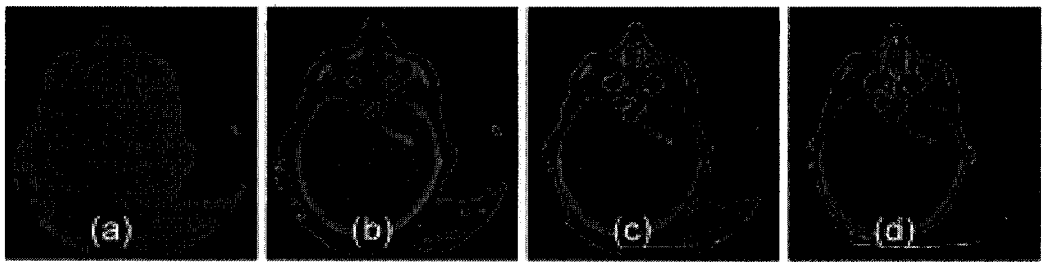

Figure 13: SVM based level set segmentation. (a) SVM based. (b) Iteration 0. (c) Iteration 5. (d) Iteration 15.

needed, 15 iterations are sufficient now. Fig. 14 gives the results of coupled level sets (see Fig. 14(b, c, d)) and proposed framework based segmentation (see Fig. 14(e and f)). The coupled level set segmentation is obtained by manually setting the distribution by assuming the distribution information is known. However it still takes 250 iterations for three coupled level set curves to converge while SVM based segmentation just needs 15 iterations and its uncertainty map is shown in the Fig. 15. The uncertainty map is able guide the users to those high uncertainty areas, which might be areas requiring special attention.

Fig. 16 shows the volumetric segmentation results when one level set function is used. And the Fig. 17 shows the results when our proposed framework is used. As we can see even though the SVM segmentation can only provide a coarse segmentation, it greatly speeds up the level set segmentation. To let internal evolution be visible, some of the volume data are "cut" into two halves as shown in the Figs. 16 and 17. Figs. 18 and 19 provide another example when three coupled level set functions are used. To make the internal part visible, we make some parts of the volumetric data set transparent as shown in the Fig. 18(c) and (d). For the same reason, we directly render the internal skull portion in the Fig. 19 as shown in the Fig. 19(d). Figs. 19 and 20 demonstrate the volumetric segmentation and visualization of a chest CT scan. Fig. 20 shows segmentation procedure performed with four coupled level set functions. Fig. 21 shows the visualization of segmented results done by our proposed framework, which takes only 10 iterations to converge. The volume visualization is done by making the less dense parts part red and partially transparent to make the bones visible.

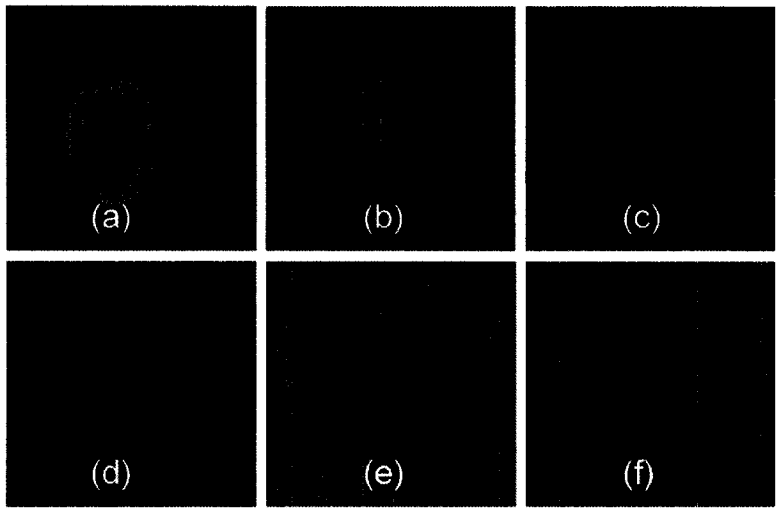

Figure 14: Comparison of coupled level sets (b, c, and d) and proposed framework based segmentation (e and f). To distinguish the results from two methods, different colors are used to color the region. (a) Original image. (b) Iteration 0. (c) Iteration 150. (d) Iteration 250. (e) Iteration 0. (f) Iteration 20.

3.5 Summary

In this chapter, we discuss a new Bayesian model to analyze the error in hierarchical level set and coupled level sets. The error analysis shows that coupled level sets are able to converge to more accurate boundaries even though it takes much longer time to converge. Based on the analysis, an efficient clinical medical image segmentation framework is proposed and implemented by combining a pattern classifier with hierarchical and coupled level set methods. With the aid of techniques from the field of pattern recognition, we naturally combined hierarchical with the coupled level set methods to achieve a fast and robust automatic level set image segmentation framework for clinical setting where the complicated setting for level sets can be transparent to user. The framework is not only able to achieve fast segmentation, but is also able to give a more accurate boundary. To help the clinical radiologist to evaluate the segmentation results, an uncertainty map is computed with a proposed measure of uncertainty. Two-dimensional and volumetric images were used to test the framework. This framework works efficiently in a clinical setting where a specialist works with a limited variety of medical images. The classifier needs to be

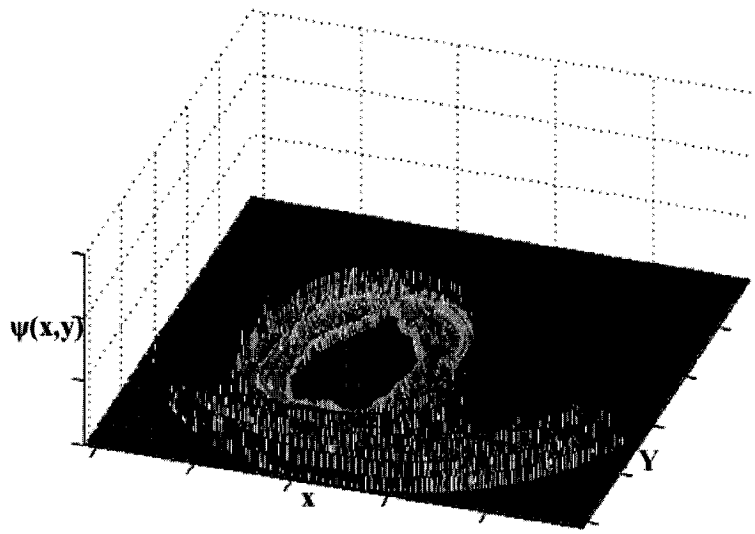

Figure 15: Uncertainty map of Fig. 14(f).

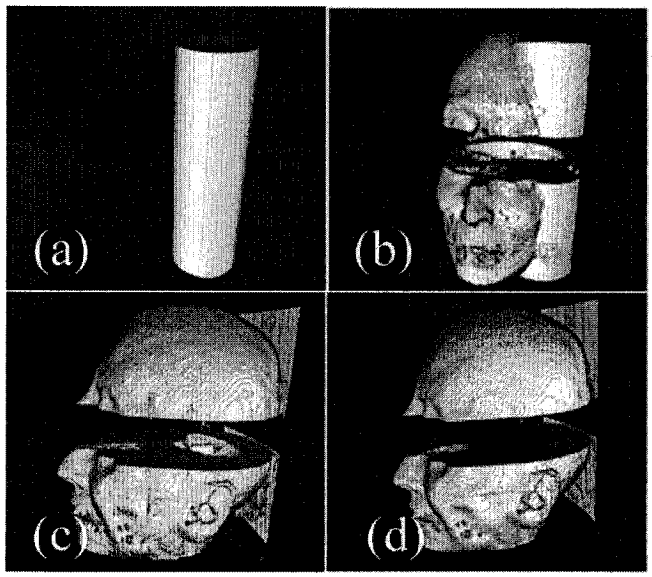

Figure 16: Level set volumetric segmentation. (a) Iteration 0. (c) Iteration 150. (d) Iteration 250.

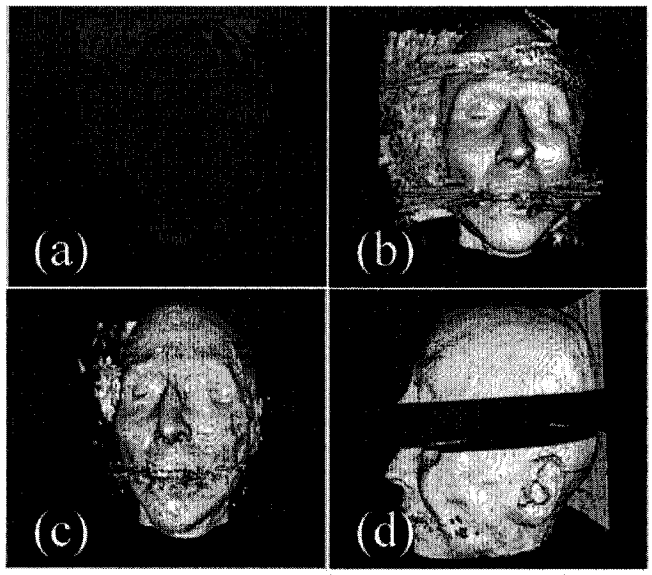

Figure 17: Volumetric segmentation results. (a) Volumetric segmentation by SVM. (b) iteration 1. (c) Iteration 5. (d) Iteration 10.

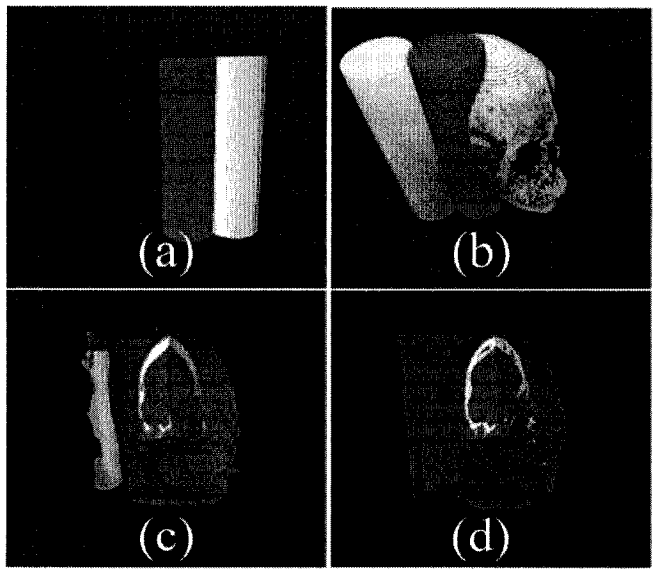

Figure 18: Volumetric coupled level set segmentation results. (a) Iteration 0. (b) Iteration 10. (c) Iteration 50. (d) Iteration 100.

trained only once with representative images or slices segmented by the hierarchical level set method. Then a clinician just needs to indicate to the classifier the image type. Although only the Chan and Vese level set method and Samson *et al.*'s coupled level set method are used to test the framework, the framework can be easily extended to combinations of other level set methods.

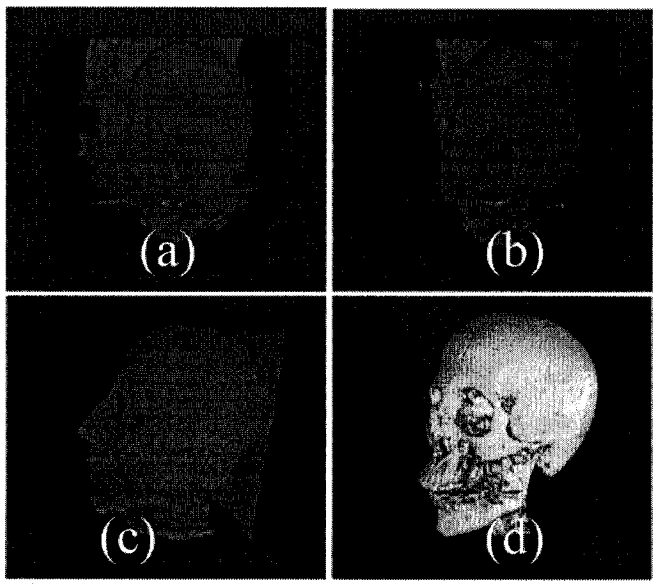

Figure 19: Volumetric segmentation results. (a) Volumetric segmentation by SVM. (b) Iteration 2. (c) Iteration 5. (d) Segmented skull part.

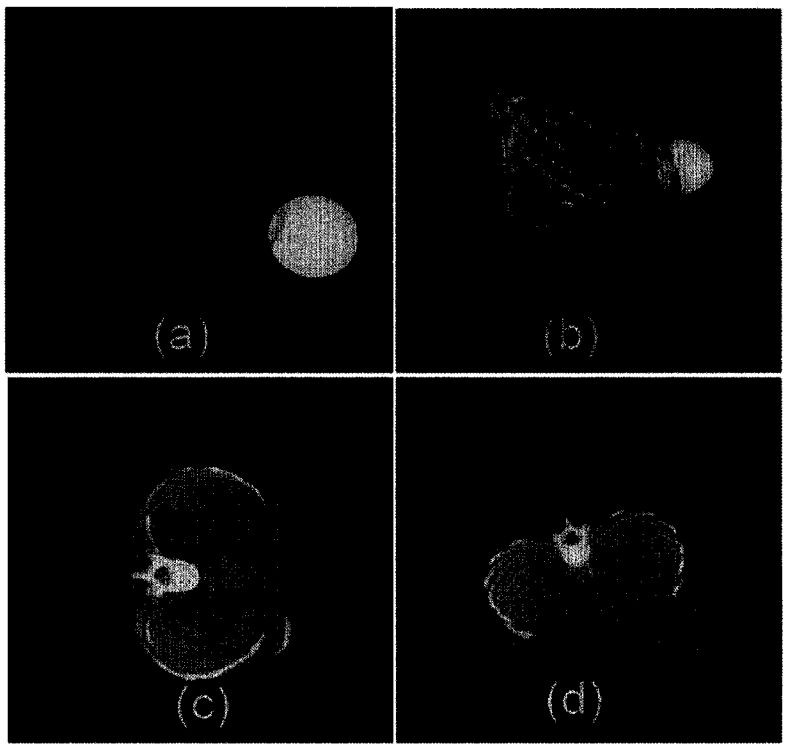

Figure 20: Volumetric segmentation results with four coupled level sets. (a) Iteration 0. (b) Iteration 30. (c) Iteration 80. (d) Iteration 120.

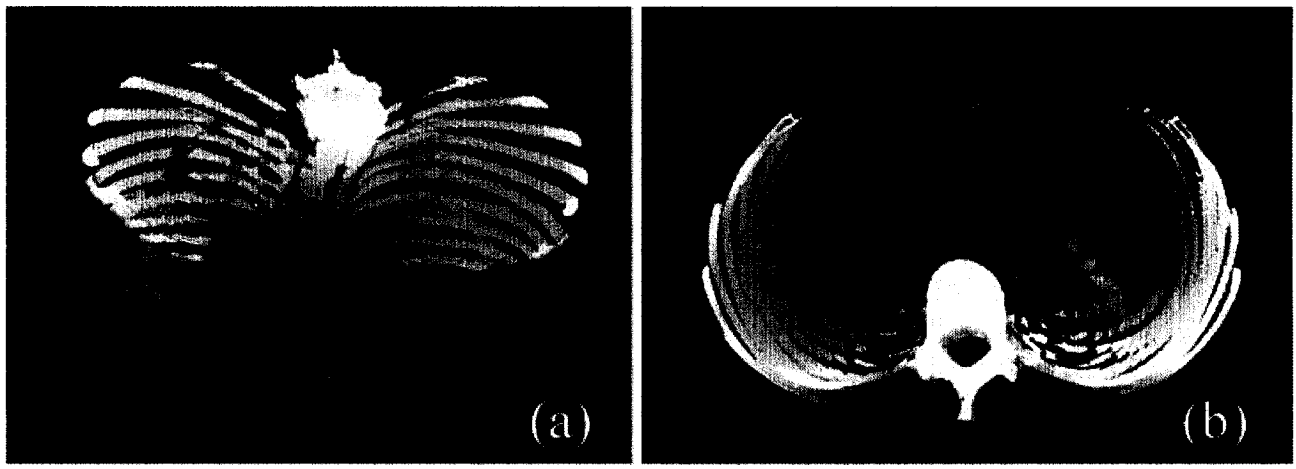

Figure 21: Volume rendering of segmentation results of SVM based level set method and of chest CT images. The flesh area is colored as transparent red. (a) One view. (c) Another view.

Chapter 4

Automatic Clinical Image Segmentation using Pathological Modelling, PCA and SVM

"Give me a museum and I'll fill it."

– Pablo Picasso

4.1 Introduction

Although the work in the Chapter 3 can help to improve the current performance in the clinical segmentation using level set, it still takes some iterations to segment the image, which may not meet the real time requirement. In many clinical applications, it would be ideal to have an even faster segmentation.

For this purpose, this chapter reports on innovative work using machine learning techniques such as the SVM and principal component analysis (PCA) learning with a pathologically modelled variational level set method to address the clinical image segmentation and analysis. As mentioned in the § 3.1, although efficient, level set methods are not directly suitable for clinical image segmentation. Therefore we employ the level set method only during the training stage of the SVM, which limits the effect of the method's slow convergence and lack of stability. Through the pathologically energy functional, we incorporate the pathological modelling with variational level set. Therefore the regions segmented would naturally have pathological meanings. Through the application of PCA, we then use the SVM exclusively

for segmentation, which leads to faster and more robust segmentation. Although the SVM has been used in the medical image segmentation, it is usually used during an intermediate step [36, 37, 80] to accelerate convergence of the segmentation. In this chapter, with appropriate pre-processing, we utilize the SVM to directly segment the medical images.

4.2 Proposed Method

The proposed method consists of two stages: a learning stage and a clinical segmentation stage. During the segmentation stage, a variational level set method driven by a pathologically modelled energy functional is used to segment those manually chosen representative images. This is followed by a window-based feature extraction using PCA analysis. The extracted features are used to train an SVM. During segmentation of images in the clinical setting, the clinical image is then directly segmented by the trained SVM.

4.2.1 Pathologically Modelled Variational Level Set Method

In this work, we apply the variational level set method to segment the representative images. First, with the assistance of a radiologist or clinician, the energy functional will be modelled according to the pathological characteristics of the different regions in an image. In the following, we are going to take chest CT (2D and 3D) scans and dental X-ray images as examples as can be seen in Figs. 22 and 23.

Chest CT Scans

Fig. 22 demonstrates a pathological modelling for chest CT scans. The images can be divided into four regions of interest: the Background Region (Ω_{BR}), the Skeletal Structure (bone) Region (Ω_{SR}), the Fatty Tissue Region (Ω_{FR}) and the Muscle and Visceral Tissue Region (Ω_{MR}). Energy functional for the four coupled level set functions are modelled as shown in the Eq. 52.

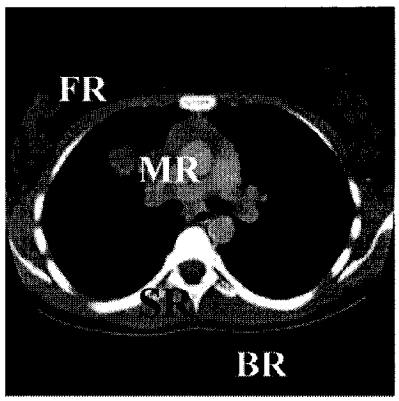

Figure 22: Pathological modelling for chest CT scans. The chest CT image can be divided into four regions: Ω_{FR}, Ω_{MR}, Ω_{SR}, and Ω_{BR}.

$$E_{MV}(\phi_i) = \int_{\Omega_{BR}} \frac{e_1(u-c_{BR})^2}{\sigma_{BR}^2} dxdy + \int_{\Omega_{FR}} \frac{e_2(u-c_{FR})^2}{\sigma_{FR}^2} dxdy + \int_{\Omega_{SR}} \frac{e_3(u-c_{SR})^2}{\sigma_{SR}^2} dxdy + \int_{\Omega_{MR}} \frac{e_4(u-c_{MR})^2}{\sigma_{MR}^2} dxdy \quad (52)$$

where c_i, i=1,...,4, is the mean grey value of region Ω_i.

Dental X-rays

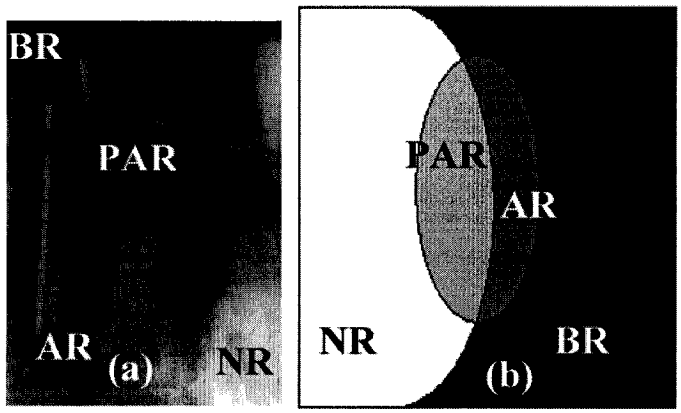

Figure 23: Pathological modelling of dental X-ray. The dental X-ray image can be divided into four regions: Ω_{NR}, Ω_{PAR}, Ω_{AR}, and Ω_{BR}.

With prior information of the pathology associated with possible diagnosis, this pathological modelling can also be used for computer aided diagnosis. As shown in

the Fig. 23, X-ray images can be divided into four regions of interest: the Normal Region (Ω_{NR}), the Potentially Abnormal Region (Ω_{PAR}), the Abnormal Region (Ω_{AR}) and the Background Region (Ω_{BR}). Since Ω_{AR} and Ω_{BR} are not separable in terms of intensity values, so in the segmentation, we take Ω_{AR} and Ω_{BR} to be one region: the Abnormal and Background Region (Ω_{ABR}). Energy functional for three coupled level set functions are modelled as shown in the Eq. 53.

$$\begin{aligned} E_{MV}(\phi_i) &= e_1 \int_{\Omega_{NR}} \frac{(u - c_{NR})^2}{\sigma_{NR}^2} dxdy + e_2 \int_{\Omega_{PAR}} \frac{(u - c_{PAR})^2}{\sigma_{PAR}^2} dxdy \\ &\quad + e_3 \int_{\Omega_{ABR}} \frac{(u - c_{ABR})^2}{\sigma_{ABR}^2} dxdy. \end{aligned} \tag{53}$$

4.2.2 Hybrid Variational Level Set

To achieve a fast and robust coupled level set segmentation, a hybrid variational functional is used. The hybrid coupled level set functional combines Samson's algorithm [61], an optimal edge integrator [34] and a geodesic active contour model [7]. Therefore, the final energy functional is

$$E = E_{MV}(\phi_i) - \gamma_1 E_{LAP} + \gamma_2 E_{GAC} \tag{54}$$

where γ_i are constants.

The level set function derived from the functional is shown in the Eq. 55.

$$\begin{aligned} \frac{\partial \phi_i}{\partial t} &= \gamma_2 \delta_\varepsilon(\phi_i) div(g \frac{\nabla \phi_i}{|\nabla \phi_i|}) - e_i \delta_\varepsilon(\phi_i) \frac{(u - c_i)^2}{\sigma_i^2} \\ &\quad - \beta \delta_\varepsilon(\phi_i)(\sum_{i=1}^{k} H(\phi_i) - 1)^2 - \gamma_1 \delta_\varepsilon(\phi_i) u_{\xi\xi}, \end{aligned} \tag{55}$$

where $u_{\xi\xi} = \Delta u - K_I |\nabla u|$.

Since the proposed pathological modelling explicitly incorporates regions of problems as part of the modelling, the identification of such areas would be an automatic byproduct of the segmentation. Through the use of the uncertainty map introduced in § 3.3.4, we can also gauge the degree of severity of such problem regions.

4.2.3 Learning

As shown in the Fig. 24, the learning phase consists of several steps. First, manually chosen images are segmented by the variational level set described in the § 4.2.1. To avoid distraction, the high uncertainty areas are removed, with the assistant of the uncertainty map introduced in § 3.3.4. Next, window-based feature extraction is applied. The results will be used to train the SVM after applying PCA learning to extract features.

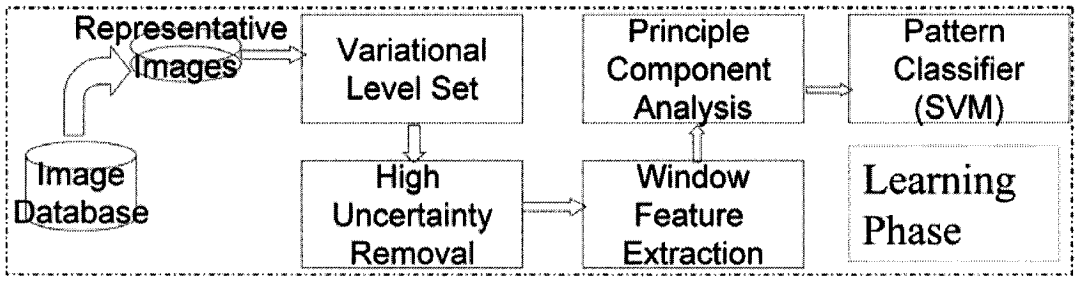

Figure 24: Learning phase diagram.

Uncertainty Removal

Before feature extraction, those areas of high uncertainty in the segmented image will be removed. The uncertainty measurement proposed in the § 3.3.4 is used to build the uncertainty map.

Feature Extraction and Principal Component Analysis

A window-based feature extraction was applied to each segmented region in the image. This is illustrated in the Figs. 25 to 27. The whole feature extraction is shown in the Fig. 25. Fig. 26 shows some of the feature samples extracted. The samples of average patch and eigenpatch are shown in the Fig. 27. The PCA method used here is adapted from [76, 77]. Let the features Γ_i $(i = 1..M)$ constitute the

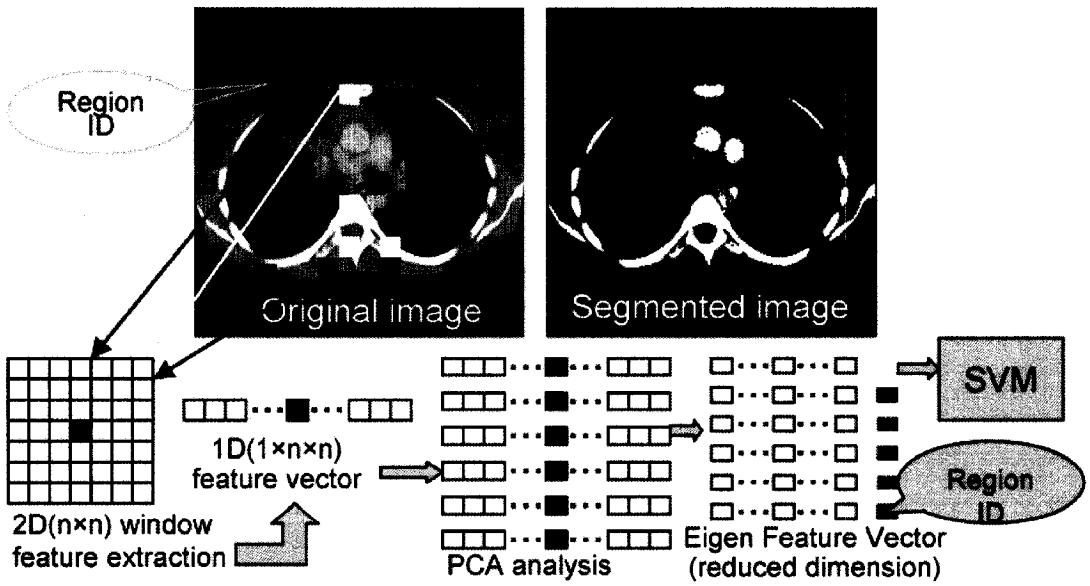

Figure 25: Feature extraction diagram.

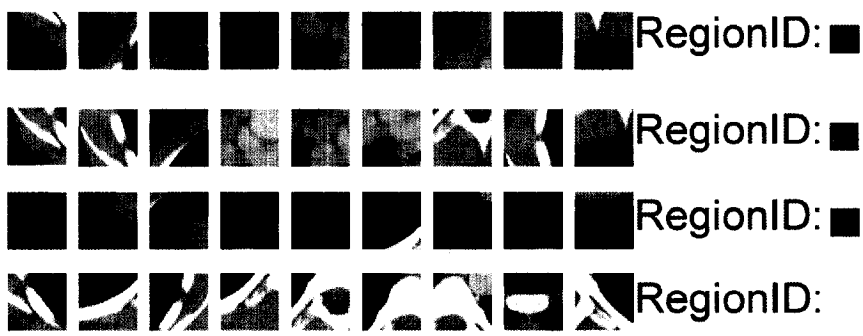

Figure 26: Window based features.

training set (Γ). The average matrix ($\overline{\Gamma}$) and covariance matrix C are:

$$\begin{aligned}
\overline{\Gamma} &= \frac{1}{M}\sum_{i=1}^{M}\Gamma_i \\
\Phi_i &= \Gamma_i - \overline{\Gamma} \\
C &= \frac{1}{M}\sum_{i=1}^{M}\Phi_i^T\Phi_i = AA^T \\
L &= A^TA(L_{n,m} = \Phi_n^T\Phi_m) \\
u_i &= \sum_{k=1}^{M} v_{ik}\Phi_k(l = 1, \ldots, M)
\end{aligned} \tag{56}$$

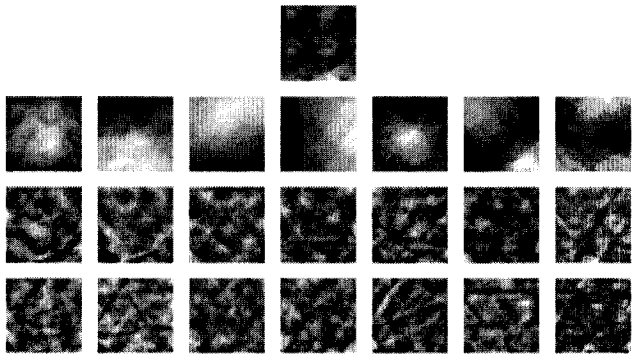

Figure 27: Average patch (first row) and eigen patches.

where L is a $M \times M$ matrix, v_{ik} are the M eigenvectors of L and u_i are eigen-patches, which were called eigenfaces in [76, 77]. The advantage of the PCA approach here is its ability to remove the effects of noise and also to accelerate the classification by reduced feature dimension.

SVM Training and Segmentation

The strength of the SVM classifier has been demonstrated in many research areas such as handwriting recognition application, which is described in Dong *et al.*'s [20, 21]. The features extracted from the eigen-patches are used to train the SVM. The classifier we use is a modified version of the SVM classifier proposed in [11].

4.3 Results

To evaluate the proposed method, both chest CT scans (two-dimensional and three-dimensional images) and dental X-ray images are used to test the proposed method.

4.3.1 Chest CT Scans

Two-dimensional Scans

Figs. 28 and 29 show the results of two-dimensional image segmentation. Fig. 28 shows the results of pathological variational level set segmentation, which divides the image into four regions of background, the skeletal structure (bone), the fatty tissue, and the muscle and visceral tissue, as defined in the § 4.2.1. However the variational level set method is a time consuming method, which generally takes

longer than 10 minutes to segment a 256 × 256 image for a PC (Pentium 1G Hz and 1G RAM). Fig. 29 demonstrates the segmentation results using the proposed method, which just takes around 1 second.

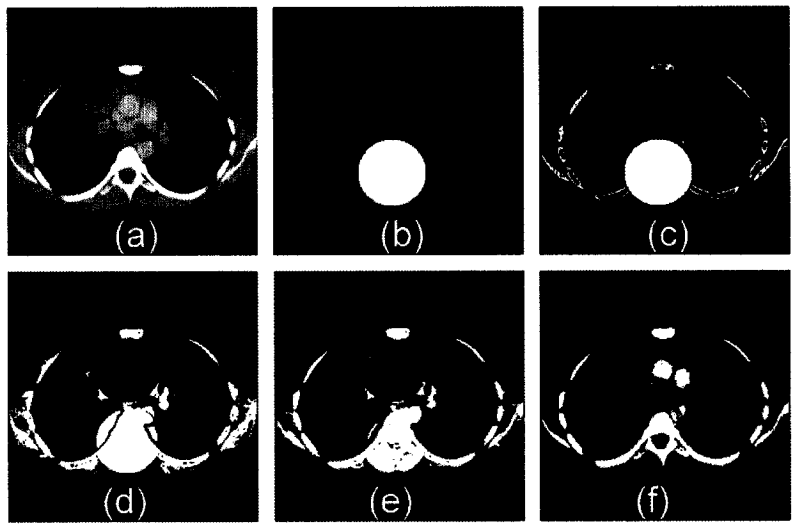

Figure 28: Experimental results on CT scans. (a) Iteration 0. (b) Iteration 20. (c) Iteration 50. (d) Iteration 100.(e) Iteration 125. (f) Iteration 150.

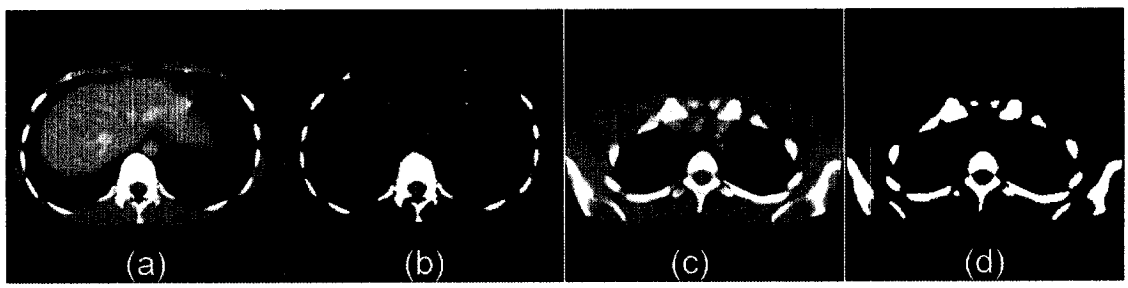

Figure 29: Experimental results on CT scans. (a) (c) Original images. (b) (d) Segmented images.

Three-dimensional Scans

Figs. 30 and 31 show results on three-dimensional image segmentation. Fig. 30 shows variational level set segmentation on volumetric CT scan image (256 × 256 × 100), which usually takes longer than two hours while with our proposed method takes around 20 seconds.

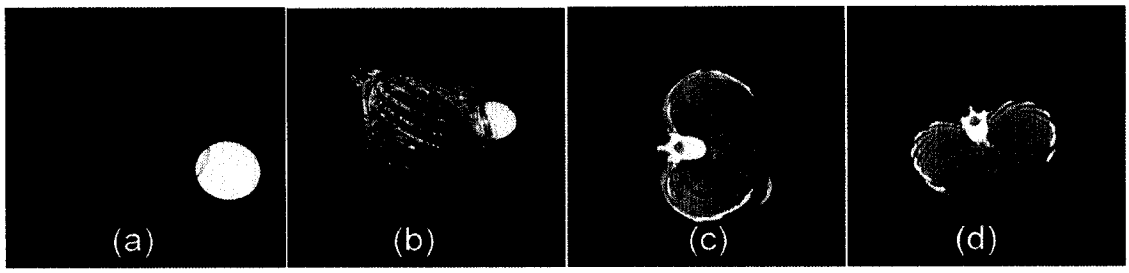

Figure 30: Volumetric coupled level set segmentation results. (a) Iteration 0. (b) Iteration 30. (c) Iteration 80. (d) Iteration 120.

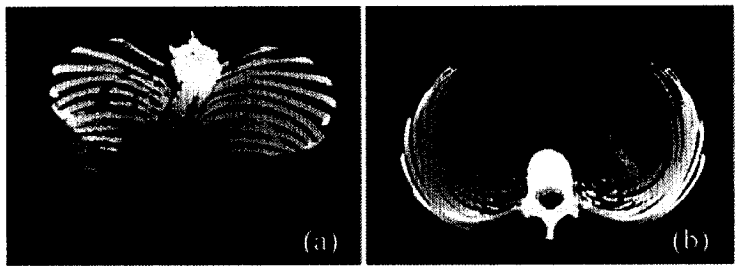

Figure 31: Volume rending of segmentation results of using proposed method on chest CT scans. (a) One view. (b) Another view.

4.3.2 Dental X-ray Images

As described before, dental X-ray segmentation is a challenging problem for classic methods due to the following characteristics: (1) poor image modalities: noise, low contrast, and sample artifacts; (2) complicated topology; and (3) there may not be clear edges between region of interest, which is especially true for dental images with early stage problem teeth. Fig. 32 demonstrates the variational level set segmentation described in the § 4.2.1 on dental X-ray images. As can be seen, the variational level set method is able to successfully segment the image using the given pathological modelling, which provides automatic feature extraction for PCA and SVM training. Fig. 33 shows the results by the proposed method. Since pathological modelling explicitly incorporates regions of problems as part of the modelling, the identification of such areas is an automatic byproduct of the segmentation.

4.4 Summary

Due to the presence of complicated topological and residual features, the segmentation of medical imagery is a difficult problem. In this chapter, an automated

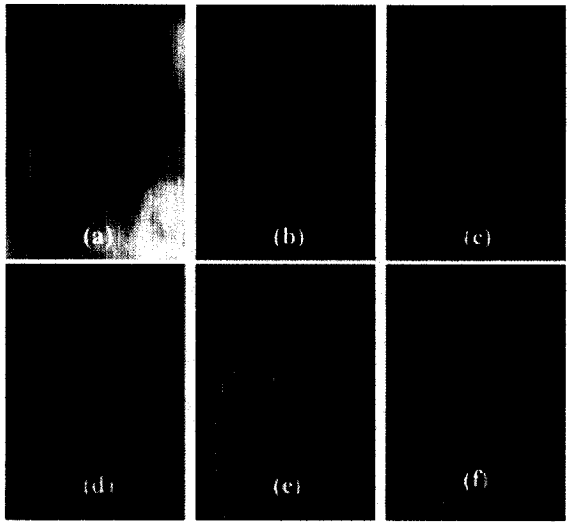

Figure 32: Coupled level sets segmentation. (a) Original image. (b) Iteration 0. (c) Iteration 50. (d) Iteration 100. (e) Iteration 200. (f) Iteration 250.

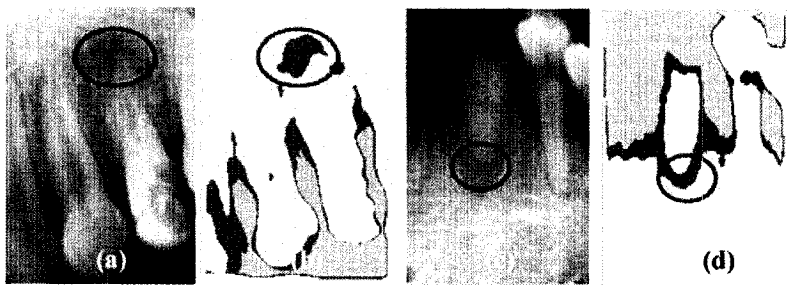

Figure 33: Experimental Results on Dental X-rays. (a) (c) Original image with problem area circled by dentist. (b) (d) Segmented image with problem area circled manually for attention.

approach to clinical image segmentation has been presented. The processing of these images in our approach is divided into learning and segmentation stages to facilitate the application of PCA with a SVM classifier. During the initial learning stage, representative images are chosen to represent typical input images. These images are segmented using a variational level set method driven by a pathologically modelled energy functional designed to delineate the pathological characteristics of the images. Then a window-based feature extraction is applied to these segmented images. Principal component analysis is applied to these extracted features and the results are used to train an SVM classifier. After training the SVM, any time a clinical image needs to be segmented, it is simply classified with the trained SVM. By the proposed method, we take the strengths of both machine learning and the

variational level set method while limiting their weaknesses to achieve automatic and fast clinical segmentation. To test the proposed system, both chest CT scans (2D and 3D) and dental X-rays are used. Promising results are demonstrated and analyzed. The proposed method can be used during pre-processing for automatic computer aided diagnosis.

These results show that the proposed method is able to provide a fast and robust clinical image segmentation of both 2D and 3D images. Due to the use of pathological modelling to define the regions of interest, the segmentation results can be used to further analyze the image. The proposed method can be used as pre-processing step for automatic computer aided diagnosis. We will continue exploring this idea in the next chapter.

Chapter 5

Computer Aided Dental X-ray Analysis

"I believe the present fashion of applying the actions of physical science to human life is not only a mistake but has something reprehensible about it."

– Albert Einstein (1879-1955)

5.1 Introduction

The past few years have seen a great increase in the usage of digital dental X-ray, which is the important way to detect periodontitis (commonly known as "gum diseases") and bone loss that cannot be seen during a visual examination in dental practices.

The benefits of digital x-rays include:

1. Reduced waiting time: Digital x-rays are available very quickly and can be displayed on the computer screen almost immediately after. This saves the time to process film.
2. High resolution image: Comparing to classic X-ray film, digital X-rays provide much high resolution image. With the higher resolution digital X-ray of sections of the teeth, or of the entire jaw, comes the possibility of more accurate diagnoses.
3. Safer radiation exposure: Sensors in digital X-ray systems are more sensitive than X-ray film systems, resulting in up to a 90% reduction in a patient's exposure to X-ray.

Moreover with the fast development of digital dental X-ray machine, the dental X-ray is not only becoming cheaper and more convenient but since they are accessible electronically, this makes computer aided dental X-ray analysis possible, convenient and efficient. All these provide the opportunities and challenges for the development of computer aided dental X-ray analysis.

Besides being used for clinical purposes, dental X-ray is also widely used in the forensic identification. Jain *et al.* [13, 24, 28] are developing an automatic human identification system using dental X-ray.

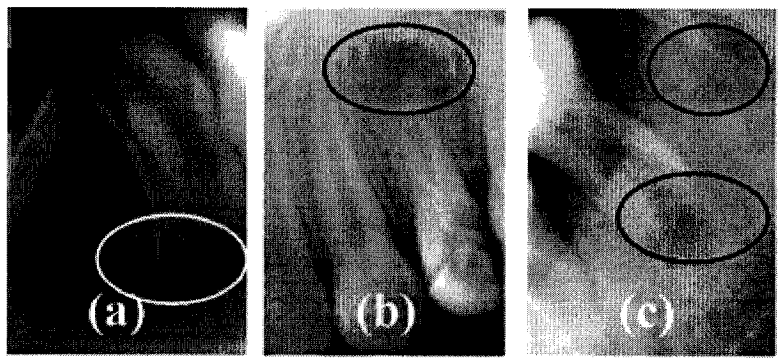

Figure 34: Dental X-ray samples.

However, although dental X-ray are widely used, it is a challenging task to do automatic, or even semi-automatic, computer aided dental X-ray analysis. As shown in the Fig. 34, as compared with other types of images, dental X-ray analysis is a challenging problem for classic image processing methods due to the reasons discussed earlier in § 4.2.1 with the additional complication of arbitrary teeth orientation. Therefore the dental X-ray is normally inspected by a dentist. Although efficient, human inspection requires specialized training and a dentist's time, which is increasingly expensive. Moreover, human inspection gives a subjective judgment, which may vary from person to person, and, as such, does not give a quantitative measurement. Inspection results could be affected by many factors, such as fatigue and distraction by other features in the image, for example. Also, some early bone loss may not be visible to the human eye. All of these issues indicate a need for effective automatic or semi-automatic dental X-ray analysis. In Chapter 4, level set segmentation method has been used for dental X-ray images. The segmentation method employs three coupled level sets driven by a proposed pathologically variational modelling. The work also demonstrated the segmentation results has can be

used for further clinical diagnosis.

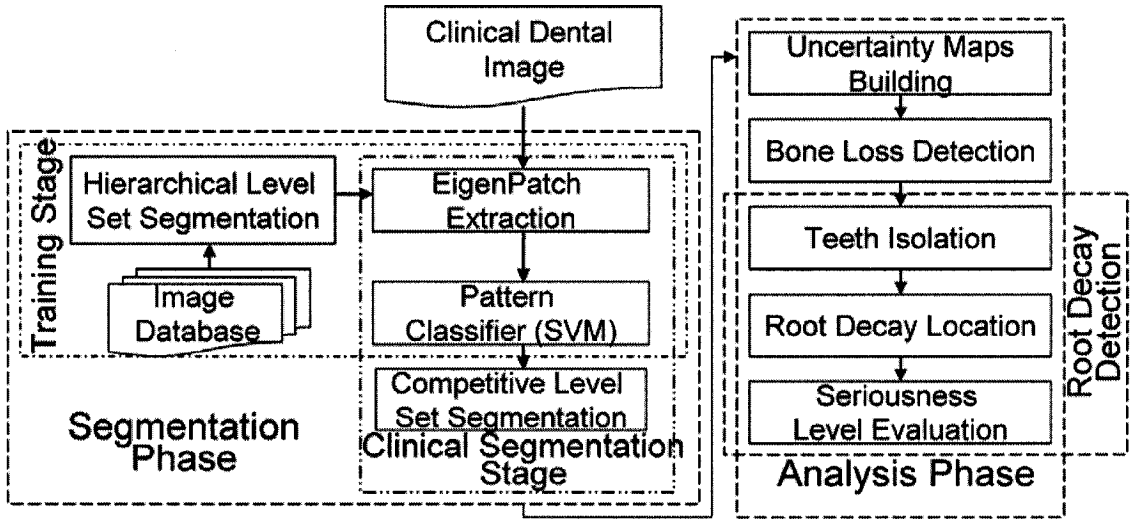

Figure 35: Framework diagram.

In this chapter, we describe an innovative work on semi-automatically providing indications to the dentist to aid in finding areas of bone loss in teeth or the jaw and to help detect root decay, which are the primary reasons that X-ray is taken in many countries. Early detection of bone loss and root decay is very important since often they can be remedied in the early stage by dental procedures, such as a root canal, for example. Without early treatment, bone loss may lead to tooth loss or erosion of the jaw bone. Although the approach developed here can be applied to other types of dental X-ray, we will be dealing primarily with periapical X-rays, which are close-up views of a few individual teeth including the root and surrounding bone. Periapical X-ray is very useful in diagnosing an abscess, impacted tooth or bone loss due to periodontal disease. Compared with panoramic dental X-ray, which include the entire jaw region, periapical X-ray taken for these purposes are more challenging since the orientation of the teeth may not be fixed and problem areas are either complicated, as shown in the Fig. 34(a), or easily overlooked, as shown in the circled areas in the Fig. 34(b) and (c). These factors complicate the use of traditional image processing methods. Therefore we employ our clinical level set segmentation framework developed in Chapters 3 and 4 using pathologically modelled level set functions for segmentation due to its ability to capture the topology of shapes in medical imagery and its robustness to noise. The benefit of using level set segmentation on dental X-rays in particular will be discussed in detail in the

§ 5.2.

To analyze the dental X-ray to determine areas of decay, adapting the framework presented in Chapters 3 and 4, a semi-automatic computer aided dental X-ray analysis framework is proposed. The diagram of the proposed framework is shown in the Fig. 35. As shown in the Fig. 35, the proposed framework consists of two phases: segmentation and analysis. Segmentation phase again contains two stages: training and clinical segmentation. The analysis phase contains three steps : uncertainty map building, bone loss detection and root decay detection. To the best of our knowledge, we are the first group working towards automatic computer aided dental X-ray diagnosis for the detection of bone loss and root decay using the level set method. This chapter reports on our preliminary results towards this goal.

5.2 Variational Level Set and Dental X-ray

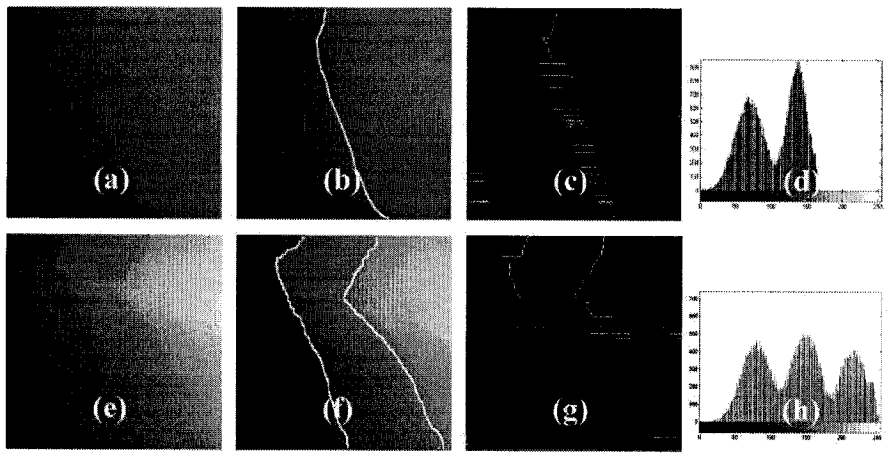

Figure 36: (a) Original image. (b) Variational level set segmentation by [10]. (c) Results by Sobel edge detection. (d) Histogram image of (a). (e) Original image. (f) Variational level set segmentation by [61]. (g) Results by Sobel edge detection. (h) Histogram image of (e).

As described in previous chapters, the variational level set method naturally segments the image according to the energy functional. Due to this characteristic, as shown in the Fig. 36, a variational level set method is able to detect a boundary where traditional methods fail. Moreover, the variational level set method is very robust to noise (see Fig. 37), which presents serious challenge to many traditional

image processing techniques on dental X-ray as shown in the Fig. 38. The variational level set method is very robust to noise, compared with the gradient based classic image processing method. Even when the amount of the noise is very high (σ = 40), the variational level set method can still determine the correct segmentation as shown in the Fig. 37.

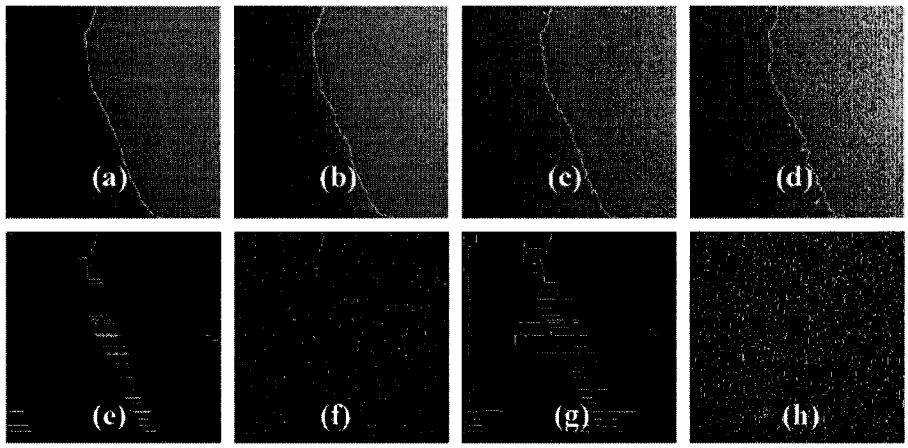

Figure 37: Noise robustness. (a-d)are variational level set segmentation by [10] ((a) noise level σ (variance of the noise) = 10; (b) noise level σ = 20; (c) noise level σ = 30; (d) noise level σ = 40.). (e-f) edge detection by Sobel edge detection ((e) noise level σ = 10; (f) noise level σ = 20.). (g-h) are edge detection by LOG ((g) noise level σ = 10; (h) noise level σ = 20).

5.3 Proposed Framework

For the proposed framework, we first employ level set methods to segment the image into three regions: Normal Region (NR), Potentially Abnormal Region (PAR), Abnormal and Background Region (ABR). As before, the segmentation contains two stages: a training stage and a clinical segmentation stage. During the training stage, first, manually chosen representative images are segmented using hierarchical level set region detection. Then the results are used to train an SVM classifier. During the clinical segmentation stage, dental X-ray are first classified by the trained SVM, which provides initial contours for two coupled competitive level set functions. The competition of the two level set functions will give the final segmentation result. Based on the segmentation results, an analysis scheme is applied. The scheme first builds an uncertainty map, which is then used to automatically mark any areas of

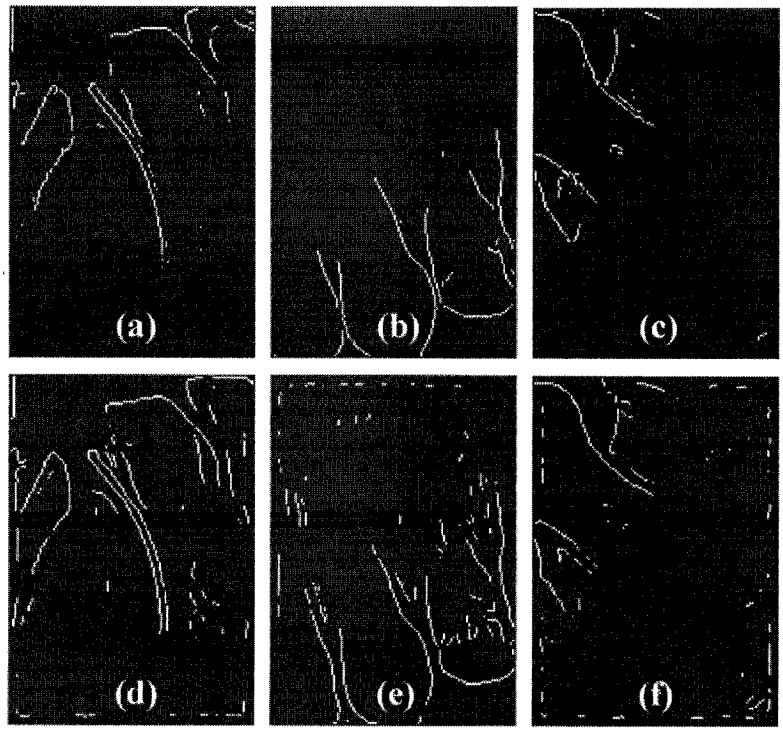

Figure 38: Edge detection of Fig. 34. (a-c) are edge detection by Sobel edge detection and (d-f) are edge detection by laplacian of gaussian (LOG).

bone loss. Subsequently, an average intensity profile based method is employed to isolate the teeth and detect possible root decay.

5.3.1 Competitive Variational Level Set Segmentation

As shown in the Chapter 3, variational level set can be modelled with a pathologically meaningful energy modelling, which will lead to a pathologically meaningful segmentation. In this implementation, we propose a new variational level set segmentation method driven by a new proposed pathological energy modelling. By the competition of two coupled level set functions, the segmentation segments the image into three pathological meaningful regions: Normal Region (NR), Potentially Abnormal Region (PAR), Abnormal and Background Region (ABR). The modelling explicitly incorporates problem regions as part of the modelling, such that the identification of these areas would be an automatic product of the segmentation.

Pathological Energy Modelling

With an evolving curve C, one level set function divides the image (u) into two parts: Normal Region Ω_{NR}("+" region) and Abnormal Region Ω_{AR}("-" region) as shown in the Fig. 39(b). The energy functional is given by

$$E(\Phi) = \beta_1 \int_{\Omega_{NR}} \frac{(u-c_{NR})^2}{\sigma_{NR}^2} dxdy + \beta_2 \int_{\Omega_{AR}} \frac{(u-c_{AR})^2}{\sigma_{AR}^2} dxdy, \tag{57}$$

where c_i is the mean grey value of the region Ω_i, σ_i is the variance and β_i is a constant.

However for medical diagnosis and early detection, the areas between the normal and abnormal regions are more important since these are the areas of potential problems, which are of particular interest for medical diagnosis and early detection of problems. Therefore we propose a competitive level set model with two level set functions to segment the image into three regions: normal region, abnormal region and potentially abnormal region. As shown in the Fig. 39(a), a dental X-ray image (u_0) can be divided into four region of interest: the Normal Region (Ω_{NR}), the Potentially Abnormal Region (Ω_{PAR}), the Abnormal Region (Ω_{AR}) and the Background Region (Ω_{BR}). Since Ω_{AR} and Ω_{BR} is not separable in terms of intensity values, so in the segmentation, we take Ω_{AR} and Ω_{BR} to be a single region: the Abnormal and Background Region (Ω_{ABR}). The energy functional for the two coupled level set functions (Φ_1 and Φ_2) can be modeled as:

$$\begin{aligned} E(\Phi_1, \Phi_2) = \lambda_1 \int_{\Omega_{NR}} \frac{(u-c_{NR})^2}{\sigma_{NR}^2} dxdy + \lambda_3 \int_{\Omega_{ABR}} \frac{(u-c_{ABR})^2}{\sigma_{ABR}^2} dxdy, \\ + \lambda_2 \int_{\Omega_{PAR}} Min\left(\frac{(u-c_{PAR_1})^2}{\sigma_{PAR_1}^2}, \frac{(u-c_{PAR_2})^2}{\sigma_{PAR_2}^2} \right) dxdy \end{aligned} \tag{58}$$

where the function $Min(x, y)$ returns the smaller value of x and y and λ_i is a constant. The modelling is in the same spirit as multiphase modelling in [79].

As shown in the Fig. 39(c) using competitive coupled level set functions, if both level set functions classify an area as a normal region, we take it as a normal region Ω_{NR}; if both level set functions classify a region as an abnormal and background region, we take it as an abnormal and background region Ω_{ABR}; however if only one of the level set functions segments a region as a normal region, the region will be taken as a potentially abnormal region Ω_{PAR}. Using the proposed method,

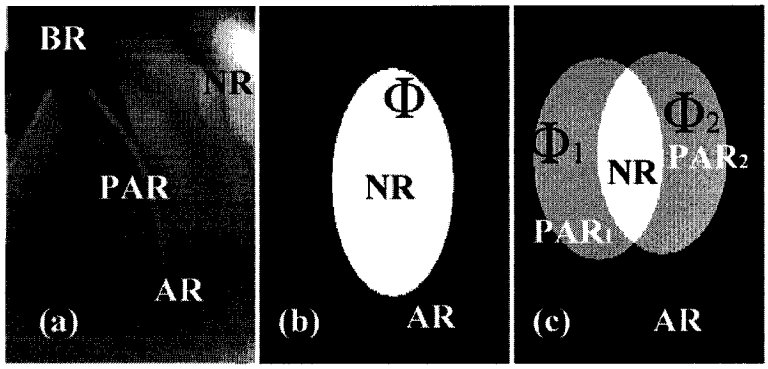

Figure 39: Region modelling. (a) The dental X-ray image can be divided into four regions: Ω_{NR}, Ω_{PAR}, Ω_{AR}, and Ω_{BR}. (b) With one curve C, one level set function segments the image into Ω_{NR} and Ω_{AR}. (c) Two competitive coupled level set functions segment the image into three regions: Ω_{NR}, Ω_{PAR} and Ω_{ABR}.

segmentation can be naturally achieved by the competition of the two level set functions.

Although it is possible to use three coupled level set functions to segment the image into three regions as described in [40, 39, 42], the two coupled level set method is able to achieve faster segmentation and a more accurate boundary as discussed in [79].

To achieve a fast and robust segmentation, a hybrid coupled level sets functional that combines minimal variance (Eq. 58), the optimal edge integrator [34] and the geodesic active contour model [7] is used:

$$E = E(\Phi_1, \Phi_2) - \gamma_1 E_{LAP} + \gamma_2 E_{GAC}, \tag{59}$$

where γ_i are constants.

Competitive Level Set Functions

The level set functions Φ_i derived from the functional in the Eq. 59 are shown below in Eqs. 60 and 61.

$$\begin{aligned}\frac{\partial \Phi_1}{\partial t} = \; & \delta_\varepsilon(\Phi_1)\Big[\gamma_2 div(g\tfrac{\nabla\Phi_1}{|\nabla\Phi_1|}) - \tfrac{(u-c_{NR})^2}{\sigma_{NR}^2}H(\Phi_2) - \tfrac{(u-c_{PAR})^2}{\sigma_{PAR}^2}(1-2H(\Phi_2)) \\ & + \tfrac{(u-c_{ABR})^2}{\sigma_{ABR}^2}(1-H(\Phi_2)) - \gamma_1 U_{\xi\xi}\Big],\end{aligned} \tag{60}$$

$$\frac{\partial \Phi_2}{\partial t} = \delta_\varepsilon(\Phi_2)\left[\gamma_2 div(g\frac{\nabla\Phi_2}{|\nabla\Phi_2|}) - \frac{(u-c_{NR})^2}{\sigma_{NR}^2}H(\Phi_1) + \frac{2(u-c_{PAR})^2}{\sigma_{PAR}^2}H(\Phi_1) + \frac{(u-c_{ABR})^2}{\sigma_{ABR}^2}(1-H(\Phi_1)) - \gamma_1 u_{\xi\xi}\right]. \quad (61)$$

Here,

$u_{\xi\xi} = \Delta u - K_u|\nabla u|$.

Although we only apply the proposed level set method to the dental X-ray, the method can be extended to be a general segmentation method. Three regions medical image segmentation plays an essential role in the medical image processing since most X-ray and some types of CT images naturally contain up to three region of interest.

5.3.2 Segmentation

To apply the level set method in the dental clinical setting, we adapt the clinical segmentation framework described in the Chapter 3 for general clinical settings. The framework uses an SVM to provide a good initial contour for the level set method, which greatly speeds up convergence of the coupled level set functions. Following the same principle, we use an SVM to provide initial contours for two coupled level set functions. The purpose is not only to speed up the segmentation convergence, but also to provide a competitive initial condition for level set functions. The segmentation phase has two stages: a training stage and a clinical segmentation stage.

Segmentation Phase

During the training stage, manually chosen representative images are segmented by hierarchical level set region detection (see § 3.2.2 for detail) using the Chan and Vese level set method [10]. In the hierarchical level set region detection, first a level set function is used to separate Ω_{ABR} from the rest of the image (Ω_{AR} and Ω_{BR}). Then another level set function is used to separate Ω_{AR} and Ω_{BR}. Then these results are used to train an SVM classifier.

During the clinical segmentation stage, a dental X-ray image is first classified by the trained SVM. The classifier is able to give a rough classification of the three

regions (Ω_{ABR}, Ω_{NR} and Ω_{PAR}), which may not be accurate. But it provides good initial contours for coupled level set functions as described in [36, 37] and § 3.2.2. The final segmentation will be achieved by evolution of these two level set curves under the functional described in the Eq. 59 and level set functions described in Eqs. 60 and 61. The competitive initial conditions are set as following: for Φ_1, we set classified Ω_{NR} as the "+" region and rest of the image as the "- " region; for Φ_2, we set classified Ω_{NR} and Ω_{PAR} region as the "+" region and rest of the image as the "-" region.

Eigenpatch Feature Extraction

In the training stage, after segmentation, the results are used to train a SVM. The procedure of the feature extraction is illustrated in the Fig. 40. To speed up classification we use the PCA method based on eigenpatch discussed in § 4.2.3 as shown in the Fig. 40.

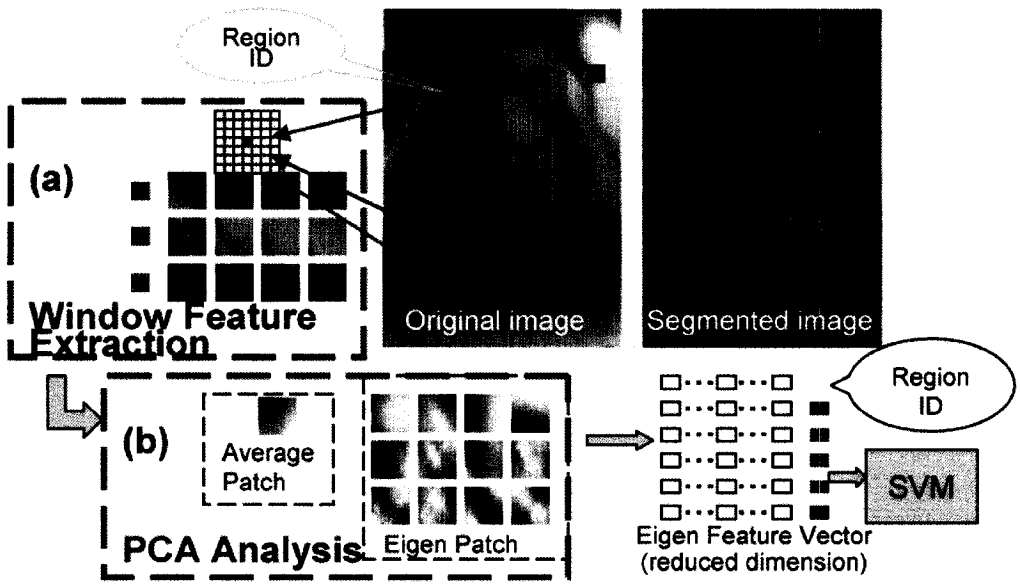

Figure 40: Feature extraction diagram.

5.3.3 Analysis Phase

The analysis phase contains three steps: uncertainty map building, bone loss detection and root decay detection. The first two steps are fully automatic. The only

manual input for the last step is the image orientation. This information is not difficult to obtain in the dental clinical setting.

Uncertainty Map

As shown in the § 3.3.4, intensity deviation has a good diagnosis value together with segmentation result. Here, following the same principle in the § 3.3.4, an uncertainty map is built based on the following uncertainty measurement:

$$\psi = \frac{(u - c_{NR})\tau_1 + (u - c_{PAR})(\tau_2 - 2\tau_1) + (u - c_{ABR})(1 - H(\phi_1))(1 - H(\phi_2))}{\sigma_{NR}\tau_1 + \sigma_{PAR}(\tau_2 - 2\tau_1) + \sigma_{ABR}(1 - H(\phi_1))(1 - H(\phi_2))}$$

where $\tau_1 = H(\phi_1)H(\phi_2)$ and $\tau_2 = H(\phi_1) + H(\phi_2)$.

The uncertainty map provides a digitalized intensity deviation for further analysis. As shown in the following, those high uncertainty areas usually have diagnostic value.

Bone Loss Detection

Areas of bone loss will generally occur in those regions of high uncertainty. Therefore, we mark these areas with different levels of emphasis according to the uncertainty measurement and the type of region segmented.

Color emphasis scheme: Although the uncertainty map is an objective and digitalized uncertainty measure, it fails to provide direct visual cues. In this chapter, we propose an approach to combine the uncertainty map with the color channels to give efficient and direct visual aids to the dentist. To achieve the visual assistance, the RGB channels of the image are used to couple the intensity values of the image with the degree of uncertainty at each pixel. For all regions, the G channel is used to represent the intensity value of each pixel of the original dental X-ray image. The uncertainty values are nonlinearly scaled to the range 0 to 255. To differentiate between the three type of regions, for Ω_{ABR}, the R channel is set to the uncertainty value while the B channel is set to 0; for Ω_{PAR}, both the R and B channels are set to 255 to emphasize this region; and for Ω_{NR}, both the R and B channels are set to the uncertainty value.

Root Decay Detection

Root decay detection consists of three steps: tooth isolation, root decay location and seriousness level evaluation. This is a semi-automatic process in which the orientation of the teeth is supplied manually.

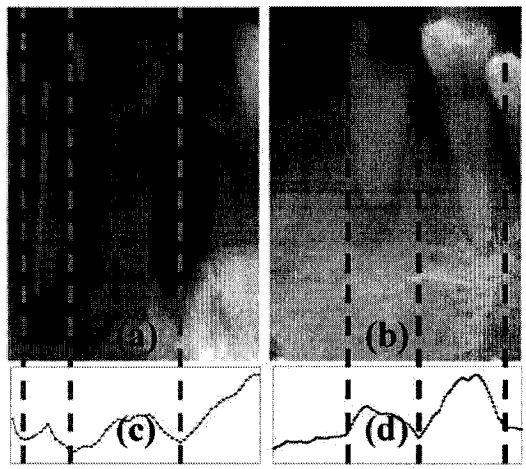

Figure 41: Teeth isolation. (a) Original image 1. (b) Original image 2. (c) Integrated intensity profile of (a). (d) Integrated intensity profile of (b). The scales of the profiles in (c) and (d) are normalized to facilitate comparison.

Teeth isolation: As suggested by Jain *et al.* [28], individual teeth can be isolated by the integrated intensity value as shown in the Fig. 41. The integrated intensity values sum the intensities of pixels along the vertical direction. Since the teeth usually yield higher intensity values than the jaws and other tissues, the gap of teeth will have a very low value on the integrated intensity value profile as shown in the Fig. 41 (c) and (d). However, unlike a dental forensic X-ray analysis, which can be assumed to have certain orientations, the clinical dental X-ray used to detect root decay, etc., could have any orientation. As shown in the Fig. 42(a) and (c), if the orientation varies, this profile method will not be able to obtain the correct isolation. Therefore as additional information, we assume that the orientation is given. Then we rotate the image according to the given orientation so that the teeth are aligned in a consistent direction. After the rotation, instead of using an integrated intensity value, we use the average of the intensity value (the integrated intensity value divided by the number of pixels) as shown in the Fig. 42(b) and (d).

Root decay location and seriousness level evaluation: The areas of decay are considered to be root decay if they are found at the root of teeth with the

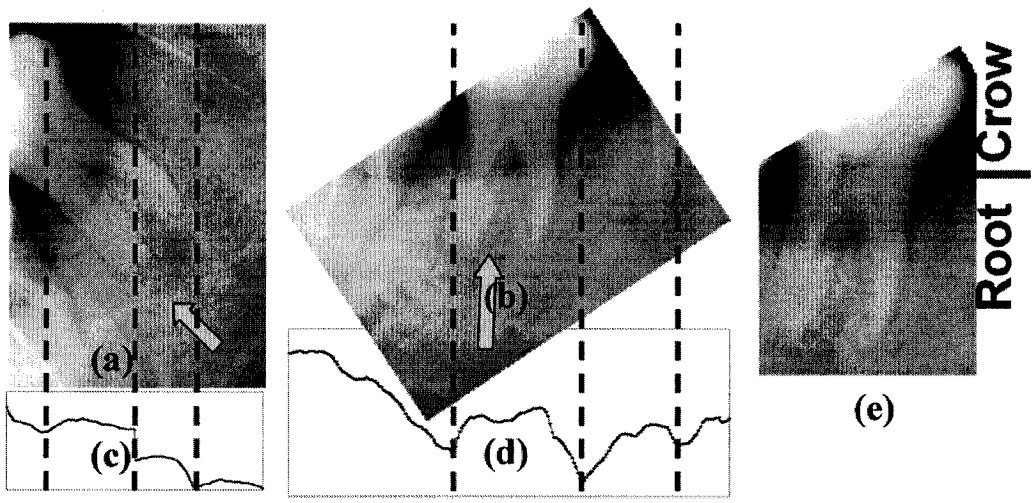

Figure 42: Teeth isolation. (a) Original image. (b) Rotated image. (c) Integrated intensity profile of (a). (d) Average intensity profile of (b). (e) Two parts of a tooth: crown and root.

following seriousness levels, in order of most serious to least serious: 1. Serious Level (SL): if the Ω_{ABR} is found at the root of the tooth; 2. Warning Level (WL) : if the Ω_{PAR} of any uncertainty is found at the root of the tooth; 3. Attention Level (AL): if a high uncertainty area of Ω_{NR} is found at the root of the tooth. In this implementation, the bifurcation decay (as shown in the Fig. 42 (e)), the decay on the bifurcation of the teeth, is taken as one type of areas of root decay.

To improve the robustness and reduce the misidentification, the following two schemes are applied: 1. the seriousness level of the root decay is decided by the most serious level. 2. the area of decay is assumed to be a "round" shaped region. So the "nail like" shaped regions will be ignored since they are usually either nerves or noise..

5.4 Experimental Results

Altogether sixty dental X-ray with different level of bone loss and root decay were used to test the proposed framework. The root decay and bone loss area detected by the program are validated by two dentists. The promising results were demonstrated and analyzed in segmentation and analysis sections below separately.

5.4.1 Segmentation

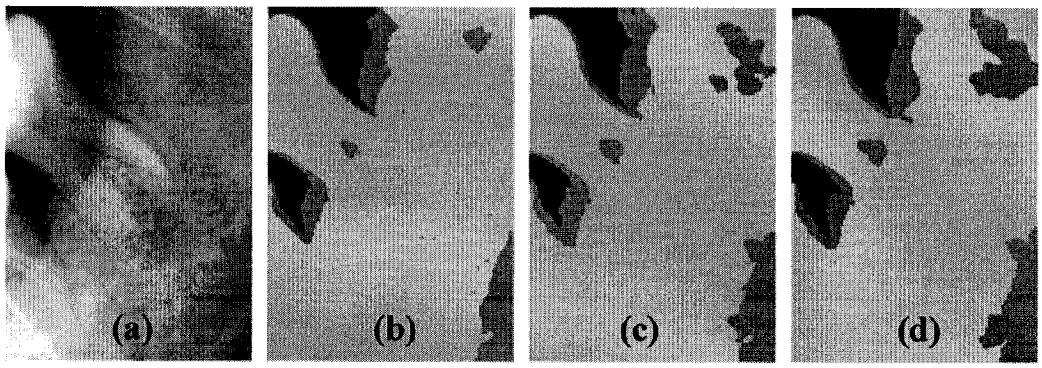

Figure 43: Segmentation results. (a) Original image. (b) Iteration 0 provided by SVM. (c) Iteration 40. (d) Iteration 60.

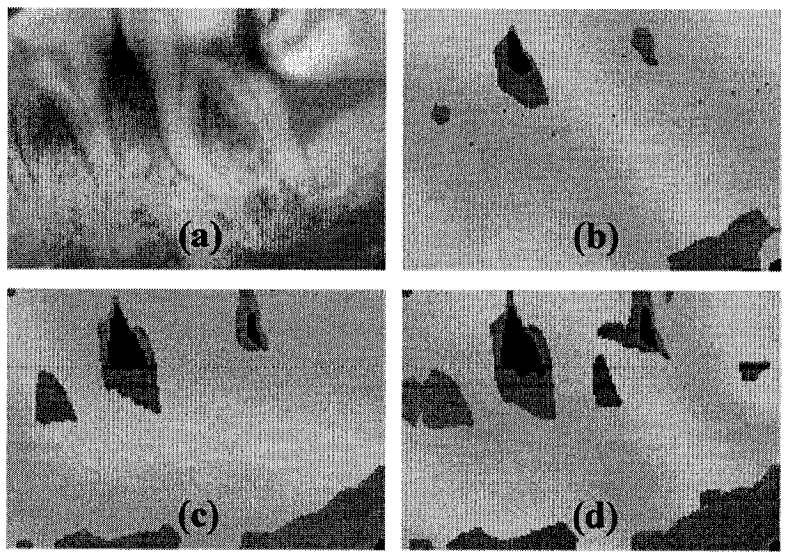

Figure 44: Segmentation results. (a) Original image. (b) Iteration 0 provided by SVM. (c) Iteration 40. (d) Iteration 60.

First, images were used to test the proposed segmentation method. The results presented in Figs. 43 to 46, show that competitive level set segmentation is able to give pathologically meaningful segmentation. Most of the bone loss and decay areas are segmented as potentially abnormal region; the serious decay areas are included in the abnormal and background region; and the early decay areas are included in the normal region. The pathologically meaningful segmentation is achieved by explicitly incorporating regions of problems as part of the modelling, such that those areas

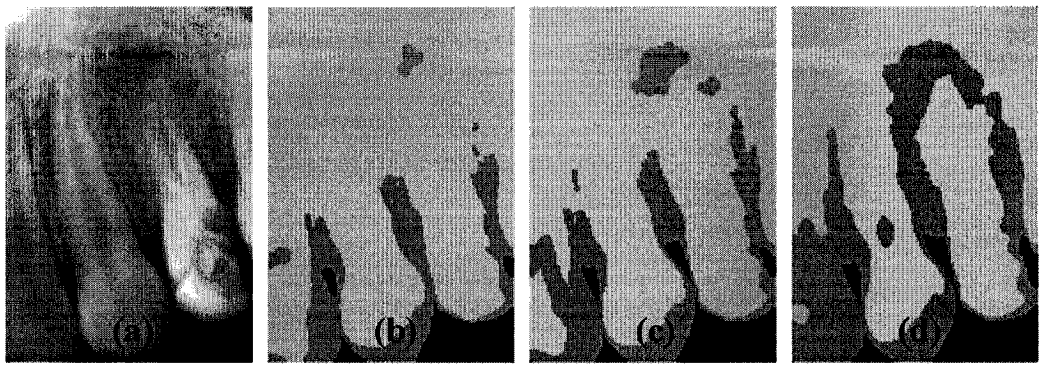

Figure 45: Segmentation results. (a) Original image. (b) Initial condition provided by SVM. (c) Iteration 20. (d) Iteration 60.

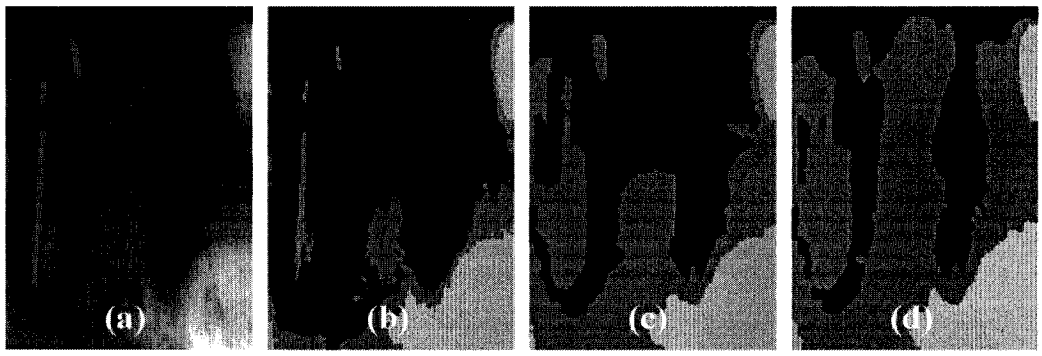

Figure 46: Segmentation results. (a) Original image. (b) Iteration 0 provided by SVM. (c) Iteration 40. (d) Iteration 80.

would be automatically segmented by the competition of the level set functions. Moreover, as shown in those figures, although the SVM only gives an approximate segmentation, it is able to provide good initial contours for two level set functions, which not only accelerates the segmentation, but also provides competitive initial conditions for level set functions. Indeed, the competitive level set segmentation is robust to the placement of the initial contours so that even when the initial contours do not closely correspond to the final segmentation, the level set functions can still achieve an accurate segmentation as shown in the Fig. 46 although with more iterations.

5.4.2 Analysis

The pathological segmentation provides a sound basis for analysis. Since the pathologically modelled competitive level set segmentation explicitly incorporates regions

of problems as part of the modelling, the identification of decay areas is an automatic product of the segmentation.

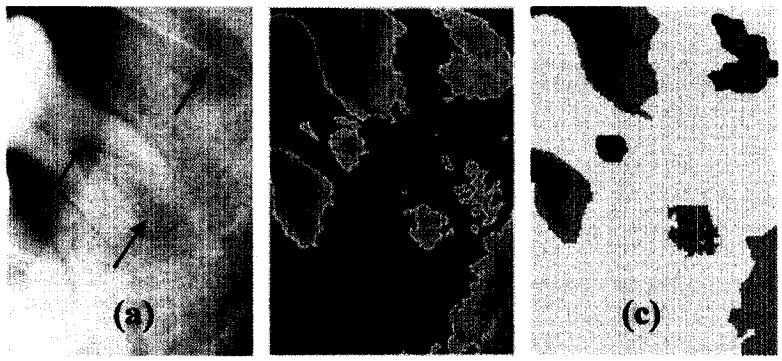

Figure 47: Segmentation results. (a) Original image. (b) Bone loss area marked with color channel method. (c) Root decay detected.

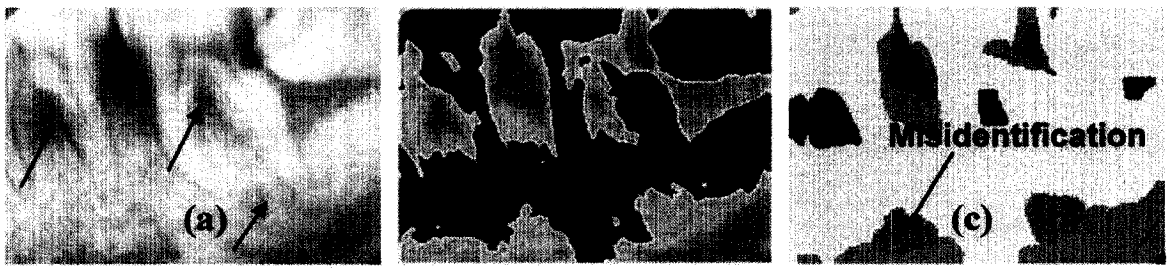

Figure 48: Segmentation results. (a) Original image. (b) Bone loss area marked with color channel method. (c) Root decay detected.

Based on the uncertainty map and segmentation results, the color emphasis scheme is able to indicate all the areas of bone loss and decay in the image, as shown in Figs. 47(b) and 48(b), in which the bone loss areas are emphasized by the color scheme. Since the soft tissue has the same intensity distribution, they are also marked as bone loss area. The scheme provides direct visual cues, which will greatly reduce the possibility that some of these areas, e.g. areas indicated by arrows in the Fig. 47(b) for example, might be overlooked. Although the area is segmented as a normal region in the segmentation phase, the color channel scheme is able to highlight those areas for the dentist's attention.

Figs. 47 to 50 show the results of teeth root decay detection. In the example shown in the Fig. 47, after being given the orientation of the image, the color analysis scheme successfully locates the areas of root decay (see Fig. 47(c)). In this example,

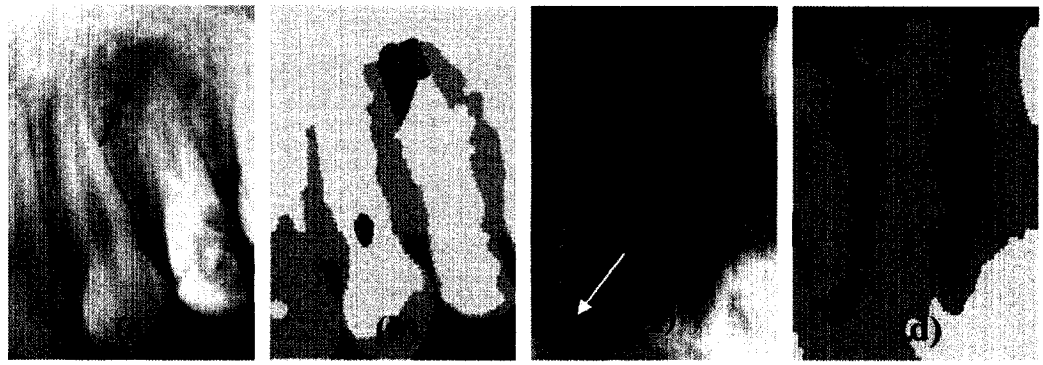

Figure 49: Root decay detection results. (a,c) Original image with root decay area pointed by dentist. (b,d) Root decay detected.

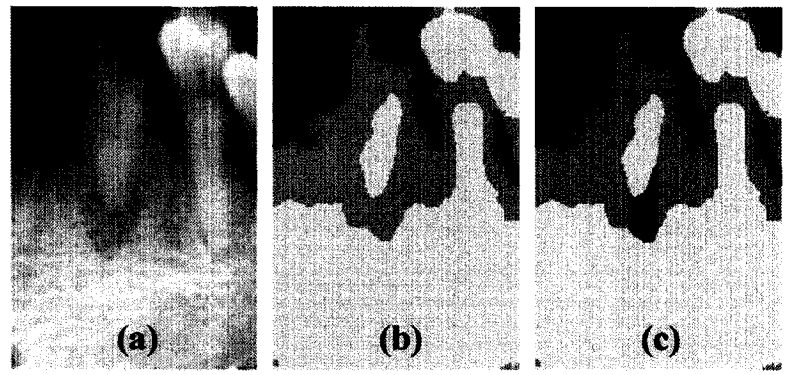

Figure 50: Root decay detection results. (a) Original image. (b) Segmentation Results. (c) Root decay detected.

the system automatically locates three areas of root decay. Two of them are at the warning level (pink area) and one is at the attention level (orange area). In the example shown in the Fig. 48, five areas of root decay are detected although one of them is a false positive. Fig. 49 shows other two examples of locating a warning level area of root decay (pink area in the Fig. 49(b)) and a serious level root decays (red area in the Fig. 49(d)). Fig. 50 shows an example of locating a warning level area of root decay (pink area in the figure).

Fig. 51 shows two of the visualized uncertainty maps. The uncertainty map is able to give a general idea of the problem areas. And more importantly, it provides a digitized uncertainty measurement for further analysis.

The experimental results validated by dentists show that the proposed framework is able to help to find all the areas of bone loss. For the root decay detection, the proposed framework is able to semi-automatically detect all of root decays. But due

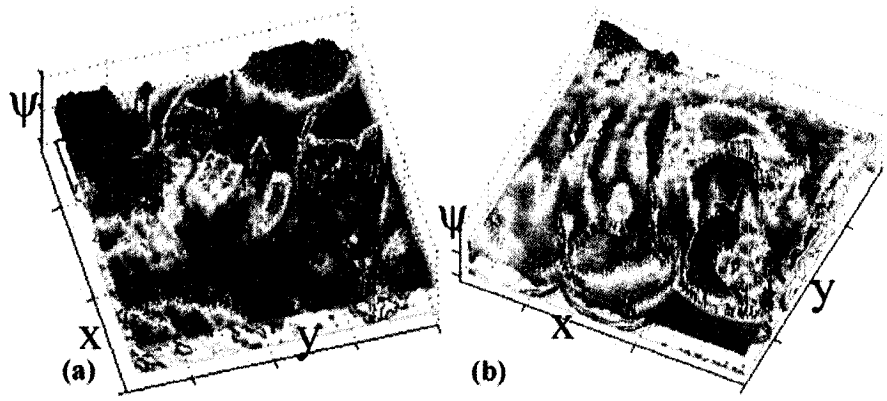

Figure 51: Uncertainty maps of (a) Fig. 43 and (b) Fig. 45

to complexity of the dental X-ray, there are still 11 false positive of root decay out of 162 areas of root decay detected. One of these false positive is indicated by an arrow in the Fig. 48(c).

5.5 Summary

In this chapter, a semi-automatic dental decay detection framework has been proposed to detect the areas of bone loss and root decay from dental X-ray. In this framework, first, a new proposed competitive coupled level set method is used to segment the image into three pathologically meaningful regions using two coupled level set functions. Tailored for the dental clinical setting, a two-stage clinical setting applicable segmentation method is used. The method uses a trained SVM classifier to provide an initial contour for two coupled level sets. Then, based on the segmentation results, an analysis scheme is applied. Firstly, the scheme builds an uncertainty map from which those areas with bone loss will be automatically detected. Secondly, the scheme employs a method based on the average intensity profile to isolate the teeth and detect root decay. Experimental results show that our proposed framework is able to automatically detect the areas of bone loss and, when given the orientation of the teeth, it is able to automatically detect the root decay with a seriousness level marked for further dental diagnosis. The framework has the potential to be used in a dental clinical setting since the classifiers can be trained in advance and the orientation of the X-ray image can be given or predetermined by the dentist.

Chapter 6

Volumetric Medical Image Reconstruction

"The grand aim of all science is to cover the greatest number of empirical facts by logical deduction from the smallest number of hypotheses and axioms."

- Albert Einstein (1879-1955)

6.1 Introduction

The reconstruction and visualization of volumetric medical data has been an active area of research in recent decades. It plays a critical role in the medical image analysis and visualization. The problem of 3D reconstruction arises in the medical imaging where human organs are scanned through an image modality (e.g. CT , MRI scans). Such reconstructions of human organs are widely used for computer aided diagnosis, planning and simulation [52, 84], prosthesis milling, radiation therapy planning and volumetric measurements. Due to the increasing use of the 3D and 4D medical data, the reconstruction becomes increasingly important.

There have been a great number of approaches proposed, which may be roughly classified into two groups: surface reconstruction and volume reconstruction. Most of the current approaches cope only with surface modelling. In the surface reconstruction approach, typically the main goal is to reconstruct a triangulated surface that bounds an object. This group of methods is usually very fast. However only the surface information is used. The internal part is discarded. In this category,

recent researchers are use GDM to detect the surface. Most of these works are application oriented as shown in [6, 73]. One the other hand, volume reconstruction is usually based on voxel-technique. The surface can be fit on the set of parallelepipeds based on these techniques, for example the marching cube technique [46], and the object is rendered with conventional rendering algorithms such as ray casting and ZSweep [25]. The volume reconstruction is able to keep all the information. However the main disadvantage is it relies on the large volume of data to be manipulated. This is a fatal problem for many real time applications such as remote data access and web based visualization, which becomes more and more popular now.

To overcome the above problems, we explore the advantage of using tetrahedral meshes to combine surface reconstruction and volumetric reconstruction. We propose an approach to reconstruct non-grid models from grid based volumetric data sets. By this method, the regular grid based volumetric medical image is first segmented by a coupled level set method driven by a pathologically modelled functional. Then the volumetric medical image is transformed from regular grid data to a tetrahedral mesh. To reduce the redundancy and noise in the data set to reach the goal of effective storing, transferring and rendering the data efficiently, a hybrid sculpting scheme is proposed to sculpt the tetrahedral mesh obtained while still preserving the important features necessary for diagnosis. With customizable criteria, the hybrid sculpting scheme is able to provide multiple levels of detail, thus enables the efficient reconstruction and visualization of the data at different levels of detail. The method has the potential to be used in a clinical setting where a radiologist or clinician can quickly inspect a volumetric image even when the data is remotely obtained.

6.2 Proposed Framework

6.2.1 Pathological Segmentation

In this work, the pathological level set method described in the § 4.2.1 is used to segment the volume first. With the assistance of radiologist, the energy functional is modelled according to the pathological meaning of different regions in a typical medical image of the type being considered. Without losing generality, we are going to take chest CT scans as an example to describe the modelling. For this

implementation, a chest CT image is divided into four region of interest as shown in the Fig. 22 in the § 4.2.1: the Background Region (Ω_{BR}), the Skeletal Structure Region (Ω_{SR}), the Fatty Tissue Region (Ω_{FR}) and the Muscle and Visceral Tissue Region (Ω_{MR}). The detail of the modelling can be found in the § 4.2.1.

Segmentation plays an important role in the reconstruction since it changes the unstructured data into structured data. It creates a basis for the reconstruction. Compared to other segmentation methods, level set is able to achieve accurate and automatic segmentation. More importantly it is very robust to noise, which is essential for medical image processing. Although it is a originally slow processing, several efforts [36, 9] have been proposed to improve the speed of level set when applied in medical and clinical applications.

6.2.2 Tetrahedral Partition

The original grid data is transformed into tetrahedral mesh by simply splitting each voxel/cubic diagonally into five tetrahedra as shown in the Fig. 52. The tetrahedral mesh provides great flexibility with reconstruction due to the following two reasons:

1. Operations of hybrid sculpting can be easily performed on its basic primitive, tetrahedron. It is convenient to assign attributes and functions to the vertices and tetrahedron. Computational steps such as interpolation, integration, and differentiation are fast and can be done in similar forms.
2. With tetrahedral mesh and segmentation results, we can easily combine volume visualization with surface visualization. Moreover, the triangles that generated by tetrahedra may be rendered with hardware acceleration.

6.2.3 Hybrid Sculpting

Usually a medical image contains a large amount of redundancy, which has been inherited by the tetrahedral mesh after partition. To achieve efficiency in storing, transferring and rendering, an efficient tetrahedral mesh sculpting scheme is needed to reduce the complexity of original dataset by collapsing some of the tetrahedra while preserving meaningful features. Based on region information naturally obtained by segmentation, inspired by [6, 30, 58, 85], some of the basic graphics techniques such as tetrahedra collapse, flip check and error predictions are modified

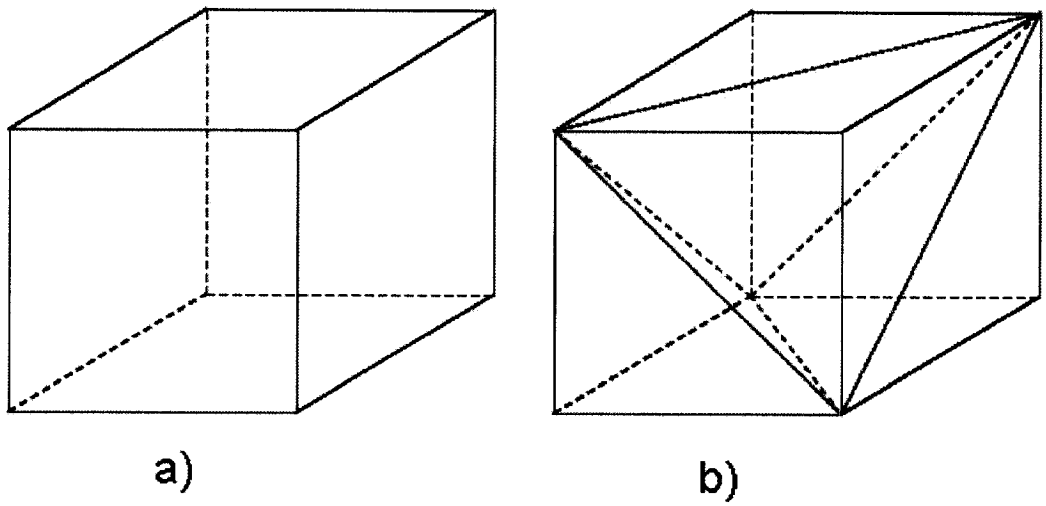

Figure 52: Tetrahedral partition. (a) One cube. (b) Partition of five tetrahedra.

and adopted from [30], we propose a hybrid sculpting scheme, which is consisted of two sculpting schemes: internal sculpting and surface sculpting.

Internal Sculpting

By internal sculpting, each region is internally sculpted individually. To meet different requirements and obtain an optimized sculpting, a customable hybrid regional and local error prediction based internal sculpting scheme is used to reach different levels of sculpting. This is done by a weighted sum of regional error prediction (ε_r) and local error prediction (ε_g, ε_n, ε_v and ε_s) to optimally choose the next cell to be collapsed as shown:

$$\Delta\varepsilon_I = \omega_r\varepsilon_r + \omega_g\varepsilon_g + \omega_n\varepsilon_n + \omega_s\varepsilon_s + \omega_v\varepsilon_v, \tag{62}$$

where ω_i are weights and ε_i are error predication functions as following:

$$
\begin{aligned}
\textit{Variance Error Prediction:} \quad & \varepsilon_r = \frac{1}{4}\sum_{i=0}^{3}(s_i - \mu_k)/{\sigma_k}^2, \\
\textit{Gradient Error Prediction:} \quad & \varepsilon_g = \frac{1}{4}\sum_{i=0}^{3}(s_i - s'_n)^2, \\
\textit{Volume Error Prediction:} \quad & \varepsilon_n = volume(\tau)/\sum volume(\tau_i), \\
\textit{Volume Aspect Prediction:} \quad & \varepsilon_v = |a \cdot (b \times c)|/3!, \\
\textit{Shape Error Prediction:} \quad & \varepsilon_s = \frac{1}{4}\sum_{i=0}^{3}|v_i - \hat{v}_n|,
\end{aligned}
$$

where s_i are the attribute values of the original vertices v_i of the cell τ ready for collapse; μ_k and σ_k are mean value and variance of the region the cell belongs to; s'_n is the attribute value of new vertex after collapse; $\hat{v}_n$ is the new vertex generated after collapse; a, b and c represent the three edges of the cell τ, which share one common vertex; and τ_i are the neighboring cells.

The internal sculpting removes internal redundancy while preserving internal pathological features via the hybrid error prediction function. This is achieved by choosing the cells with smallest $\Delta\varepsilon_I$ values to collapse in each iteration of the sculpting. The internal sculpting is only performed in each segmented region individually and does not touch the boundaries of either the regions or the overall volume..

Greedy Internal Sculpting Scheme The sculpting is an iteration based process. Each iteration gives one level of sculpting ratio, which is defined as:

$$
sculpting\ ratio(\gamma) = \frac{\text{number of tetrahedra removed}}{\text{number of tetrahedra in the original image}}. \tag{63}
$$

To achieve fast processing, we choose the greedy strategy to implement each iteration as listed below:

1. For all the non-surface cells, the cells are sorted with respect to $\Delta\varepsilon_I$ and stored in a queue, if the $\Delta\varepsilon_I$ is smaller than a specific threshold.
2. For all the cells in the queue, a collapse operation is performed after checking that the operation will not cause the flipping problem (i.e., its interior becomes its exterior after a collapse). For more detail about the tetrahedral collapse, we refer the reader to [31, 58, 85].

Surface Sculpting

Based on the segmentation, during the tetrahedral partition, tetrahedral cells on the surface are marked. During the internal sculpting, these surface cells are left untouched. However, for many applications, the surface of the overall volume plays a less important role in the visualization of the volume. Therefore we provide such a surface sculpting scheme subject to customization based on need.

To obtain an optimized surface sculpting, a weighted sum of gradient error prediction (ε_g), shape error prediction (ε_s) and Hausdorff error prediction (ε_h) is used to optimally choose the cell along the surface to be collapsed as shown in the Eq. 64. Based on the Hausdorff distance function ($h(\cdot)$), which is the maximin function of a set to the other set [59], Hausdorff error prediction is asymmetric and oriented as shown in [74]. This characteristic helps to preserve more meaningful features along the surface.

$$\Delta\varepsilon_S = \omega_g\varepsilon_g + \omega_s\varepsilon_s + \omega_h\varepsilon_h \tag{64}$$

$$\textit{Hausdorff Error Prediction:} \quad \varepsilon_h = \max(h(P,\hat{P}), h(\hat{P},P)), \tag{65}$$

$$\textit{Hausdorff Distance Function:} \quad h(P,\hat{P}) = \max_{p_i\in P}(\min_{p_j\in\hat{P}}(\textit{distance}(p_i,p_j))),$$

where P is localized surface mesh and $\hat{P}$ is sculpted surface mesh, and functions *max* and *min* return the larger and smaller value, respectively.

Greedy Surface Sculpting Scheme Similar to greedy internal sculpting, each iteration of greedy surface sculpting has the following steps:

For all the cells on the surface,

1. if the cell has one single vertex on the surface, the cell will be collapsed to that vertex;
2. if the cell has two vertices on the surface, the cell will be collapsed to the middle of these two vertexes when among all the cells share the same two vertices, the cell has the smallest $\Delta\varepsilon_S$, which is smaller than the specified threshold;
3. if the cell has three or more vertices on the surface, the cell will not be collapsed.

Combined Sculpting

To obtain large sculpting rate, internal sculpting and surface sculpting can be combined together. For combined sculpting, in each iteration, the mesh is sculpted by surface sculpting followed by internal sculpting.

6.3 Experimental Results

We have implemented our algorithm on a Windows Platform with a 2.39GHz Intel Pentium 4 CPU and NVIDIA Quadro4900 XGL adapter with 128 Megabit RAM. We use ZSweep as our irregular mesh rendering technique to obtain the final images.

In the following, our proposed method is tested on chest CT scans. Results show that the proposed framework is able to successfully reconstruct the organs from the original medical volume. Also the proposed hybrid sculpting is able to remove redundancy while preserving important features with multiple levels of detail. Although only tested using chest CT scan, our method can be used for a general medical volume with its associated pathological modelling.

The Fig. 53 shows the level set segmentation using pathologically modelled variational level set method. Each level set function is first initialized as a sphere as shown in the Fig. 53(a). Driven by the pathological energy functional, the evolving of the level set curves converges to final segmentation, which segment the volume into four pathologically meaningful regions as shown in the Fig. 53(d). The segmentation creates a solid basis for the whole reconstruction. It helps to find the structure and boundaries of each pathological region, which is ideal as the starting point for feature preserving hybrid sculpting.

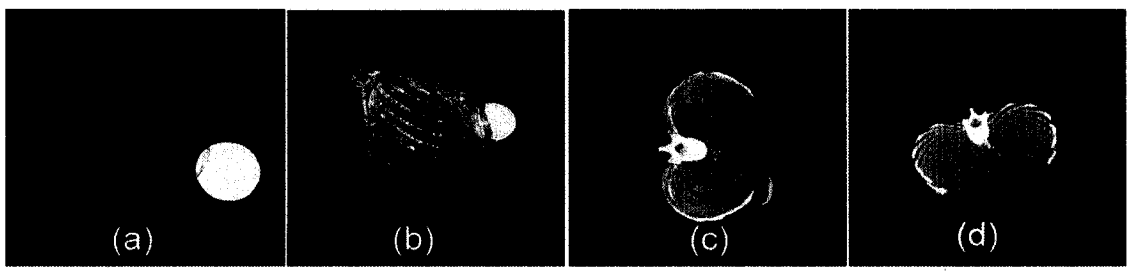

Figure 53: Volumetric segmentation results with four coupled level sets. (a) Iteration 0. (b) Iteration 30. (c) Iteration 80. (d) Iteration 120.

To test the efficiency of the internal sculpting, we use ZSweep to visualize the

tetrahedral mesh before and after internal sculpting as shown in the Fig. 54. Comparison of Fig. 54 (a) and (c) shows even when 64% of tetrahedra are collapsed by internal sculpting, there is still no noticeable visual change in its visualization. This indicates the efficiency of internal sculpting scheme at preserving the important features while removing large amount of redundancy in the image.

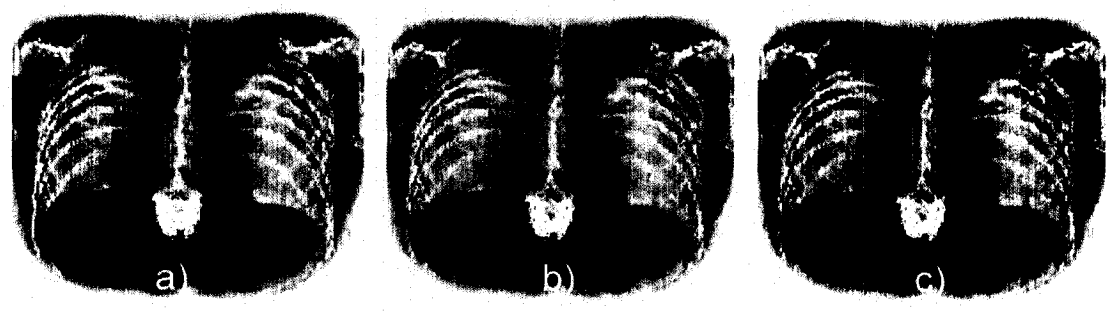

Figure 54: Volume rendering for internal sculpting using ZSweep. (a) Original image. (b) $\gamma = 48\%$. (c) $\gamma = 64\%$.

Bone structure is used to demonstrate the surface sculpting and combined sculpting as shown in the Figs. 55 to 58. Fig. 55 demonstrates the reconstructed bone from the original volume. Fig. 56 demonstrates the results of only surface sculpting. The surface is extracted from the surface tetrahedra in the mesh. Since the surface usually contains very important information, surface sculpting alone can only collapse 17% of tetrahedra as shown in the Fig. 56. Using combined sculpting, a large sculpting rate can be achieved as shown in Figs. 57 and 58. Even when more than 90% of the tetrahedra have been collapsed, the main structure of the volume is still kept, which indicates the efficiency of the proposed sculpting schemes.

Figure 55: Two views of bone surface rendered from tetrahedral mesh ($\gamma = 0\%$).

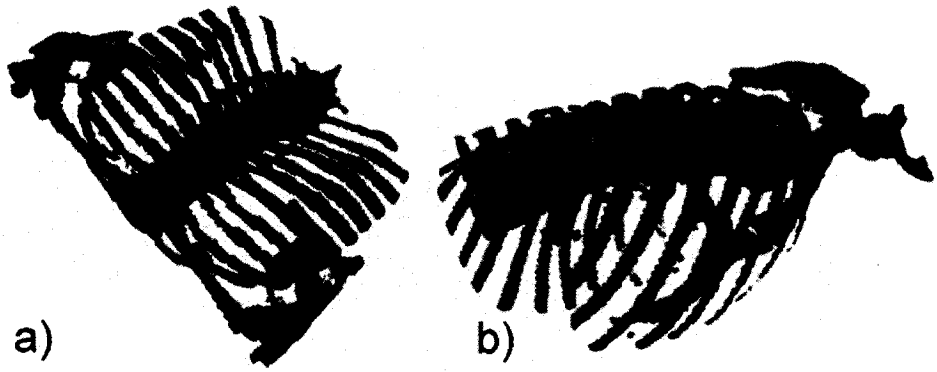

Figure 56: Two views of surface sculpting results ($\gamma = 17\%$).

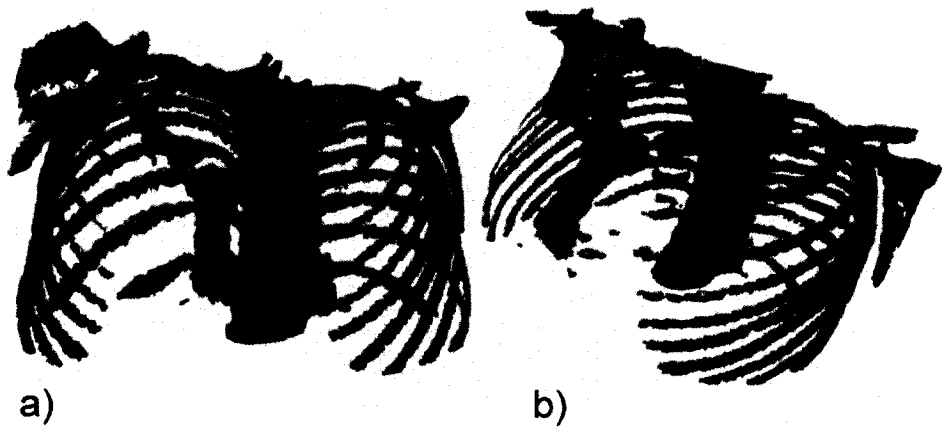

Figure 57: Two views of sculpting results using combined internal and surface sculpting ($\gamma = 63\%$).

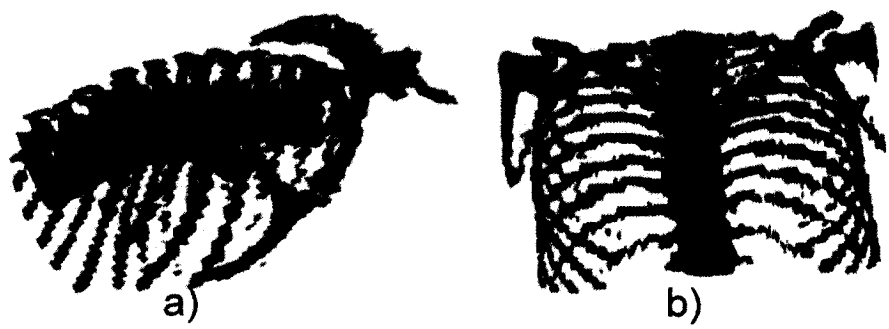

Figure 58: Two views of sculpting results using combined internal and surface sculpting ($\gamma = 91\%$).

6.4 Summary

In this chapter, a volumetric medical image reconstruction method using tetrahedral meshes and level set has been whereby non-grid models are reconstructed from grid based volume. In addition, the approach is able to provide customizable feature preserving levels of detail. By this method, the grid based volumetric medical image is first segmented by coupled level sets driven by a pathologically modelled energy functional. The segmentation divides the volume into pathologically meaningful regions. The volume is changed from regular grid data to a tetrahedral mesh by tetrahedra partition scheme, which divide one cube into five tetrahedra. To reduce the redundancy in the mesh, a hybrid sculpting scheme is proposed to reduce the amount of redundancy and noise while preserving the important features. The hybrid sculpting scheme consists of internal sculpting and surface sculpting, which is able to provide multiple levels of detail through each iteration of sculpting thus enabling efficient reconstruction and visualization of the data. Initial results confirm the efficiency of the proposed method and demonstrate high visual quality for rendered data even when a large sculpting rate is achieved. These results show that the proposed framework is able to maintain important features with less data volume and change the data from regular grids to tetrahedral mesh whose rasterization are supported by 3D graphics hardware. Moreover the results show that hybrid sculpting proposed provides efficient multiple levels of detail by removing redundancy while preserving important features. The framework has potential to be used in clinical setting where a radiologist or clinician can inspect the volumetric image with less data volume and faster hardware supported volumetric rendering even the data is remotely obtained.

Chapter 7

Conclusion and Future Work

"I never worry about the future. It comes soon enough."

– Albert Einstein (1879-1955)

7.1 Conclusion

This thesis reports on our efforts to overcome some of the current challenges existing in medical image analysis and visualization using geometric level set.

The theoretical contribution of the thesis lies in extension of geometric level set on domain of medical image analysis and visualization. To improve the performance of the geometric level set, the strength of geometric level set was combined with some recently developed techniques such as, support vector machine and principal component analysis for example, to limit the weakness and strengthen the strong points. Results have shown that by this, we are able achieve fast, robust and accurate segmentation methods. Two novel level set segmentation methods are proposed. The competitive level set, which segment triple region image using two coupled level set functions, and pathological level set, which incorporate pathological diagnosis information into level set segmentation, proposed in the thesis have potential to be used widely in medical image analysis and visualization since it provides a base for further processing.

The practical contribution of the thesis lies in two applications: dental X-ray CAD and chest CT volume reconstruction. Results from dental X-rays have shown that the dental X-ray CAD is able to automatically detect the bone loss and root decay based on the analysis of segmentation result. Results of volume reconstruction

on chest CT scan have shown that the proposed method is able to transfer grid based medical volume into non-grid volume. More importantly, it is able to remove the redundant while keeping important features.

7.2 Future Work

As is often the case in research, this thesis leaves more open questions than closed chapters.

In the future, we will keep working on the following:

1. research and development of a general automatic approach, which fuses segmentation and registration together. As two popular tools in the medical image analysis and visualization, automatic segmentation and registration are two very challenging and unsolved problems. This is a very active and challenging research topic in the field.
2. research and development of an efficient (real time if possible) volumetric medical image reconstruction and visualization system using cutting edge segmentation and registration method with application on virtual augmentation and simulation for diagnosis and surgery.

Bibliography

[1] History of medical diagnosis and diagnostic imaging. http://imaginis.com/faq/history.asp.

[2] Milestones in medical diagnosis and diagnostic imaging. http://imaginis.com/faq/milestones.asp.

[3] G. E. Andrews. *The Theory of Partitions.* Cambridge University Press, 1998.

[4] C. Baillard, C. Barillot, and P. Bouthemy. Robust adaptive segmentation of 3-D medical images with level sets. Technical Report PI-1369, IRISA, Rennes Cedex, France, 2000.

[5] C. Baillard, P. Hellier, and C. Barillot. Cooperation between level set techniques and dense 3D registration for the segmentation of brain structures. In *International Conference on Pattern Recognition*, 2000.

[6] P.-L. Bazin and D. L. Pham. Topology smoothing for segmentation and surface reconstruction. In *International Conference on Medical Image Computing and Computer-Assisted Intervention (MICCAI)*, pages 111–118, 2004.

[7] V. Caselles, R. Kimmel, and G. Sapiro. Geodesic active contours. *International Journal of Computer Vision*, 22:61–79, 1997.

[8] V. Caselles, R. Kimmel, G. Sapiro, and C. Sbert. Minimal surfaces based object segmentation. *IEEE Trans. on Pattern Analysis and Machine Intelligence*, 19(4):394–398, 1997.

[9] J. E. Cates, A. E. Lefohn, and R. T. Whitaker. GIST: an interactive, GPU-based level set segmentation tool for 3D medical images, medical image analysis. Technical report, September 2004.

[10] T. Chan and L. Vese. Active contour without edges. *IEEE Trans. on Image Processing*, 24:266–277, 2001.

[11] C.-C. Chang and C.-J. Lin. Training nu-support vector classifiers: theory and algorithms. *Neural Computation*, 13(9):2119–2147, 2001.

[12] L.W. Chang, H.W. Chen, and J.R. Ho. Reconstruction of 3D medical images: A nonlinear interpolation technique for reconstruction of 3D medical images. *Computer Vision, Graphics, and Image Processing*, 53:382–391, 1991.

[13] H. Chen and A. K. Jain. Tooth contour extraction for matching dental radiographs. In *International Conference on Pattern Recognition*, volume III, pages 522–525, Cambridge, UK, August 2004.

[14] D. L. Chopp. Computing minimal surfaces via level set curvature flow. *Journal of Computational Physics*, 106(1):77–91, 1993.

[15] I. Cohen, Laurent D. Cohen, and N.Ayache. Using deformable surfaces to segment 3D images and infer differential structures. *CVGIP: Image Understanding*, 56:242–263, 1991.

[16] L. D. Cohen and I. Cohen. Finite element methods for active contour models and balloons for 2D and 3D images. *IEEE Trans. on Pattern Analysis and Machine Intelligence*, 15(11):1131–1147, 1993.

[17] N. Cristianini and J. Shawe-Taylor. *An Introduction to Support Vector Machines.* Cambridge University Press, 2000.

[18] C. Davatzikos and R. N. Bryan. Using a deformable surface model to obtain a mathematical representation of the cortex, coral gables. In *International Symposium on Computer Vision, Coral Gables, FL*, pages 212–217, Los Alamitos, 1995. IEEE Computer Society Press.

[19] T. Deschamps. *Curve and Shape Extraction with Minimal Path and Level-Sets techniques - Applications to 3D Medical Imaging.* PhD thesis, Université Paris-IX Dauphine, Place du maréchal de Lattre de Tassigny, 75775 Paris Cedex, December 2001.

[20] J. Dong, A. Krzyżak, and C. Y. Suen. A fast parallel optimization for training support vector. In P. Perner and A. Rosenfeld, editors, *Machine Learning and Data Mining in Pattern Recognition*, volume LNAI 2734, pages 96–105, Leipzig, Germany, July 2003. Springer.

[21] J. Dong, A. Krzyżak, and C. Y. Suen. Fast SVM training algorithm with decomposition on very large training sets. *IEEE Trans. on Pattern Analysis and Machine Intelligence*, 27(4):603–618, 2005.

[22] R. O. Duda and P. E. Hart. *Pattern Classification and Scene Analysis.* John Wiley and Sons, New York, 1973.

[23] R. O. Duda, P. E. Hart, and D. G. Stork. *Pattern Classification.* Wiley-Interscience, 2001.

[24] G. Fahmy, D. Nassar, E. Haj-Said, H. Chen, O. Nomir, J. Zhou, R. Howell, H. H. Ammar, M. Abdel-Mottaleb, and A. K. Jain. Towards an automated dental identification system (ADIS). In *International Conference on Biometric Authentication*, volume III, pages 522–525, Hong Kong, July 2004.

[25] R. Farias, J. S. B. Mitchell, and C. T. Silva. ZSWEEP: an efficient and exact projection algorithm for unstructured volume rendering. In *2000 IEEE symposium on Volume visualization*, pages 91–99. ACM Press, 2000.

[26] A. Gupta, T. O'Donnell, and A.Singh. Segmentation and tracking of cine cardiac MR and CT images using a 3-D deformable model. In *Proc. IEEE Conference on Computers in Cardiology*, 1994.

[27] M. Holtzman-Gazit, D. Goldsher, and R. Kimmel. Hierarchical segmentation of thin structures in volumetric medical images. In *International Conference on Medical Image Computing and Computer-Assisted Intervention (MICCAI)*, pages 562–569, 2003.

[28] A. K. Jain and H. Chen. Matching of dental x-ray images for human identification. *Pattern Recognition*, 37(7):1519–1532, 2004.

[29] M. Jeon, M. Alexander, W. Pedrycz, and N. Pizzi. Unsupervised hierarchical image segmentation with level set and additive operator splitting. *Pattern Recognition Letters*, 26(10):1461–1469, July 2005.

[30] C. Jin. Feature preserving simplification techniques for tetrahedral meshes. Master's thesis, Department of Computer Science and Software Engineering, Concordia University.

[31] C. Jin, T. Fevens, S. Li, and S. P. Mudur. Feature preserving volumetric data simplification for application in medical imaging. In *International Conference in Central Europe on Computer Graphics, Visualization and Computer Vision*, pages 235–242, Plzen, Czech republic, 2005.

[32] M. Kass, A. Witkin, and D. Terzopoulos. Snakes: Active contour models. *International Journal of Computer Vision*, 1(4):321–331, 1988.

[33] S. Kichenassamy, A. Kumar, P. Olver, A. Tannenbaum, and A. Yezzi. Conformal curvatures flows: From phase transitions to active vision. *Archive for Rational Mechanics and Analysis*, 134:275–301, 1996.

[34] R. Kimmel and A. M. Bruckstein. Regularized Laplacian zero crossings as optimal edge integrators. *International Journal of Computer Vision*, 53(3):225–243, July 2003.

[35] M. E. Leventon, W. Grimson, L. Eric, and O. Faugeras. Statistical shape influence in geodesic active contours. In *IEEE Conference Computer Vision and Pattern Recognition*, volume 1, pages 316–323, Los Alamitos, June 2000. IEEE.

[36] S. Li, T. Fevens, and A. Krzyżak. Image segmentation adapted for clinical settings by combining pattern classification and level sets. In *International Conference on Medical Image Computing and Computer-Assisted Intervention (MICCAI)*, volume 3216 of *Lecture Notes in Computer Science*, pages 160–167, St-Malo, France, 2004. Springer.

[37] S. Li, T. Fevens, and A. Krzyżak. A SVM-based framework for autonomous volumetric medical image segmentation using hierarchical and coupled level sets. In *CARS*, volume 1268 of *International Congress Series*, pages 207–212, Chicago, USA, 2004. Elsevier.

[38] S. Li, T. Fevens, A. Krzyżak, C. Jin, and S. Li. Toward automatic computer aided dental x-ray analysis using level set method. In *International Conference on Medical Image Computing and Computer-Assisted Intervention (MICCAI)*, volume 3749 of *Lecture Notes in Computer Science*, pages 670–678, Palm Springs, California, USA, 2005. Springer.

[39] S. Li, T. Fevens, A. Krzyżak, and So. Li. Automatic clinical image segmentation using pathological modelling, PCA and SVM. In Petra Perner and Atsushi Imiya, editors, *Machine Learning and Data Mining in Pattern Recognition*, volume LNAI 3587, pages 314–324, Leipzig, Germany, 2005. Springer.

[40] S. Li, T. Fevens, A. Krzyżak, and So. Li. Level set segmentation for computer aided dental X-ray analysis. In *SPIE Conference on Medical Imaging*, volume 5747, pages 580–589, San Diego, USA, 2005.

[41] S. Li, T. Fevens, A. Krzyżak, and So. Li. Automatic clinical image segmentation using pathological modelling, PCA and SVM. *Journal of Engineering Applications in Artificial Intelligence*, 2006. In press.

[42] S. Li, T. Fevens, A. Krzyżak, and So. Li. An automatic variational segmentation for dental X-ray analysis in clinical environment. *Computerized Medical Imaging and Graphics*, 2006. In press.

[43] S. Li, T. Fevens, A. Krzyżak, and So. Li. A triple region image segmentation using two level set functions. In *Computer Assisted Radiology and Surgery*, Osaka, Japan, 2006. Accepted.

[44] S. Li, C. Jin, T. Fevens, A. Krzyżak, and S. P. Mudur. A medical volume reconstruction method using tetrahedral meshes and level set. In *Computer Assisted Radiology and Surgery*, Osaka, Japan, 2006. Accepted.

[45] W.-C. Lin, S.-Y. Chen, and C.-T Chen. A new surface interpolation technique for reconstructing 3D objects from serial cross-sections. *Computer Vision, Graphics, and Image Processing*, 48(1):124–143, 1989.

[46] W. E. Lorensen and H. E. Cline. Marching cubes: A high resolution 3D surface construction algorithm. In *SIGGRAPH '87: Proceedings of the 14th annual conference on Computer graphics and interactive techniques*, pages 163–169. ACM Press, 1987.

[47] L. M. Lorigo, O. D. Faugeras, W. E. L. Grimson, R. Keriven, R. Kikinis, and C.-F. Westin. Co-dimension 2 geodesic active contours for MRA segmentation. In *Information Processing in Medical Imaging*, pages 126–133, Visegrád, Hungary, June/July 1999.

[48] L. M. Lorigo, W. Eric L. Grimson, O. D. Faugeras, R. Keriven, R. Kikinis, A. Nabavi, and C.-F. Westin. Codimension - Two geodesic active contours for the segmentation of tubular structures. In *IEEE Conference Computer Vision and Pattern Recognition*, pages 1444–1451, 2000.

[49] R. Malladi, J. A. Sethian, and B. C. Vemuri. Shape modeling with front propagation: A level set approach. *IEEE Trans. on Pattern Analysis and Machine Intelligence*, 17(2):158–175, 1995.

[50] T. Mcinerney and D. Terzopoulos. Dynamic finite element surface model for segmentation and tracking in multidimensional medical images with application to cardiac 4d image analysis. *Computerized Medical Imaging and Graphics*, 19:69–83, 1995.

[51] J. V. Miller, D. E. Breen, W. E. Lorensen, R. M. O'Bara, and M. J. Wozny. Geometrically deformed models: a method for extracting closed geometric models form volume data. In *18th annual conference on Computer graphics and interactive techniques*, pages 217–226. ACM Press, 1991.

[52] W. Mollemans, F. Schutyser, J. V. Cleynenbreugel, and P. Suetens. Fast soft tissue deformation with tetrahedral mass spring model for maxillofacial surgery planning systems. In *International Conference on Medical Image Computing and Computer-Assisted Intervention (MICCAI)*, pages 371–379, 2004.

[53] W. J. Niessen, B. M. ter Romeny, and M. A. Viergever. Geodesic deformable models for medical image analysis. *IEEE Trans. on Medical Imaging*, 17:634–641, 1998.

[54] S. Osher and J. A. Sethian. Fronts propagating with curvature-dependent speed: Algorithms based on Hamilton-Jacobi formulations. *Journal of Computational Physics*, 79:12–49, 1988.

[55] N. Paragios and R. Deriche. Geodesic active contours and level sets for the detection and tracking of moving objects. *IEEE Trans. on Pattern Analysis and Machine Intelligence*, 22:266–280, 2000.

[56] J. Radon. Uber due bestimmung von funktionen durch ihre intergralwerte langsgewisser mannigfaltigkeiten (on the determination of functions from their integrals along certain manifolds. *Berichte Saechsische Akademie der Wissenschaften*, 29:262 – 277, 1917.

[57] R. A. Robb. *Biomedical Imaging, Visualization, and Analysis.* Wiley-Liss, 1999.

[58] C. Rössl, F. Zeilfelder, G. Nürnberger, and H.-P. Seidel. Reconstruction of volume data with quadratic super splines. *IEEE Transactions on Visualization and Computer Graphics*, 10(4):397–409, July/August 2004.

[59] G. Rote. Computing the minimum hausdorff distance between two point sets on a line under translation. *Information Processing Letters*, 38(3):123–127, 1991.

[60] E. Rouy and A. Tourin. A viscosity solutions approach to shape-from-shading. *SIAM Journal on Numerical Analysis*, 29(3):867–884, 1992.

[61] C. Samson, L. Blanc-Fraud, G. Aubert, and J. Zerubia. A level set model for image classification. *International Journal of Computer Vision*, 40(3):187–197, 2000.

[62] B. Schölkopf and A. J. Smola. *Learning with Kernels.* MIT Press, 2002.

[63] J. A. Sethian. *An analysis of flame propagation.* PhD thesis, University of California, Berkeley, 1982.

[64] K. Siddiqi, Y. Berube Lauzi'ere, A. Tannenbaum, and S. W. Zucker. Area and length minimizing flows for shape segmentation. *IEEE Trans. on Image Processing*, 7:433–443, 1998.

[65] J. S. Suri. Leaking prevention in fast level sets using fuzzy models: An application in MR brain. In *Proc. International Conference Information Technology in Biomedicine*, 2000.

[66] J. S. Suri. White matter/gray matter boundary segmentation using geometric snakes: A fuzzy deformable model. In N. Murshed S. Singh and W. Kropatsch, editors, *International Conference Applicat. Pattern Recognition,Lecture Notes in Computer Science*. Springer-Verlag, 2000.

[67] J. S. Suri. *Advanced Algorithmic Approaches to Medical Image Segmentation: State-of-the-Art Applications in Cardiology, Neurology, Mammography and Pathology*. Springer-Verlag, London, U.K., 2001.

[68] J. S. Suri. Two dimensional fast MR brain segmentation using a region based level set approach. *International Journal Engineering in Medicine and Biology*, 20:8 –28, 2001.

[69] R. Szeliski. Bayesian modeling of uncertainty in low-level vision. *International Journal of Computer Vision*, 5:271–301, 1990.

[70] H. Tek and B. B. Kimia. Shock-based reaction-diffusion bubbles for image segmentation. In *Third Conference on Visualization in Biomedical Computing. SPIE*, Ayache, 1995.

[71] D. Terzopoulos and K. Fleischer. Deformable models. *The Visual Computer*, 4(6):306–331, 1988.

[72] D. Terzopoulos, A. Witkin, and M. Kass. Constraints on deformable models: Recovering 3D shape and nonrigid motion. *Artificial Intelligence*, 35:91–124, 1988.

[73] D. Tosun, M. E. Rettmann, D. Q. Naiman, S. M. Resnick, M. A. Kraut, and J. L. Prince. Cortical reconstruction using implicit surface evolution: A landmark validation study. In *International Conference on Medical Image Computing and Computer-Assisted Intervention (MICCAI)*, pages 384–392, 2004.

[74] I. J. Trotts, B. Hamann, and K. I. Joy. Simplification of tetrahedral meshes with error bounds. *IEEE Transactions on Visualization and Computer Graphics*, 5(3):224–237, July 1999.

[75] A. Tsai, Jr. Yezzi, A., and A.S. Willsky. Curve evolution implementation of the Mumford-Shah functional for image segmentation, denoising, interpolation, and magnification. *IEEE Trans. on Image Processing*, 10:1169 – 1186, 2001.

[76] M. Turk and A. Pentland. Eigenfaces for recognition. *Journal of Cognitive Neuroscience*, 3(1):71–86, 1991.

[77] M. Turk and A. Pentland. Face recognition using eigenfaces. In *Proc. IEEE Conference on Computer Vision and Pattern Recognition*, Hawaii, 1991.

[78] V. Vapnik. *Statistical Learning Theory.* Wiley, NewYork, 1998.

[79] L. Vese and T. Chan. A multiphase level set framework for image segmentation using the Mumford and Shah model. *International Journal of Computer Vision*, 50(3):271–293, 2002.

[80] S. Wang, W. Zhu, and Z.-P. Liang. Shape deformation: SVM regression and application to medical image segmentation. In *International Conference on Computer Vision*, pages 209–216, 2001.

[81] W. M. Wells III, W. E. L. Grimson, R. Kikinis, and F. A. Jolesz. Adaptive segmentation of MRI data. *IEEE Trans. on Medical Imaging*, 15:429–442, 1996.

[82] R. Whitaker. Volumetric deformable models: Active blobs. In Richard A. Robb, editor, *Third Conference on Visualization in Biomedical Computing. SPIE*, volume 2359, pages 122–134, Ayache, 1994.

[83] E. P. Wigner. Converting energy to medical progress: Vital legacy of ber medical sciences. http://www.doemedicalsciences.org/pubs/sc0033/vital.shtml.

[84] O. Wink, R. Kemkers, S.-Y. J. Chen, and J. D. Carroll. Coronary intervention planning using hybrid 3D reconstruction. In *International Conference on Medical Image Computing and Computer-Assisted Intervention (MICCAI)*, pages 604–611, 2002.

[85] J.-H. Wu, S.-M. Hu, J.-G. Sun, and C.-L. Tai. An effective feature-preserving mesh simplification scheme based on face constriction. In *9th Pacific Conference on Computer Graphics and Applications*, page 12. IEEE Computer Society, 2001.

[86] A. Yezzi, S. Kichenassamy, A. Kumar, P. Olver, and A. Tannenbaum. A geometric snake model for segmentation of medical imagery. *IEEE Trans. on Medical Imaging*, 16:199–209, 1997.

[87] X. Zeng, L. H. Staib, R. T. Schultz, and J. S. Duncan. Segmentation and measurement of the cortex from 3-D MR images using coupled surfaces propagation. *IEEE Trans. on Medical Imaging*, 18(10):927–937, 1999.

[88] H.-K. Zhao, T. F. Chan, B. Merriman, and S. Osher. A variational level set approach to multiphase motion. *Journal of Computational Physics*, 127(1):179–195, 1996.